Critical bistability and large-scale synchrony in human brain dynamics

M.A. Sheng H Wang

Doctoral Programme Brain & Mind, University of Helsinki,
Division of Physiology and Neuroscience,
Faculty of Biological and Environmental Sciences, University of Helsinki.
Neuroscience Center, Helsinki Institute of Life Science, University of Helsinki.
Department of Neuroscience and Biomedical Engineering, Aalto University, Finland.

DOCTORAL DISSERTATION

To be presented for public examination with the permission of the Faculty of Biological and Environmental Sciences of the University of Helsinki,
in PORTHANIA PIII, on 19.11.2021 at 12 o'clock.

Research location: Neuroscience Center, Helsinki Institute of Life Science
Doctoral programme: Doctoral Programme Brain and Mind
Printing house: UNIGRAFIA
Printing location: Helsinki
Printing year: 2021
ISBN 978-951-51-7475-8 (Print)
ISBN 978-951-51-7476-5 (PDF)

Supervisors	**J Matias Palva, PhD** Department of Neuroscience & Biomedical Engineering, Aalto University, Finland; Neuroscience Center, Helsinki Institute of Life Science, University of Helsinki, Finland; Centre for Cognitive Neuroimaging, Institute of Neuroscience and Psychology, University of Glasgow, United Kingdom **Satu O Palva, PhD** Neuroscience Center, Helsinki Institute of Life Science, University of Helsinki, Finland; Centre for Cognitive Neuroimaging, Institute of Neuroscience and Psychology, University of Glasgow, United Kingdom
Thesis advisory committee	**Lauri Parkkonen, PhD** Department of Neuroscience and Biomedical Engineering, Aalto University, Finland **Petri Ala-Laurila, PhD** Department of Neuroscience and Biomedical Engineering, Aalto University; Faculty of Biological and Environmental Sciences, University of Helsinki, Finland
Pre-examiners	**Olaf Hauk, PhD** MRC Cognition and Brain Sciences Unit, University of Cambridge, United Kingdom **Krish Singh, PhD** Brain Research Imaging Centre, Cardiff University, United Kingdom
Opponent	**Philippe Ciuciu, PhD** CEA DRF Institut Joliot NeuroSpin, Gif-sur-Yvette; Inria Parietal, Université Paris-Saclay, Palaiseau, France

The Faculty of Biological and Environmental Sciences uses the Urkund system (plagiarism recognition) to examine all doctoral dissertations

To my family, and

for my father's unfulfilled wish

to save my brother from epilepsy.

Preface

In Platonian allegory of the cave, the show of shadows on the cave wall represents the very reality to the prisoners. Only after being unshackled and set free from the cave, a prisoner could experience the "true" reality in the outside world. This story, supposedly narrated by Socrates, tells us about the impact of new knowledge and the lack of it on human mind. The key concept of imperfect projection of truth in the cave allegory is where the classic philosophy connects today's hard sciences. Science is one way out of many for solving problems, especially the ones that matter to us and our existence. The problems that science excels at solving are those in which the predominant factors are subject to the basic laws of physics and therefore, can be projected into models using the language of logic and mathematics. Science is also a tradition of demarcating and managing reproducible solutions to such problems, weighing facts, heartlessly refuting the old beloved conjectures proven to be inaccurate or inadequate to reflect the truth. In other words, science consists of a feedforward loop of conjectures, comprehensions, testing, and a feedback loop for proving, improving, or refuting conjectures. Thus, it resembles a scenario, if I may, where there is always a bigger cave outside to be proven as the prisoners' reality – curiosity, honesty, and courage are the keys to the shackles.

By the author,
Savonlinna,
Summer, 2020

By Taija Sairanen, 03.14.2021

Table of Contents

Selected publications

This thesis is based on the following articles:

I. (Bistability) **Wang SH,** Arnulfo G, Myrov V, Siebenhühner F, Puoliväli T, Nobili L, Breakspear M, Palva S, Palva JM. Bistable critical dynamics in the resting-state human brain. (Submitted)

II. (HFO Synch) **Wang SH**†, Arnulfo G†, Myrov V†, Toselli B, Hirvonen J, Fato MM, Nobili L, Cardinale F, Rubino A, Zhigalov A, Palva S, Palva JM. (2020) Long-range phase synchronization of high-gamma activity in human cortex. ***Nature Communication***. (†*Equal contribution first author*)

III. (Ghosts) Palva JM, **Wang SH**, Palva S, Zhigalov A, Monto S, Brookes MJ, Schoffelen JM, Jerbi K. (2018) Ghost interactions in MEG/EEG source space: A note of caution on inter-areal coupling measures. ***Neuroimage***.

IV. (Hyperedge) **Wang SH,** Lobier M, Siebenhühner F, Puoliväli T, Palva S, Palva JM. (2018) Hyperedge bundling: A practical solution to spurious interactions in MEG/EEG source connectivity analyses. ***Neuroimage***.

V. (Hyperedge Methods) **Wang SH,** Lobier M, Siebenhühner F, Puoliväli T, Palva S, Palva JM. (2018) Hyperedge bundling: Data, source code, and precautions to modeling-accuracy bias to synchrony estimates. ***Data in Brief***.

The candidate conducted above work under the supervision of J Matias Palva and Satu O Palva, and his contributions as follows:

I. **SHW** and JMP conceived the study. **SHW** wrote code for the simulation and model analysis, and MB provided technical advice. **SHW** conducted analyses of model, SEEG, and MEG data. **SHW** and VM conducted classifier analyses. LN provided SEEG data. GA processed SEEG data. FS processed MEG data. **SHW**, JMP, MB, and SP wrote the manuscript. All authors contributed to manuscript revision and approved the submitted version.

II. GA, **SHW**, VM, SP, and JMP conceived the study. GA, **SHW**, VM, BT, AZ, and JMP wrote the analysis code. GA, **SHW**, VM, BT, JH, and MMF run the analysis. FC, LN, and AR provided clinical information and preprocessed clinical data. All authors contributed to the writing and revising the manuscript. All authors read and approved the manuscript.

III. JMP and JK conceived the study. JMP wrote code for simulation, JMP and **SHW** analyzed data and produced the results. JMP and JK wrote the manuscript. All authors contributed to manuscript revision, read and approved the submitted version.

IV. JMP and **SHW** conceived the study. **SHW** wrote code for simulation, analyzed data and produced the results; **SHW** and JMP wrote the manuscript. All authors contributed to manuscript revision and approved the submitted version.

V. JMP and **SHW** conceived the study. **SHW** wrote code for simulation, analyzed data and produced the results; **SHW** and JMP wrote the manuscript.

The articles below are co-authored by the candidate during his graduate studies and are related to but not included into this thesis:

I. Siebenhühner F, **Wang SH**, Arnulfo G, Nobili L, Palva JM, and Palva S. (2020). Resting-state cross-frequency coupling networks in human electrophysiological recordings Short title: Resting-state cross-frequency coupling networks. ***PLOS Biology*.**

II. Williams N, Arnulfo G, **Wang SH**, Nobili L, Palva S, and Palva JM. (2019). Comparison of methods to identify modules in noisy or incomplete brain networks. ***Brain Connectivity***.

III. Hirvonen J, Monto S, **Wang SH**, Palva JM, and Palva S (2017). Dynamic large-scale network synchronization from perception to action. ***Network Neuroscience***.

IV. Siebenhühner F, **Wang SH**, Palva JM, and Palva S. (2016). Cross-frequency synchronization connects networks of fast and slow oscillations during visual working memory maintenance. ***Elife***.

V. Honkanen R, Rouhinen S, **Wang SH**, Palva JM, and Palva S. (2015). Gamma oscillations underlie the maintenance of feature-specific information and the contents of visual working memory. ***Cerebral Cortex*.**

List of abbreviations

AIs	Artificial interactions
BiS	Bistability index
CC	Correlation coefficient
cPLV	Complex-valued phase locking value
CTF	Cross-talk function
cWM	Closest white-matter referencing
DFA	Detrend fluctuation analysis, the operationalization of LRTCs
EEG	Electroencephalography
E/I	Excitation/inhibition
EPSP	Excitatory postsynaptic potential
EZ	Epileptogenic zone
FC	Functional connectivity
FP(R)	False positive (rate)
fMRI	Functional magnetic resonance imaging
GMPI	Grey-matter proximity index
HFO	High-frequency oscillations
HGA	High-gamma activity
IIE	Interictal Epileptic Events
iPLV	Imaginary part of the complex cPLV
IPSP	Inhibitory postsynaptic potential
LFP	Local field potential
LRTCs	Long-range temporal correlations
MEG	Magnetoencephalography
MRI	Magnetic resonance imaging
MUA	Multiunit activity
nEZ	Brain regions that are not inside EZ
oCC	Orthogonalized correlation coefficient
PAC	Cross-frequency phase-amplitude coupling
pHFO	Pathological HFO
PLV	The phase locking value
PPI	Protein-protein interaction
PSF	Point-spread function
ROI	Regions of interest
SEEG	Stero-EEG
SI	Spurious interaction, or ghost interaction
TP(R)	True positive (rate)
wPLI	Weighted phase lag index

Abstract

Neurophysiological dynamics of the brain, overt behaviours, and private experiences of the mind are co-emergent and co-evolving phenomena. An adult human brain contains ~10^{11} neurons that are hierarchically organized into intricate networks of functional units comprised of interconnected neurons. It has been hypothesized that neurons within a functional unit communicate with each other or neurons from other units via synchronized activity. At any moment, cascades of synchronized activity from millions of neurons propagate through networks of all sizes, and the levels of synchrony wax and wane. How to understand cognitive functions or diseases from such rich dynamics poses a great challenge. The brain criticality hypothesis proposes that the brain, like many complex systems, optimize its performance by operating near a critical point of phase transition between disorder and order, which suggests complex brain dynamics be effectively studied by combining computational and empirical approaches. Hence, the brain criticality framework requires both classic reductionist and reconstructionist approaches. Reconstructionism in the current context is meant to address the "Wholeness" of macro-level emergence due to fundamental mechanisms such as synchrony between neurons in the brain. This thesis includes five studies and aims to advance theory, empirical evidence, and methodology in the research of neuronal criticality and large-scale synchrony in the human brain.

Study I: The classic criticality theory is based on the hypothesis that the brain operates near a continuous, second order phase transition between order and disorder in resource-conserving systems. This idea, however, cannot explain why the brain, a non-conserving system, often shows bistability, a hallmark of first order, discontinuous phase transition. We used computational modeling and found that bistability may occur exclusively within the critical regime so that the first-order phase transition emerged progressively with increasing local resource demands. We observed that in human resting-state brain activity, moderate α-band (11 Hz) bistability during rest predicts cognitive performance, but excessive resting-state bistability in fast (> 80 Hz) oscillations characterizes epileptogenic zones in patients' brain. These findings expand the framework of brain criticality and show that near-critical neuronal dynamics involve both first- and second-order phase transitions in a frequency-, neuroanatomy-, and state-dependent manner.

Study II: Long-range synchrony between cortical oscillations below ~100 Hz is pervasive in brain networks, whereas oscillations and broad-band activities above ~100 Hz have been considered to be strictly local phenomena. We showed with human intracerebral recordings that high-frequency oscillations (HFOs, 100–400 Hz) may be synchronized between brain regions separated by several centimeters. We discovered subject-specific frequency peaks of HFO synchrony and found the group-level HFO synchrony to exhibit laminar-specific connectivity and robust community structures. Importantly, the HFO synchrony was both transiently enhanced and suppressed in separate sub-bands during tasks. These findings showed that HFO synchrony constitutes a functionally significant form of neuronal spike-timing relationships in brain activity and thus a new mesoscopic indication of neuronal communication *per se*.

Studies III: Signal linear mixing in magneto- (MEG) and electro-encephalography (EEG) artificially introduces linear correlations between sources and confounds the separability of cortical current estimates. This linear mixing effect in turn introduces false positives into synchrony estimates between MEG/EEG sources. Several connectivity metrics have been proposed to supress the linear mixing effects. We show that, although these metrics can remove false positives caused by instantaneous mixing effects, all of them discover false positive ghost interactions (SIs). We also presented major difficulties and technical concerns in mapping brain functional connectivity when using the most popular pairwise correlational metrics.

Study IV and V: We developed a novel approach as a solution to the SIs problem. Our approach is to bundle observed raw edges, *i.e.,* true interactions or SIs, into hyperedges by raw edges' adjacency in signal mixing. We showed that this bundling approach yields hyperedges with optimal separability between true interactions while suffers little loss in the true positive rate. This bundling approach thus significantly decreases the noise in connectivity graphs by minimizing the false-positive to true-positive ratio. Furthermore, we demonstrated the advantage of hyperedge bundling in visualizing connectivity graphs derived from MEG experimental data. Hence, the hyperedges represent well the true cortical interactions that are detectable and dissociable in MEG/EEG sources.

Taken together, these studies have advanced theory, empirical evidence, and methodology in the research of neuronal criticality and large-scale synchrony in the human brain. Study I provided modeling and empirical evidence for linking bistable criticality and the classic criticality hypothesis into a unified framework. Study II was the first to reveal HFO phase synchrony in large-scale neocortical networks, which was a fundamental discovery of long-range neuronal interactions on fast time-scale *per se*. Study III raised awareness of the ghost interaction (SI) problem for a critical view on reliable interpretation of MEG/EEG connectivity, and for the development of novel approaches to address the SI problem. Study IV offered a practical solution to the SI problem and opened a new avenue for mapping reliable MEG/EEG connectivity. Study V described the technical details of the hyperedge bundling approach, shared the source code and specified the simulation parameters used in Study IV.

Tiivistelmä

Ihmisaivojen neurofysiologinen dynamiikka, ihmisen käyttäytyminen, sekä yksityiset mielen kokemukset syntyvät ja kehittyvät rinnakkaisina ilmiöinä. Ihmisen aivot koostuvat ~10^{11} hierarkisesti järjestäytyneestä hermosolusta, jotka toisiinsa kytkeytyneinä muodostavat monimutkaisen verkoston toiminnallisia yksiköitä. Hermosolujen aktiivisuuden synkronoitumisen on esitetty mahdollistavan neuronien välisen kommunikoinnin toiminnallisten yksiköiden sisällä sekä niiden välillä. Hetkenä minä hyvänsä, synkronoidun aktiivisuuden kaskadit etenevät aivojen erikokoisissa verkostoissa jatkuvasti heikentyen ja voimistuen. Kognitiivisten funktioiden ja erilaisten aivosairauksien ymmärtäminen tulkitsemalla aivojen rikasta dynamiikkaa on suuri haaste. Kriittiset aivot -hypoteesi ehdottaa aivojen, kuten monien muidenkin kompleksisten systeemien, optimoivan suorituskykyään operoimalla lähellä kriittistä pistettä järjestyksen ja epäjärjestyksen välissä, puoltaen sitä, että aivojen kompleksisia dynamiikoita voitaisiin tutkia yhdistämällä laskennallisia ja empiirisiä lähestymistapoja. Aivojen kriittisyyden viitekehys edellyttää perinteistä reduktionismia ja rekonstruktionismia. Erityisesti, rekonstruktionismi tähtää kuvaamaan aivojen makrotason "yhteneväisyyden" syntymistä perustavanlaatuisten mekaniikoiden, kuten aivojen toiminnallisten yksiköiden välisen synkronian avulla.

Tämä väitöskirja sisältää viisi tutkimusta, jotka edistävät teoriaa, empiirisiä todisteita ja metodologiaa aivojen kriittisyyden ja laajamittaisen synkronian tutkimuksessa. Tutkimus I tarjosi mallinnuksia ja empiirisiä todisteita bistabiilin kriittisyyden ja klassisen kriittisyyden hypoteesien yhdistämiseksi yhdeksi viitekehykseksi. Tutkimus II oli ensimmäinen laatuaan paljastaen korkeataajuisten oskillaatioiden (high-frequency oscillation, HFO) vaihesynkronian laajamittaisissa neokortikaalisissa verkostoissa, mikä oli perustavanlaatuinen löytö pitkän matkan neuronaalisista vuorovaikutuksista nopeilla aikaskaaloilla. Tutkimus III lisäsi tietoisuutta aave-vuorovaikutuksien (spurious interactions, SI) ongelmasta MEG/EEG kytkeytyvyyden luotettavassa tulkinnassa sekä uudenlaisten menetelmien kehityksessä SI-ongelman ratkaisemiseksi. Tutkimus IV tarjosi käytännöllisen "hyperedge bundling" -ratkaisun SI-ongelmaan ja avasi uudenlaisen tien luotettavaan MEG/EEG kytkeytyvyyden kartoittamiseen. Tutkimus V kuvasi teknisiä yksityiskohtia hyperedge bundling -menetelmästä, jakoi menetelmän lähdekoodin ja täsmensi tutkimuksessa IV käytettyjä simulaatioparametreja. Yhdessä nämä tutkimukset ovat edistäneet teoriaa, empiirisiä todisteita ja metodologiaa neuronaalisen kriittisyyden sekä laajamittaisen synkronian hyödyntämisessä ihmisaivojen tutkimuksessa.

1 Introduction

An organism's astonishing gift of concentrating a 'stream of order' on itself and thus escaping the decay into atomic chaos – (Schrodinger, 1944).

1.1 Complexity problems in life sciences and neurosciences

Life asserts itself as information, a phenomenological *order* against the decay into disorder prescribed by the second law of thermodynamics (Schrodinger, 1944). The Darwinian dynamic hypothesis proposes that the evolution of order in living organisms and certain physical systems obey the same set of fundamental principles (Bernstein et al., 1983). These principles dictate how macroscopic orders appear in interacting non-living materials, which results in dynamics far from thermodynamic equilibrium and eventually gives birth to life.

From a life sciences perspective, although living organisms from this earth vary widely in their genetic makeup, physical features, and lifespans, invariably they share the same underlying logics subservient to adaptation and heredity (Pennisi, 2003), which are for the very purpose to survive environmental changes and to thrive (Schrodinger, 1944; Sterling, 2012). These fundamental logics include how to gather, process, store, and utilize information, which are shaped by Darwinian selection (Ellis, 2005) and constructed with simple modular blocks such as negative and positive feedback/feedforward (Nurse, 2008; Wiener, 1948). Positive feedback, a key construct for this thesis, can generate an irreversible switching behaviour from one state to another whereas negative feedback is a generative mechanism for homeostasis and conservation. Combinations of these simple modules produce versatile functions including reversible toggle switches, timers, and oscillators, which eventually give rise to higher order adaptative behaviours such as error prediction and allostasis (Sterling, 2012).

From a physical sciences perspective, living organisms manifest themselves as complex systems[1] that are hardwired for learning and adaptation (Gell-Mann, 1995; Landauer, 1996). Their physical existences, as Rudolf Virchow put it 'all cells come from cells', are realized through an abstract process called integrative level[2]. Integrative level frequently asserts itself as quasi-periodic[3] objects with individual cells conventionally being considered, albeit arguably, as the most basic building components. Among all complex biological systems, the most fascinating specimen is the human brain – the seat of the sentient mind and the main subject of this thesis.

[1] A system: components in standing relationship (von Bertalanffy, 1968).

[2] Novel phenomena arise from pre-existing phenomena of a lower level. The construct *level* is a mean of constructing reality, which arranges components into a hierarchy based on the complexity of their inter-relationship. Thus, each component is simultaneously three entities: it is made up of components from the immediate lower level; it is a whole system in its own right; it is a component of the system on the immediate level above.

[3] Quasi-periodic objects show self-similarity in its building patterns and are thought to be the projections of periodic objects from higher-order (abstract) dimensions (Mandelbrot, 1985).

1.1.1 Levels and scales of enquiry into the brain

Several interrelated disciplines comprise an epistemological hierarchy[4] (Anderson, 1972) for studying brain dynamics[5] specific to physical levels (Figure 1A–F). A non-exhaustive list of the disciplines includes, following an ascending order, biochemistry, genetics and protein expression, cell biology, neurophysiology, systems neuroscience, and cognitive neuroscience. Throughout these levels of observations, each level links to the one immediate above it, and the organizational laws[6] are qualitatively distinct across levels (Ellis, 2005, 2008). Likewise, studying brain dynamics unavoidably concerns several scales across the temporal axis (Figure 1G). The human brain is the collective outcome of the evolutionary past of homo-sapiens, and multiple factors work together to shape the physical and functional dynamics across the lifespan in individuals.

Although, theoretically, there is no need for upper or lower boundaries in constructing an epistemological hierarchy, the number of levels is determined by the variation of physical properties and how they emerge (Figure 1H). Studying the laws of a particular level requires methods that can accurately address the physical expression of information on that level. Understanding the laws of a specific level is necessary for understanding the phenomena of the levels above. However, laws of lower levels are not necessarily predictive of higher-level phenomena because a multitude of realizations on the lower level can lead to the same macro-level outcome such as convergent evolution seen in different organisms. Neither can the higher-level phenomena be described using the vocabularies specific to lower level because the physical attributes are qualitatively different between levels, *e.g.*, intracellular biochemical signaling *vs*. inter-neuronal electric signaling between brain regions. The levels situated higher in the hierarchy have autonomous causal powers that are functionally independent of processes in the levels below (Novikoff, 1945). Yet, bottom-up actions and top-down causations coexist, with higher-level contexts determining the outcome of lower-level functionality and altering the long-term nature of lower-level constituents[7]. These attributes of brain dynamics thus present us an unconventional set of problems.

William Blake once wrote, 'to see a world in a grain of sand'. As a neurophysiologist myself, it would be nice to learn the operating principles of the human brain through a short period of a neurophysiological recording that is seemingly disordered – just as learning about the governing laws of a sand pile from grains of sand (Bak, 1996).

1.1.2 Three kinds of problems

There are three kinds of problems in the hard sciences (Weaver, 1948). The first kind constitutes the problems of *simplicity* that concern few strongly coupled variables. Classic examples include the 19th century physical problems or the firing mechanisms of single neurons (Hodgkin and Huxley, 1952). The second type of problems are of a *disorganized complexity* nature and involve an astronomically large number of variables with sparse interactions. Examples include the study of macro-level state of matter (Muñoz, 2018) or reconstruction and

[4] A vertical topology where smaller and more specific parts are nested within larger and more generic parts.

[5] The study of continually changing structure and behaviour of systems, which are defined as the flow consisting of the totality of systems trajectories.

[6] These rules that shape the interactions between elements and to the unit system as a whole (Novikoff, 1945); these rules are relevant level-specific physical properties and not to be confused with general principles governing complex systems.

[7] The downward causation claim has long provoked heated debates (Eronen, 2013; Noble, 2012), but I will not further the discussion here because it is not relevant to this thesis *per se*.

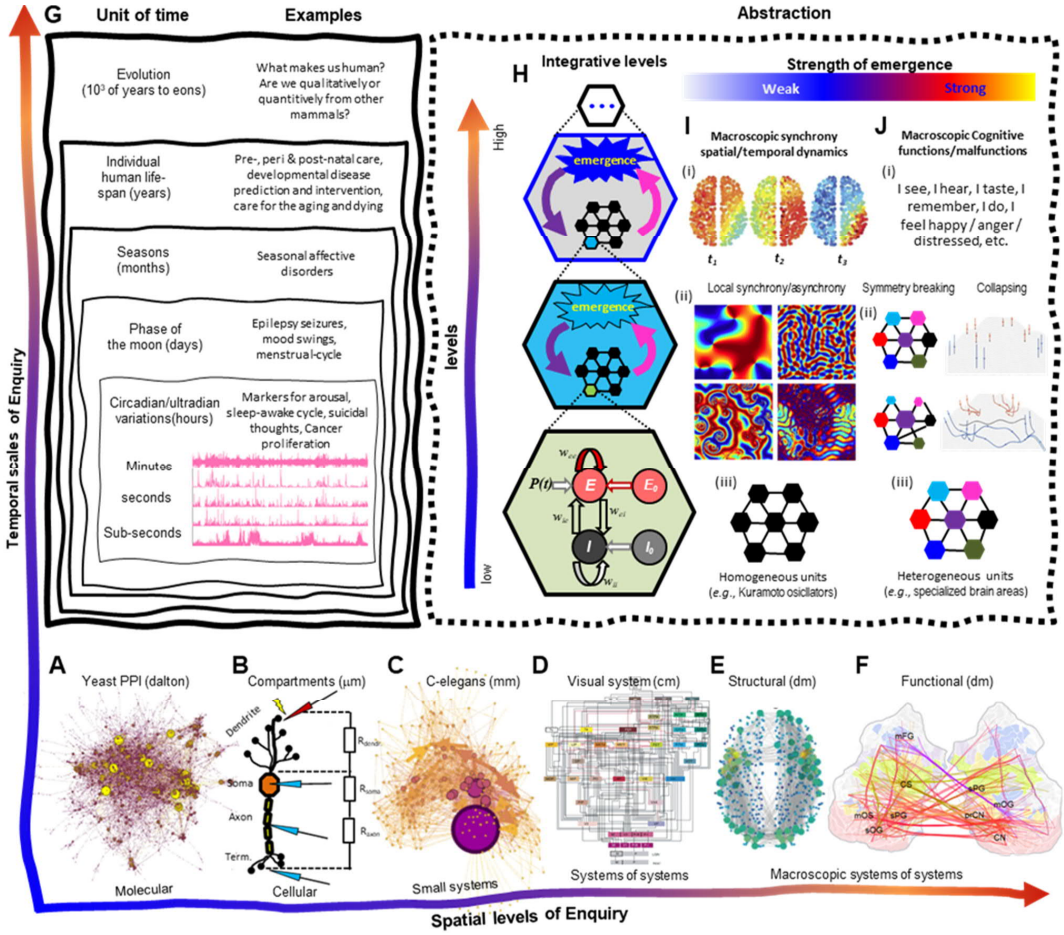

Figure 1 Problems of complexity and emergence relevant to the brain and the mind. (**A**) Yeast protein interaction graph; plotted by SHW using data from (Bu et al., 2003), (**B**) Functional segments of a model neuron, study notes based on (Rattay et al., 2018)**. (C)** A directed weighted graph representing C. Elegans neural network; plotted by SHW using data from (Watts and Strogatz, 1998). **(D)** Hierarchical structure of the primate visual cortex, adapted with permission from (Silvanto, 2015); Creative Commons license: CC-BY-NC-ND. **(E)** Human structural connectome, adapted with permission from (Gollo et al., 2018); license# 5012490201451. **(F)** A hypergraph showing increased α-band phase synchrony during working memory retention, adapted with permission from (Wang et al., 2018); Creative Commons license: CC BY-NC-ND 4.0. **(G)** Temporal scales of investigation of the brain dynamics and behaviours. (**H**) Caricature of integrative levels and emergence. The unit in the bottom tier is exemplified with a Wilson-Cowan model (Wilson and Cowan, 1972), wherein the solid red arrow represents a local positive feedback. Purple and magenta arrows in upper levels indicate coexisting bottom-up actions and top-down causations. (**I**) Examples of weak emergence where components are homogeneously modeled; (i) temporal evolution of large-scale dynamics in brain network model, adapted with permission from (Breakspear, 2017); license# 5012491086109; (ii) spinodal decompositions of synchrony in a Kuramoto model with varying degrees of order, adapted with permission from (Breakspear et al., 2010); (iii) Building motif. (**J**) Examples of strong emergence where the components are functionally inhomogeneous. (i) Cognitive functions; (ii) Symmetry break mechanism, adapted with permission from (Pillai and Jirsa, 2017); license# 5012500262773; (iii) Building motif.

simulation of micro-circuitry of neurons (Markram et al., 2015). 20th century statistical mechanics[8] provide potent tools to address these problems, wherein the precision of prediction increases as the system grows larger (Schrodinger, 1944), *e.g.*, the $1/\sqrt{n}$ law of error. The third type are *organized complexity* problems that concern

a sizable number of strongly and non-linearly coupled variables that are interrelated into "an organic whole" so that the collective behaviours are above and beyond individual behaviours. This Gestalt outcome is *emergence*, a central construct of systems theory.

1.1.3 Weak and strong emergence

For millennia, sages and scholars have extensively discussed the concept of emergence[9]. Recent definitions in sciences generally consider emergence as the arising of novel properties on macro-level in systems composed of many *autopoietic* components (Darley, 1996; Goldstein, 1999). Autopoiesis in this context refers to self-sustaining, self-organized non-linear interactions between components in which information processing and overall control are decentralized (Friston, 2013; Siljak, 2011). Emergence depends neither on the number of components nor on component intricacies, but rather on interaction protocols between components (Friston, 2013; Jonas and Kording, 2017; Lazebnik, 2002; Tamas Vicsek, 2002) and macro-micro dynamics (Marchiori and Possamai, 2015). Multiple emergent properties can concur in time and space and reuse most of the system components – this is an obvious evolutionary fitness because it builds more using less. However, solving the inverse problem of emergence in biological systems is hard because multiple underlying generative mechanisms could lead to the same global phenomena (Jonas and Kording, 2017; Lazebnik, 2002; Schrodinger, 1944). Although components can be complex systems and encapsulate high intricacies and rich functionality, macro-level emergent behaviours require only simple inputs/outputs such as yes-or-no answers from components. This insensitivity to component details gives rise to the robustness and universality of complex dynamics in living systems, for a comprehensive review on this subject matter see (Muñoz, 2018).

Emergent phenomena demonstrate varying degrees of strengths (Corning, 2002) (Figure 1I–J). In *weak emergence*, novel synchronic or diachronic macro-level phenomena are derived from the organized behaviours of the components, such as order or disorder in collective activity, and the system's external conditions (Bedau, 1997). The sandpile model (Bak, 1996) is a classic analogue of weak emergence, of which the building components are functionally homogeneous. In models of weak emergence, the characteristics of collective activity such as emergent synchrony and scale-free dynamics can be effectively studied with simulations and statistical mechanics (Bedau, 1997; Darley, 1996; Turkheimer et al., 2019). Examples of weak emergence models in neurophysiology include the spiking activity of interconnected primary neurons (Beggs and Timme, 2012; Priesemann, 2014; J. Wilting and Priesemann, 2019) and larger scale ensemble models (Breakspear, 2017; Deco et al., 2011). Importantly, large-scale neuronal models of weak emergence, albeit simple in construction, have shown network synchrony highly consistent with empirical observations in normal brains (Breakspear et al., 2010; Schirner et al., n.d.; Strogatz, 2004) and brains with diseases (Jirsa et al., 2017; Proix et al., 2017).

In *strong emergence*, radically novel phenomena appear at the macro-level via various synergistic[10] processes, but these novel phenomena cannot be observed locally in components or below the component level (Novikoff,

[8] A mathematical framework that studies how macroscopic properties, *e.g.*, heat or pressure, arise from statistics of the mechanics of large number of microscopic components, *e.g.*, molecules.

[9] For example, "...the totality is not, as it were, a mere heap, but the whole is something besides the parts ...", see Part 16, (Aristotle, 1991).

[10] A nonlinear inter-relationship between components of a system whereby they generate a combined outcome that are above and beyond the summation of functions of individual components. During synergistic processes, the interacting components could work together or against each other, *i.e.*, positive or negative synergy, respectively. The interactions between components promote the integration and evolution of specialized functionality among components.

1945; Turkheimer et al., 2019). A car serves a good analogue of strong emergence. Unlike the classic sandpile comprised of homogeneous sand grains, a car has different specialized parts and the parts further comprise of distinct specialized parts, and so on. A car would function normally only when its vital parts and their constituent parts function normally. However, the macro-level behaviours, *e.g.*, whether the car is skidding on an icy road, on standby, or on reverse, cannot be understood by analyzing, for example, the stroke phases of the engine piston or the dynamics a specific gear in the transmission system alone. Strong emergence is associated with steep hierarchy and modular organizations of components (Simon, 1962), functional encapsulation and specialization among components (Hoel et al., 2013; Sperry, 1980), macro-level downward causations (O'Connor, 1994), and symmetry breaking in spatio-temporal dynamics (Brading et al., 2017; Pillai and Jirsa, 2017). Representative theories of strong emergence in the brain include the "free energy" principle (Friston, 2010, 2009) and the integrated information theory of consciousness (Oizumi et al., 2014; Tononi et al., 2016). They are very hard problems.

In the brain, the macro-level properties in strong emergence are organic "wholeness" that are due to tight inter-relations and inter-dependency between functionally specialized components such as the functional systems and their subdivisions of the brain. This "wholeness" is an irreducible global phenomenon (Anderson, 1972; Krakauer et al., 2017; Laughlin, 2005) that cannot be understood by studying the properties of the components alone. Thus, the holistic "constructionist" hypothesis (Anderson, 1972) contests upfront some reductionist ideas that complex systems are nothing but the heap of its components (Godfrey-Smith, 2013; Polkinghorne, 2002). Furthermore, being capable of reducing to fundamental components does not equate to the ability to reconstruct (Anderson, 1972) due to metaphysical implausibility (Turkheimer et al., 2019). Therefore, when studying strong emergence such as the duality of the brain and the states of the mind, observing the ensemble dynamics and the dynamical relationship between ensembles are equally important (Anderson, 1972; Bar-Yam, 2002; von Bertalanffy, 1968), and even more so for addressing the physical nature of the relationship as recently proposed by (Pillai and Jirsa, 2017).

1.2 Neuronal connectivity and its costs across scales

The mammalian brain comprises of the cerebrum and the brain stem. The cerebrum comprises of telencephalon and diencephalon (Kandel et al., 2012; Patestas and Gartner, 2006). The telencephalon is the largest component of the brain, and it could be further divided into neocortex and subcortical structures. The neocortex is especially well developed in humans for supporting sensory, motor, and higher cognitive functions. The adult human brain contains $0.9\pm0.08\times10^{11}$ neurons (Azevedo et al., 2009), of which ~19% are found in the neocortex.

Although the neocortex represents a small portion of the total neuronal population of the human brain, its wiring and running expenditures are disproportionately high. An adult human cerebrum weights about 1.4 kg, and the neocortex grey and white matter together make up ~82% of the total brain mass (Azevedo et al., 2009). One neuron on average forms ~7000 synapses with other neurons (Pakkenberg et al., 2003), which in total yields $1.5–1.8\times10^{5}$ km of myelinated white-matter fibers (Drachman, 2005). Hence, neurons are well connected across scales from microscopic networks to large-scale interareal networks in the neocortex. High connectivity allows neurons to fire in synchrony on different levels, which in turn gives rise to new functionality throughout hierarchical anatomical scales. Moreover, the metabolic cost for maintaining brain functions is also high. The brain requires 20% of the whole body's energy budget in adults (Herculano-Houzel, 2011) and up to 66% in children (Kuzawa et al., 2014).

1.2.1 A graphic approach for studying brain connectivity

The graphic approach, also known as complex network analysis, offers a set of powerful tools to quantitively and qualitatively describe topological features of complex dynamical systems (Boccaletti et al., 2006; Newman, 2003; Sporns, 2018; Strogatz, 2001). The past two decades have seen a drastic increase in applying graphic approaches to study brain dynamics ranging from intracellular signaling across several scales to macroscopic anatomical and functional connectomes [11] (Sporns, 2018) (Figure 1A–F). The graphic approach is the methodological platform for Study III (Ghost) and IV and V (Hyperedge) and instrumental for discussing the following materials concerning brain connectivity cross scales (Sporns et al., 2005).

A *graph* is a mathematical object for modeling a specific feature set of a complex system, wherein a functional component is denoted as a *node* and a pairwise relationship between two nodes an *edge*[12] (Rubinov and Sporns, 2010). An edge may embody structural, functional, or effective connectivity (Friston, 1994). Structural connectivity refers to estimated anatomical connections obtained using invasive or non-invasive approaches such as directed neural tract tracing in animals and undirected tractography in human diffusion tensor imaging, respectively (Wandell, 2016). Functional connectivity (FC), the main interest of Study (I–V), refers to an estimated statistical interdependence between spatially distinct neurophysiological signals. FC may be directed or undirected depending on correlational or information-based metric being employed. FC are meaningful between temporal or spatial scales. An example of FC between temporal scales is within (1:1) frequency (S. Palva and Palva, 2012) and cross-frequency (n:m) phase coupling(F. Siebenhühner et al., 2016; Siebenhühner et al., 2020); an example of FC between spatial scales is spike and local field potential (LFP) coherence (Benchenane et al., 2010). Effective connectivity refers to the influences that one neuronal ensemble exerts over another ensemble over a time period, and they are usually dependent on specific models for describing causal relationships (Friston, 1994).

Both brain structural and functional connectivity show features of complex systems including small-world topology[13] (Bassett and Bullmore, 2006; S. Palva et al., 2010), modular [14] organizations (Sporns and Betzel, 2016), highly connected nodes (or hubs) at microscopic and macroscopic networks (Bullmore and Sporns, 2009; Hagmann et al., 2008; Sporns et al., 2005). Notably, many of these graph topological features persist across species and scales within species, which suggests an economical principle the brain obeys when balancing the trade-off between minimizing wiring cost and maximizing expensive yet advantageous topological properties such as global efficiency (Bullmore and Sporns, 2012). Importantly, a high fidelity connectivity graph, regardless of the interaction metric used, reflects the irreducible "wholeness" (1.1.3) crucial to understanding the emergent properties of the functional organizations (Turkheimer et al., 2019) and chains of macro-level behaviours (Pillai and Jirsa, 2017).

1.2.2 Interactions at single-neuron level

Neurons vary in morphology, functional specialty, and the neurotransmitters that they depend on for signaling (Kandel et al., 2012). A "canonical" neuron consists of a cell body (soma), dendrites, and an axon, but some

[11] A comprehensive topological description of the network of elements and connections forming the human brain (Sporns et al., 2005).

[12] There are multiple interchangeable terms for these elements; throughout this thesis, I will use node, edge, and graph.

[13] A network regime of average short path length and high clustering coefficient (Watts and Strogatz, 1998).

[14] Modules, or communities, in cortical networks are clusters of brain regions that are densely connected with each other (Sporns and Betzel, 2016).

neurons may not have dendrites and/or axon. Dendrites are tree-like cytoplasmic protrusions usually extend a few hundred micrometers from the soma, through which the neuron receives incoming connections from other neurons. An axon is a long and slender cytoplasmic protrusion from the soma that is usually myelinated and conducts action potentials away from the soma. An action potential is an electrical pulse initialed in the soma, from where it propagates along the axon until reaches axonal terminals. The intra-cellular ionic generating and propagating mechanisms of action potentials, were well scribed in the Nobel Prize winning work by (Hodgkin and Huxley, 1952) or its simplified version the Morris-Lecar model (Morris and Lecar, 1981) as a set of time-dependent nonlinear differential equations. The generating mechanism of action potential is a problem of simplicity (1.1.2).

Passing of information from an upstream neuron to a downstream neuron takes place at synapses or gap junctions[15]. A synapse is where the axonal terminals of the upstream (presynaptic) neuron "meet" the dendrite or cell body of the downstream (postsynaptic) neuron, and a multitude of neurotransmitters could be present in the synaptic cleft depending on the pathway and the type of neurons involved. A synapse is said to be "excitatory" or "inhibitory" based on how presynaptic inputs affect the postsynaptic conductance and ensuing change in probability of firing postsynaptic action potentials. In excitatory synapses, the releasing of neurotransmitter in presynaptic neuron pushes the postsynaptic potential (EPSP) toward the threshold of firing an action potential. Conversely, releasing of neurotransmitter in the inhibitory synapse causes the postsynaptic potential (IPSP) to shift farther away from the firing threshold. Most neocortical neurons receive a multitude of inputs from both excitatory and inhibitory synapses, *e.g.*, glutamatergic and GABAergic, respectively. Whether a postsynaptic neuron would fire an action potential is thought to depend on the spatial and temporal summation of these presynaptic inputs at a given time.

The temporally aligned firing among neuronal populations are thought to associated with the strengthening of synaptic connections and the forming of neuronal connectivity. The cell assembly theory (Hebb, 1950) proposes that networks of connected neurons are formed by strengthening synaptic connections based on pre- and post-synaptic activity. The group selection theory (Edelman, 1993) further proposes that ensembles of cortical and subcortical systems are dynamically organized into variable networks whose gross structure and function are determined by evolution but further modified by behaviours during development. The underlying neuroplasticity of these changes is not only dependent on pre- and post-synaptic firing but also is modulated by selecting the group of neurons via re-entrant pathways modulated via neurotransmitters. These theories emphasize the behavioural relevance of network dynamics instead of the firing of specific individual neurons. For the rest of this subsection, I will focus on the structure and dynamics of neuronal networks.

1.2.3 Micro- and mesoscopic connectivity

Anatomical connectivity is the basis of network dynamics. Neocortical neurons are organized into columns and within a column into six layers[16] (Molnár, 2013). A cortical column is a constellation of cells that share the same tuning for specific receptive field[17] and thus can be viewed as a local functional module (Horton and Adams,

[15] Gap junctions embody strong coupling and are primarily seen in short-range communications, and therefore are not relevant to this thesis.

[16] This thesis does not concern the allocortices, *e.g.*, the olfactory cortex and hippocampus, that have different laminar composition.

[17] The specific portion of a sensory space that can evoke cortical neuronal responses when stimulated (Alonso and Chen, 2009).

2005). In the human neocortex, the ratio between inhibitory and excitatory neurons is roughly 1:4 (Noback et al., 2005). The inhibitory neurons are crucial for generating oscillations in a column (Izhikevich, 2007; Wilson and Cowan, 1972), which allows parsing and concatenate neuronal activity for information coding (Buzsáki, 2012). Depending on species and cortical location, columns are 150–600 μm in diameter, and they are spatially organized like a 2D lattice and thereby forming a continuous sheet of neocortex. A column receives inputs and fires outputs via "interface" neurons located in specific layers, and these connections are prone to alteration due to various factors such as learning, adaptation, or diseases (Hawkins et al., 2017). Columns with similar receptive fields are neighbours on the neocortex sheet and are inter-connected with horizontal connections. Columns vary in terms of neuron types, diameter, volume, local connectivity patterns, and functions, which sometimes results in a lack of consensus regarding their structural and functional delineation (Horton and Adams, 2005; Rakic, 2008).

The cytoarchitecture within columns is relatively uniform across the neocortex. There are six layers within a column, and a column has average thickness of ~2.5 mm and range of 1–4.5 mm (Fischl and Dale, 2000). The layers are delineated in principle by cell types and inter-neuronal connections (Kandel et al., 2012). The generalized local connection patterns between layers include: *i*) layer IV neurons receive the majority of the synaptic inputs from thalamus and they simultaneously form local connections to other cortical layers; *ii*) layer II and III pyramidal neurons project to other areas and are the major output neurons; *iii*) layers V and VI neurons mainly project to the thalamus and brainstem (Noback et al., 2005).

Numerous models have been developed to study the interactions between neurons in cortical columns and layers (Breakspear, 2017; Hill, 2014; Izhikevich, 2007). These models aim to study the weakly emergent (1.1.3) electrophysiological phenomena in ensembles ranging from detailed biophysical models (with heterogeneous neurons) to abstract mean-field models (that mimic the interactions between homogeneous neurons). Despite the differences in implementational details, these models invariably focus on the emergent collective behaviours of a group of neurons in micro- and mesoscopic circuitries, and they do not concern the intracellular intricacy of the neurons in the columns.

1.2.4 Large-scale structural connectivity

Historically, the cerebral hemispheres were demarcated into the frontal, parietal, temporal, and occipital lobes based on overlying cranial bones (Kandel et al., 2012). The cortical surface is folded where the ridges and grooves are called gyri and sulci, respectively. Different neuronal ensembles specialize in processing specific information such as sensory, motor, auditory, or attention control functions, and ensembles for similar functions usually cluster together on the cortical sheet and distant from ensembles processing different functions. For example, the earlier and higher order visual processing areas are clustered mainly in occipital and temporal lobe (Wandell et al., 2007), whereas primary motor cortex is located in the frontal lobe (Sanchez-Panchuelo et al., 2010). Macro-level functions such as multisensory integrations and working memory requires the involvement of several brain regions.

The cerebral white matter contains axons and glial cells for supporting long-range connectivity between cortical regions. White matter connectivity decreases as brain size increases in primates (Herculano-Houzel et al., 2010). However, the volume of cortical white and gray matter scales with an exponent of 1.2(Mota et al., 2019; Zhang and Sejnowski, 2000), and this super-linear scaling[18] indicates that across primate species, white matter volume

[18] One quantity varies as the power of another quantity, where the power exponent is greater than 1.

increases faster than gray matter as the brain gets larger. The paradoxical combination of decreasing white matter connectivity with increasing white matter volume in larger brains was thought to reflect the universal scaling of cortical folding and the presence of small-world network topology with a decrease in global conduction delay (Herculano-Houzel et al., 2010).

The macro-level (whole-brain) networks do not obey the sheet-like organizational rules in micro- and mesoscopic networks. Most of the cortical neurons form only local connections with neurons in the immediate vicinity, and thus the information they carry would reach their neighbors but never – and no needs to – reach other distal parts of the cortex (Breakspear, 2017; Wandell, 2016). Some neurons do project axons and send local computational results to other parts of the brain. Many of such neurons usually project axons in bundles called fascicles that research similar destinations in other parts of the brain. Multiple fascicles bundle into larger pathways, *e.g.*, superior longitudinal fasciculus and the optic radiation, which in turn form the white matter core, *i.e.*, the information highway of the brain. Tractography algorithms estimate the fascicles from diffusion MRI data by finding streamlines whose orientations match the local diffusion orientation in fascicles with additional procedures to ensure the streamlines match the general anatomical features. Thus, an all-to-all structural connectome with estimated fascicles as edges can be mapped between all brain areas (nodes). The human structural connectome is known to show modularity (Sporns and Betzel, 2016), highly connected hubs (Bullmore and Sporns, 2009; Hagmann et al., 2008; Sporns et al., 2005).

1.2.5 Neuronal synchrony and oscillations across scales

Synchrony[19] is inevitable through which living systems establish orders (Pikovsky et al., 2003; Strogatz, 2004), and phase synchrony is a key aspect of emergent property of the complex systems (Anderson, 1972). Neural *oscillations* are rhythmic patterns of synchronized electrical activity produced by neurons in the brain (Buzsáki, 2006; Engel et al., 2001; Singer, 1999), spinal cord, and autonomic nervous system (Buzsáki, 2006). In the cortex, narrow-band neuronal oscillations reflect the fluctuations in cortical excitability. The balance between excitation (E) and inhibition (I) is relative so that within each oscillation cycle, E or I prevails at different phases. Oscillations, in the form of a continuously sine function of time, present the most energetically efficient solution for synchronizing neuronal activity and forming assemblies (Bullmore and Sporns, 2012; Buzsáki, 2006; Strogatz, 2004). Thus, in a "sending" phase, excitatory neurons synchronizes activity to dispatch information to downstream neurons, whereas in the receiving or perturbation phase, the ensemble can receive most effectively from upstream inputs (Buzsáki, 2012; Fries, 2015). Numerous physiological mechanisms have been proposed for cortical oscillations across scales, but there are only four bifurcation mechanisms for cortical oscillations (Izhikevich, 2007).

In the mammalian brain, neurons demonstrate behaviourally correlated oscillations spanning nearly five orders of rhythms approximately from 0.02 Hz to 600 Hz (Buzsáki, 2018; Buzsáki and Draguhn, 2004). Oscillatory rhythms vary across circuitries, regions, and different states of the brain. The collective activity of an ensemble, regardless of its micro- or mesoscopic connectivity pattern, can be regarded as an oscillator (Pikovsky et al., 2003; Pillai and Jirsa, 2017). Oscillations often are short bursts with sub-second duration, while some do retain for longer periods. There are roughly ten discrete brain rhythms denoted historically by Greek letters. Representative rhythms are listed as follows. The α-band (8–12 Hz) oscillations are observed in the occipital lobe most pronounced when a person resting with his/her eyes closed. The δ-band (0.5–1.5 Hz) represents the

[19] Synchrony is the adjustment of rhythms due to an interaction (Pikovsky et al., 2003), *e.g.*, *e pluribus unum*.

largest amplitude oscillations among all neocortical oscillations that occur during non-REM sleep. The θ-band (4–10 Hz) oscillations are prominent in the hippocampal-entorhinal system during spatial navigation and memory processing. The β-band oscillations (13–30 Hz) are observed in the motor system in the absence of movement. The γ-band oscillations (30–600 Hz) are present in nearly all structures and all brain states in which they dominate in the aroused, attentive brain. Moreover, oscillations of γ-band are thought to be local, whereas slower oscillations can recruit increasingly larger cortical area and connect multiple distinct regions (Buzsáki, 2018, 2006).

Synchronized cortical oscillations are instrumental for binding and segregating ensemble activities for communication between functional specialized regions (Buzsáki et al., 2012; Singer, 1999). The hierarchical "syntax" used between brain rhythms is mechanistic for neurons to communicate with each other on large-scale networks (Buzsáki, 2018, 2012, 2006). For example, the fast γ-band oscillations combine neurons into assemblies, which was proposed as a neuronal "letter". The cross-frequency coupling mechanism hierarchically combine these neuronal letters into neuronal "words" and words into "sentences", and so on. Thereby, combinatorial information generated bottom-up from spatially distributed spike patterns reaches global cortical network (Lisman and Idiart, 1995). For example, in the visual system, γ-band oscillations code various basic features such as edge orientation, contrast, colour, or locations in spatially segregated neuronal ensembles. Ensembles coding these lower-level features converge their output to neurons in the higher hierarchy so that these neurons higher in the hierarchy consequently become functionally specialized to higher-level visual features.

The interactions between rhythms allow both local computational results to reach global networks and a top-down control from global brain states to local computations. The centre frequencies of neighbouring bands have a non-integer relationship, and their entrainment requires energy[20] and thus cannot sustain over a long period. Hence, the interactions and interferences between cortical oscillations result in perpetual fluctuations between unstable and transiently stable states. On the other hand, different rhythms are bound by a hierarchical relationship, which can be observed as local cross-frequency coupling (Lisman and Jensen, 2013) or long-range cross-frequency phase-phase coupling (Palva, 2005; F. Siebenhühner et al., 2016; Siebenhühner et al., 2020; Tass et al., 1998), phase-amplitude coupling (Canolty et al., 2006; Vanhatalo et al., 2004), and phase-frequency coupling (Hyafil et al., 2015a).

Cortical oscillations, irrespective of their central frequencies or anatomical origins, are generated with neuronal circuitries built with simple motifs that usually involve the tuning between coupled glutamatergic excitatory neurons, GABAergic inhibitory neurons, and synaptic plasticity (Hellyer et al., 2016; Womelsdorf et al., 2014). Fluctuations in excitatory often involve the combined effects of more than two parties (Buzsáki, 2006). For example, in addition to coupled glutamatergic and GABAergic neurons, other neurotransmitters such as dopamine (Smialowski and Bijak, 1987) and serotonin (Ciranna, 2006) can also be involved in the tuning of the local E/I fluctuations and the resulting oscillations. Insensitive to the biological detail, this oscillation generating motif repeats across several spatial scales and supports the hypothesis that brain activity self-organizes near a critical bifurcation (1.3) and forms microscopic assemblies (Gollo et al., 2014), mesoscopic circuitry(Cabral et al., 2011), and whole brain level networks (Cabral et al., 2014). On the top of this hierarchy, large-scale neuronal

[20] As predicted by the Arnold tongue that the degree of entrainment of an oscillator coupled to a rhythmic driving force depends on the amplitude and the frequency of the drive (Jensen et al., 1983).

synchrony was proposed to be a key mechanism for the emergence of macrolevel brain functions and behaviours (Bastos et al., 2015; Buzsáki et al., 2012; Singer, 1999).

1.2.6 Behaviours and large-scale synchrony

Recent decades have witnessed important advancement towards a grand theory of brain dynamics and behaviours (Friston, 2010; Turkheimer et al., 2019). A specific behaviour of an organism refers to a set of internally coordinated actions (or inactions) in the presence of internal and/or external stimuli (Levitis et al., 2009). Here, coordinated actions is defined as low-dimensional patterns out of a large repertoire of processes (Huys et al., 2014), which constitutes the functional ordering of interacting components in space and time and bounded by constraints (Kelso, 2012). A function in this context is a process comprising of a temporal chain of causal dependence projected by an organism for achieving a specific goal (Dusenbery, 1992)[21].

A recent reflection (Krakauer et al., 2017) on current neuroscience research enunciates that the reductionist approach has much focused on correlational neuronal circuits, which would not yield insightful explanations for addressing the nature of macro-level behaviour and brain dynamics. For example, pharmacologically blocking one type of membrane ion channels abolishes certain types of ionic currents, which, across several scales, results in altered macro-level behaviours. Although, such microscopic alteration can be marked as *Causal* and *Necessary* to the macroscopic observables, it is not a *Sufficient* condition for the macroscale emergence. The need for understanding the Whole mechanism[22] of behaviour requires a formal framework to connect macro-level behaviours holistically to the emergence of whole-brain network dynamics (Pillai and Jirsa, 2017). The emergence of concurrent large-scale network connectivity and behaviour is irreducible (rationales in 1.1) and thus the *wholeness* nature of the large-scale connectivity ought to be addressed (Pillai and Jirsa, 2017).

The emergence of large-scale pattern formation[23] in the neuronal networks and concurring behaviour are thought to be caused by broken symmetry[24] in cortical space-time hierarchies (Anderson, 1972; Pillai and Jirsa, 2017). The cortical networks possess high-dimensional dynamics with complex connectivity. Behaviour is often mathematically defined as a set of low-dimensional ordinary differential equations that captures the dynamical influences from internal and external variables as well as the constraints imposed by a functional goal. Pillai and Jirsa (2017) thus suggested an update to the definition of behaviour as "a low-dimensional structured flow on manifold". Here, the *manifold* refers to low-dimensional subspace (collapsed from high-dimensional cortical connectivity) that is specific to and constrained by a task; the *structured flow* is the task-relevant organization of convergence, divergence, and the topology of the flow on the manifold whose stability is maintained by constraints tied to the task. When a task change, both the manifold and the structured flow may change drastically with concurring change (reset) in large-scale cortical connectivity.

---

[21] Due to the scope of this work, I will not argue exceptions of the "specific goal".

[22] Mechanism is a system performing a function by virtue of its components, their operations and organization (Bechtel, 2007)

[23] Any form of correlations between the states of the constituent components within a system; the said correlations can be linear or non-linear in spatial (between components) or temporal (between the past, current, and future in components) dynamics that last some period of time, *e.g.*, large-scale synchrony in neuronal networks.

[24] Symmetry is the existence of different viewpoints from which the system appears the same (Anderson, 1972), and thus it is a phenomenon of order where high compressibility of information is achieved; complexity involves interaction between symmetry and asymmetry, which is the coexistence of order and randomness.

Theoretical work on the link between behavioural and network dynamics typically investigate the effects of a perturbation on networks dynamics, *e.g.*, a stimulus as input and the emergent large-scale correlated neuronal activity as output (Abbott et al., 2016; Maass et al., 2002). Understanding and generalizing the principles that govern ensembles to form large-scale network dynamics associated with desired behaviours (or to avoid unwanted dynamics and associated disease states) is key to make advancement in basic research and clinical applications (Deco et al., 2015; Deco and Kringelbach, 2014).

Recent research on brain connectivity has accumulated a large body of modeling and empirical evidence for the understanding of connection between large-scale connectivity and behaviours. Synchronized neuronal activity across large-scale brain networks have been related to a wide range of behaviours such as sensation and perception (Hipp et al., 2011; Hirvonen et al., 2017; Monto et al., 2008; Senkowski et al., 2008), movement (Kim et al., 2017), attention (D'Andrea et al., 2019; Doesburg et al., 2016, 2008; Womelsdorf and Fries, 2007), working memory (J. M. Palva et al., 2010a; S. Palva et al., 2010), and decision making (Deco et al., 2009; Siegel et al., 2011). Likewise, neuropathology is rarely confined to few fixed anatomical foci but a network of affected regions that progressively spread through various pathways into other parts of the brain networks (Fornito et al., 2015; Uhlhaas et al., 2009; Uhlhaas and Singer, 2006). Thus, accurately estimating large-scale networks in individual patients is crucial to the evaluation, prediction, and intervention of the disease for quality individualized medicine.

1.3 Functional connectivity in electrophysiological data

Large-scale synchrony in the brain networks is thought to constitute a fundamental mechanism for processing and exchanging of information between ensembles, which eventually gives rise to the emergence of macro-level cognitive functions and behaviours (Anderson, 1972; Pillai and Jirsa, 2017; Varela et al., 2001). Empirical evidence supporting this hypothesis has been predominantly yielded from studying the functional connectivity (FC) between invasive electrophysiological recordings in animal models. These invasive methods can record neuronal activity from several orders of spatial scales. On micro-scale, single neuron spiking activity can be recorded using micro-electrodes from a single (Hubel and Wiesel, 1959) or multiple recording sites (Nicolelis et al., 1997). The multiunit activity (MUA) is the average spiking of small neuronal populations immediately adjacent to the recording electrode, and it is obtained by band-pass filtering the broad-band signals from above 400 Hz (Morgan et al., 2010). Local field potential (LFP) are intracerebral, extracellular electric potential generated by ensembles. The electrocorticography (ECoG) records the electric potential from exposed cortical surface which requires open skull surgery (Kuruvilla and Flink, 2003).

Invasive methods offer highly localized signals and can discover important mechanisms within specific systems (Hafting et al., 2005), but they cannot be widely used in human subjects to address a broad spectrum of research topics. This is because experimenters cannot casually drill holes on subjects' skull and insert electrodes into their brains, and current invasive protocols have poor spatial coverage and thus incapable of mapping large-scale connectivity. In humans, macroscopic neuronal activity can be recorded non-invasively with magneto- and electroencephalography (MEG/EEG), with which researchers can derive FC graphs with high temporal resolution and a good coverage of the whole brain (S. Palva and Palva, 2012).

This thesis concerns mapping large-scale cortical FC with SEEG (Study II) and MEG (Study III–V). To date, a wide variety of metrics are available for estimating cortical FC in terms of amplitude-, phase-, and phase-amplitude correlations within or across frequencies for pairs of electrophysiological signals (Aru et al., 2015; Bastos and Schoffelen, 2016; Jensen and Colgin, 2007; Kreuz, 2011; O'Neill et al., 2015). However, estimating

high fidelity FC using MEG/EEG is challenging due to linear mixing of signals, and I will discuss the problems in Study III and provide a practical solution in Study IV–V.

1.3.1 Non-invasive macroscopic readout: MEG and EEG

MEG and EEG are different measurements of the same neuronal signal sources (Hämäläinen et al., 1993; Hansen et al., 2010; Hari et al., 2010; Nunez and Srinivasan, 2007). MEG measures the extracranial magnetic fields generated by underlying neuronal currents (Baillet, 2017; Hari and Salmelin, 2012). EEG measures the potential differences on the scalp (Cohen, 2017; Puce and Hämäläinen, 2017). Neuronal currents include Impressed currents J_i, Primary currents J_p, and Volume currents J_v. The J_i are due to electrochemical gradients caused by opening of ion channels across the cell membrane in any compartment of the neuron. The J_p are dipolar currents inside dendrites and axons due to J_i. The dendritic J_p decay slower than axonal J_p, and both of them decay as distance from the synapse increases. The J_v are passive ohmic currents flow due to J_p. Because J_v are currents in the extracellular space, the direction of J_v is not confined as dendritic J_p that travel within apical dendrites of pyramidal neurons along the cortical column.

The dendritic J_p currents are the dominant currents and physiologically interesting. The J_p currents reflect neuronal activation following the arrival of presynaptic inputs. When a cortical pyramidal neuron receives presynaptic inputs at its dendritic arbour in the cortical layers II–IV, the voltage difference between the dendrite and soma results in intracellular J_p towards the soma situated in the deeper layers (EPSP). When many pyramidal cells in a cortical column temporally align their EPSPs, the spatial summation of the intracellular EPSPs in the column could be regarded as a dipole moment. Thus, when a presynaptic input activates a parcel of the cortex, the spatial summation of the EPSPs and magnetic fields generated in a multitude of columns would be strong enough for EEG and MEG sensors, respectively, to pick up from outside of the skull. Additionally, MEG uses superconducting quantum interference devices or SQUID sensors (Clarke 1994) to record the neuronal magnetic fields. The neuronal fields are in the order of femto-Tesla (10^{-15}) that is 10^8 times weaker than that of the earth magnetic field, and MEG recordings are conducted in a magnetically shielded room.

MEG and EEG sensors are sensitive to different components of the neuronal signals. The folding of cortical surface means that primary currents J_p have various orientations across cortical gyri and sulci (Hämäläinen and Ilmoniemi, 1994). MEG is thought to capture mainly the neuronal activity in the fissure walls because radial currents do not yield measurable magnetic field outside of a spherical conductor approximating the shape of the brain. EEG can detect both radial and tangential components of the currents, but the measurements often are affected by difference in impedance and movement etc.

1.3.2 Invasive readout of the LFP: SEEG

LFP are invasively recorded from within the cortex or other deep brain structures or nuclei. LFP signals are mesoscopic recording of electric potential generated by neuron populations in the immediate vicinity of the recording electrode. The locality of LFP signals could be limited to from few hundred microns when using micro-electrode (Katzner et al., 2009) or to millimeter-level resolution when using larger electrodes (Destexhe et al., 1999) and stereo-electroencephalography (SEEG) electrodes (Massimo Cossu et al., 2005).

The relation between LFP signals and neuronal activity are dependent on the macro-level brain state, and the overall correlations decay steeply with increased distance and time. For example, with millimeter-level recording in felines (Destexhe et al., 1999), low-amplitude fast rhythm dominates LFP traces during wakeful resting. This is thought to be associated with sustained irregular neuronal firing activity. An increase in neuronal

firing concurs with a large negative deflection in LFP trace, *i.e.*, an Up state. During slow wave sleep, the LFP traces from the same ensemble, albeit with large amplitude, exhibit similar pattern to that during rest. However, large positive peaks were correlated with momentary silencing in neuronal firing, *i.e.*, a Down state. The association between neuronal Up and Down firing states and LFP slow waves has been reported in both humans (Peyrache et al., 2012) and animals (Steriade et al., 2001), and thus likely a universal phenomenon in the mammalian brain.

SEEG, developed first by (Bancaud and Talairach, 1965), is a pre-surgical assessment of intracortical LFP signals for the treatment of drug-resistant focal epilepsy (Jerbi et al., 2010; Lachaux et al., 2012). The assessment aims to identify the epileptogenic zone (EZ) that are the primary organization of brain regions where epileptic seizures initiate, propagate, and maintain (Munari and Bancaud, 1985). The SEEG surgical procedure is minimally invasive and has had great safety records in clinical applications (Massimo Cossu et al., 2005). SEEG probes are linear shafts with multi-lead cylindrical electrode contacts. During implantation, SEEG shafts are inserted into the brain through small burr holes in the skull. The shafts can be inserted into both hemispheres and record deep structures where other methods such as ECoG or EEG are unable to reach. With high resolution MRI image of the patient brain and robotic assistance (Mullin et al., 2016), neurosurgeons can insert multiple electrode shafts with converging trajectories to targeted brain areas with high precision (Cardinale et al., 2013b). During the probing period, SEEG signals could be recorded from all electrode contacts during different brain states or tasks for EZ localization (Study I) and mapping functional connectivity (Study II).

1.3.3 Signal mixing confounds FC estimates in MEG/EEG

Accurately identifying cortical FC is crucial for understanding the co-emergence of large-scale neuronal synchrony, cognitive functions, behaviours, or diseases. A MEG or EEG system typically has a few dozens to a few hundred sensors covering the whole head, which makes them the only non-invasively electrophysiological tools for probing large-scale cortical connectivity. Importantly, MEG/EEG records neurophysiological activities and offers millisecond range temporal resolution like that of intracranial recording of LFP.

The MEG/EEG cortical FC is conventionally estimated as correlations between band-limited oscillatory signals in sensor- or sources-space. A wide variety of pairwise metrics (Aru et al., 2015; Bastos and Schoffelen, 2016; Jensen and Colgin, 2007; Kreuz, 2011; O'Neill et al., 2015) are available for estimating the FC "connectome", *i.e.*, the FC between pairs of signals from all sensors or modeled brain regions (Sporns et al., 2005). Estimated FC connectomes are often represented as graphs wherein sensors or brain areas constitute the nodes and observed FC the edges (1.2.1).

However, mapping high quality FC using MEG/EEG is challenging. MEG/EEG sensor data are anatomically uninformative and severely confounded by signal linear mixing (J. M. Palva and Palva, 2012; Felix Siebenhühner et al., 2016). Signal mixing or source leakage, in the form of field spread or volume conduction in MEG or EEG, respectively, has two aspects: *i*) the signals from one neuronal source can be registered by several sensors; *ii*) one sensor can pick up a mixture of signals from several focal sources. Analyses using modeled sources are preferable because it elucidates the neuroanatomical origins of the activities and reduces the net effects of signal mixing (Buzsáki et al., 2012; Gross et al., 2013; Hämäläinen et al., 1993; S. Palva and Palva, 2012; Schoffelen and Gross, 2009).

However, due to the ill-posed nature of the inverse solution, no source modeling methods can yield unambiguous estimates of neuronal sources. Different modeling methods may vary quantitatively in residual signal mixing, but the effect of the residual is pervasive to all source models (Figure 2A). The residue mixing inevitably

introduces false positive into estimated FC connectomes and distorts the estimated FC graph topology. Two distinct types of false positive FC could be observed in estimated FC graphs: artificial interactions (AIs) and ghost interactions (SIs) (S. Palva and Palva, 2012).

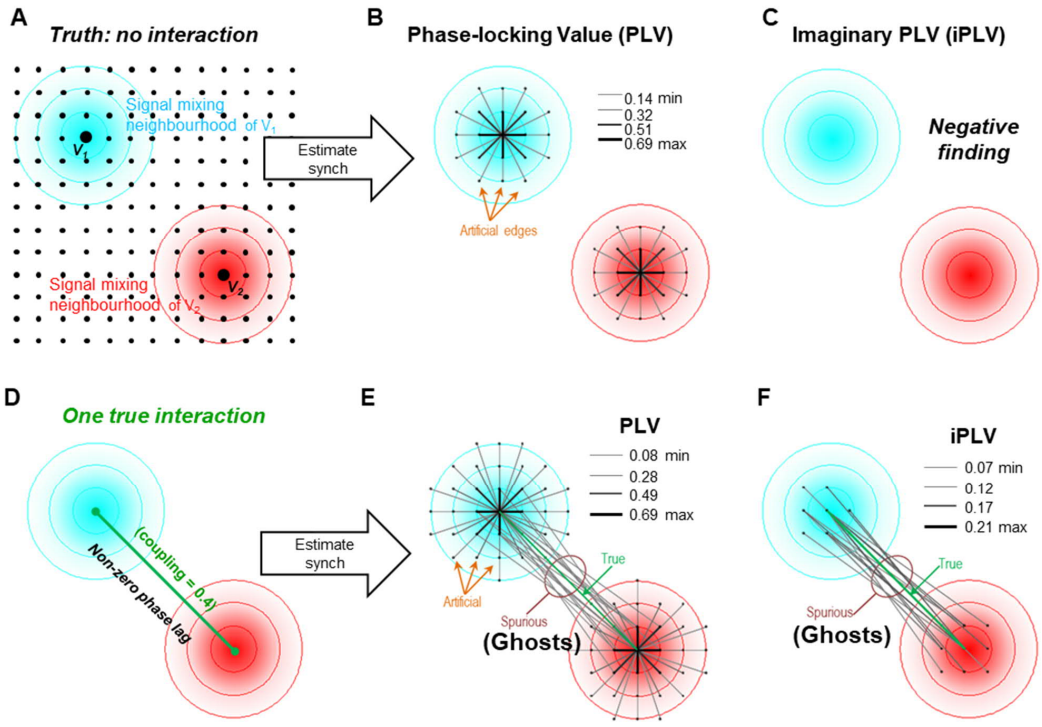

Figure 2 Linear mixing causes false-positive artificial (AI) and ghost interactions (SI). **(A)** The mixing "neighbourhood" of two uncoupled signal sources V_1 and V_2. The dots indicate the location of all modeled sources. **(B)** PLV reports false positive AIs between V_1, V_2 and their respective neighbouring sources. **(C)** iPLV does not report AIs. **(D)** One simulated true coupling between V1 and V2 with a non-zero phase lag. **(E)** The estimated synchrony graph using PLV is contaminated with both AIs and ghost interactions (SIs). **(F)** The iPLV graph is contaminated with non-zero lag SIs. Figures adapted with permission from (Palva et al., 2018); Creative Commons license(CC BY-NC-ND 4.0).

The problem of AIs was documented in the early days of FC research (Nolte et al., 2004). AIs are direct products of instantaneous signal mixing, in which one true signal is smeared to multiple adjacent[25] modeled sources – regardless of whether true interactions exists or not between the true source and the neighbours (Figure 2A–B). Several AI-free metrics have been proposed to suppress AIs by removing zero phase lag connectivity between two signals' amplitude envelopes (Brookes et al., 2012; Hipp et al., 2012; O'Neill et al., 2015), phase time series (Palva, 2005; Stam et al., 2007; Vinck et al., 2011), or coherency (Nolte et al., 2004). For example, AIs in estimated phase correlations can be effectively removed using the imaginary part of the complex phase locking value (Figure 2C). In addition, these AI-free metrics remove AIs at the cost of also removing true edges having near zero phase lag.

[25] Adjacent in terms of mixing because the mixing between sources is a geometrical property of the source model, and it is not necessarily linearly dependent on Euclidean distances between brain regions.

The ghost SIs are caused by the leakage of the signals from two truly connected nodes to their respective neighbouring nodes, which in turn results in multiple falsely identified edges like ghosts surrounding the true edge (Colclough et al., 2015; Farahibozorg et al., 2018; S. Palva and Palva, 2012). The ghost SIs, caused by multivariate mixing effects, could have non-zero phase lag, and therefore, they cannot be removed by any aforementioned AI-free metrics (Figure 2D–F). To date, one multivariate solution[26] has been proposed for correcting ghost SIs in amplitude correlations with sparse sources. In studies preferring dense sources, mixing could cause a multitude of SIs which renders FC edge localization and graph properties inaccurate (Drakesmith et al., 2015).

1.4 The critical brain hypothesis

1.4.1 Background: criticality and phase transitions

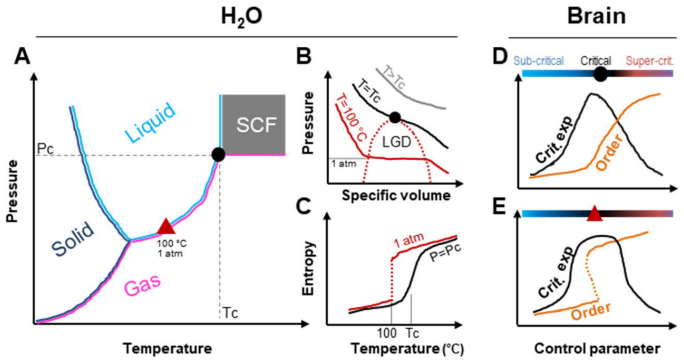

Figure 3 First and second order phase transitions. **(A)** Schematic drawing of phase diagram of H_2O with pressure and temperature as control parameters. The black marker indicates second phase transition point. Overlapping magenta and cyan lines indicate where first order transition can take place, and the red marker indicates the example discussed in the text. Pc and Tc are critical pressure and temperature, respectively. SCF: supercritical fluid. **(B)** Phase transitions with pressure as the control parameter for temperature T=100°C (below Tc), exactly at T_C, and above T_C. The black and red line corresponding to second and first order phase transition from **(A)**, respectively. The area inside red dashed line represents the liquid-gas-dome where water and steam coexist. **(C)** Liquid-gas transition of water is associated with the involvement of Gibbs free energy and discontinuity in entropy in the first order phase transition (red line) but not so in the second order phase transition (black line); the red dashed line marks the discontinuity in the curve. **(D)** Schematic drawing of the operating regimes of neuronal systems in the classic criticality and the underlying second order phase transition in the order parameter. **(E)** Hypothesized neuronal critical bistability and the underlying first order phase transition in the order parameter.

The term criticality comes from the study of equilibrium [27] systems that operate in the vicinity of phase transitions. Phase transition refers to a system property, such as the level of order among its components, changing abruptly as a response to a small change in environmental conditions quantified as certain control parameters. For example, below 0°C under 1atm pressure, H_2O molecules are organized in ordered solid phase, *i.e.*, ice. When increasing the temperature from slightly below 0°C to slightly above 0°C, a transition from solid to liquid phase takes place, in which H_2O molecules become less ordered. In other words, a phase transition is a macroscopic emergence due to changes in the inter-component interaction patterns. A complex system can demonstrate multiple phases under different conditions, and there could be multiple phase transitions as well as coexistence of multiple phases.

[26] This approach simultaneously orthogonalizes a few dozens of full-ranged source time series using the Löwdin procedure (Colclough et al., 2015, 2016)

[27] A system is said to be in equilibrium when it is isolated from external influences so that no flux of mass or energy pass through it. The models often used as analogy to neuronal criticality including the Ising model and the self-organized critical sand pile model.

The classic criticality is thought to reflect the dynamics undergoing a second order, smooth phase transition between order and disorder (Chialvo, 2010). For example, a second order phase transition takes place near the transition from fluid to supercritical matter phase when applying critical temperature (T_C) and/or critical pressure (P_C) [28] to a mass of H_2O (grey area, Figure 3A). Exactly at this critical point, the transition between liquid and supercritical matter requires no latent heat, which means, the changes in order parameter (*e.g.*, density = 1÷ specific volume) and entropy are smooth when either control parameter varies (Figure 3B–C, the T_C or P_C is the critical point that marks the second order phase transition). Henceforth, a mass of supercritical H_2O shows divergence of correlation length, critical fluctuations of multiple quantities occur at all length scales, which can be quantified with several critical exponents. For example, the critical opalescence in supercritical H_2O is due to the fluctuations of density in all wavelengths thus scattering visible lights.

A complex dynamical system can also undergo first order, discontinuous phase transition. For example, the first order phase transition takes place in a bistable state where the liquid and gaseous phase of H_2O coexist, *i.e.*, boiling water at 100 °C under 1atm pressure (red triangle, Figure 3A). The first order phase transition is said to be discontinuous, because during the liquid-gas transition there is a jump in the specific volume, order, entropy, and the first derivative of Gibbs free energy[29]. Bistable state is associated with hysteresis loop due to the involvement of latent heat, which means the current state of a system is dependent of the its immediately past state, and changing states requires the input or dissipation of energy.

1.4.2 The classic neuronal criticality framework

In neuroscience, criticality is an appealing framework for studying the co-emergence of behaviours and hierarchy of complex neuronal dynamics (Beggs and Timme, 2012; Chialvo, 2010; Cocchi et al., 2017; Muñoz, 2018; Plenz and Thiagarajan, 2007; J Wilting and Priesemann, 2019). The working hypothesis of brain criticality claims that the brain, across its levels of organization, operates in the vicinity of a second order phase transition between order and disorder (Figure 3D). Such critical dynamics are thought to optimize balance between the robustness to disturbance and the sensitivity/flexibility to everchanging stimuli or environmental conditions, and thereby conferring optimal computational capacity and rich dynamical repertoires (Muñoz, 2018).

Modeling studies have shown that when operating near the critical point, neuronal ensembles or large neuronal networks demonstrate metastability (Deco et al., 2017; Haldeman and Beggs, 2005), maximize the dynamic range (Gautam et al., 2015; Kinouchi and Copelli, 2006), information representation and processing (Boedecker et al., 2012; Shriki and Yellin, 2016; Tanaka et al., 2009), and computational capacity (Bertschinger and Natschläger, 2004; Cocchi et al., 2017; Latham and Nirenberg, 2004). These findings suggest that operating near criticality be an overarching principle that guides the brain dynamics (Bak, 1996; Beggs, 2008; Chialvo, 2010; Kauffman, 1993; Mora and Bialek, 2011).

1.4.3 Scale-invariance: the hallmark of neuronal criticality

There are several subcategories of criticality (Muñoz, 2018), and all of which share one emergent property: scale-invariance. The scale-invariance, as a construct, refers to the absence of characteristic scales in observed *quantity* and the *temporal* and/or *spatial* scales wherein the observations were made. Hence, scale-invariance

[28] For H_2O, the T_C is 373.9 °C and the P_C is 217.8 atm

[29] Gibbs free energy G = H - TS, where H is the enthalpy, T is the absolute temperature, and S is the entropy; H = U + pV, where U is the internal energy, p is the pressure, and V is the volume.

reflects the classic fractal[30] geometry, *i.e.*, statistical self-similarity and underlying building pattern of expanding symmetry (Mandelbrot, 1985). In practice, scale-invariance can be operationalized as various power-law scaling behaviours wherein one quantity varies as a power of another[31].

Scaling behaviours have been reported in a wide variety of dynamics varying from overt behaviours to neurophysiological signals. For example, in humans, the fluctuations in tasks performance have been reported to show scale-invariant long-range temporal correlations (LRTCs) (Gilden and Wilson, 1995; Monto et al., 2008; Simola et al., 2017), of which, the scaling exponent can be estimated using detrended fluctuation analysis (DFA) (Hardstone et al., 2012; Linkenkaer-Hansen et al., 2001). The LRTCs in behavioural fluctuations mean that, within individuals, descriptive statistics such as mean or standard deviation of short-term performance could readily predict the descriptive statistics of long-term performances.

The critical brain hypothesis proposes that, when operating near criticality, the brain produce a variety of scaling behaviours simultaneously across spatial, temporal, and spatio-temporal domains (Bassingthwaighte et al., 2012; Beggs and Timme, 2012; Linkenkaer-Hansen et al., 2001; Muñoz, 2018; Stanley, 1971). For a neuronal ensemble, the LRTCs in spontaneous fluctuations of narrow-band oscillation amplitudes can be estimated using DFA, which has revealed power-law scaling in amplitude fluctuations from few seconds up to at least a few hundred seconds (Linkenkaer-Hansen et al., 2001; Palva et al., 2013). For a neuronal network, spatio-temporal cascades of neuronal activities, such as a local peak in narrow-band amplitude or spiking activity, are referred to as "neuronal avalanches". Similar to the classic sand pile model, scaling behaviours in neuronal avalanche size and lifetime probability distribution have been reported in both small systems such as neurons in organotypic cultures (Beggs and Plenz, 2003) and large systems such as the resting-state human brain (Palva et al., 2013).

Moreover, the neuronal scaling behaviours have been reported to correlate with genetics (Linkenkaer-Hansen et al., 2007), age and gender (Nikulin and Brismar, 2005), arousal level (Nikulin and Brismar, 2004), response to stimuli (Arviv et al., 2019), and behavioural performances (Palva and Palva, 2014). Conversely, anomalies in neuronal scaling has been associated with depression (Linkenkaer-Hansen et al., 2005), epilepsy (Monto et al., 2007), dementia (Montez et al., 2009), and various other conditions (Zimmern, 2020). Importantly, the DFA scaling exponent of ensemble oscillation amplitudes (*i.e.*, LRTCs) and the scaling exponent of neuronal avalanches were found to be correlated during rest or tasks (Palva et al., 2013; Porta and Copelli, 2019), and both neuronal scaling exponents were found to be correlated with the DFA exponent of behavioural performance (Palva et al., 2013). Therefore, between local and large spatial scales, between short and long temporal scales, scale-invariant neuronal dynamics could be inter-related and, importantly, behaviourally relevant. This offers evidence of co-emerging critical-like fluctuations in human behaviours and intrinsic brain dynamics.

In practice, claiming power-law scaling requires not only enough data (Stumpf and Porter, 2012) but also rigorous statistical testing (Clauset et al., 2009; Virkar and Clauset, 2014). Moreover, criticality is sufficient but

[30] Fractals is a universality class of "a rough or fragmented geometric shape that can be split into parts, each of which is (at least approximately) a reduced-size copy of the whole" (Mandelbrot, 1983).

[31] An example is the scaling between cortical grey and white matter in the mammalian brains defined as $y = x^a$, where, when white matter volume (x) doubles, the power-law exponent (a = 0.8) dictates that the grey matter volume (y) increases by ~70%.

not necessary for producing power-law scaling behaviours because some non-critical models may produce power-law scaling when tuned (Touboul and Destexhe, 2017).

1.4.4 The classic neuronal criticality framework needs an update

The renormalization group approaches assume universality of scale-invariance and predict scaling behaviours asymptotically at large spatial and temporal scale when a system operates near or exactly at the critical point of second order phase transition. One consensus in probability is that the scaling behaviours should be considered in stationary processes when the observed system is in a steady state (Beran, 1994; Samorodnitsky, 2006). However, biological systems, unlike idealized classic criticality models, often demonstrate signs of non-stationarity (Eke et al., 2002, 2000). In the brain, the nonstationary phenomena include bistability (Figure 3E) or multi-stability (Buendía et al., 2019; Deco and Jirsa, 2012; di Santo et al., 2018), stochastic oscillations (Cocchi et al., 2017), Griffiths phase (Juhász et al., 2012; Moretti and Muñoz, 2013; Ódor et al., 2015), chimera state (Majhi et al., 2018; Wang and Liu, 2020), and multi-fractality (Ihlen and Vereijken, 2010; Kantelhardt, 2008; La Rocca et al., 2018). To date, little do we know about the mechanistic link between these rare regimes and the classic neuronal criticality, and their behavioural implications. These rare regimes could be caused by the specific type of criticality that the brain dynamics are associated with (Muñoz, 2018).

Recent theoretical work suggests that the brain, a non-conserving biological system, operates in a *quasi*-critical rather than in the "true" critical regime (Bonachela et al., 2010; Bonachela and Muñoz, 2009; Buendía et al., 2020). True criticality is seen in energy-conserving systems such as the classic sand pile model, in which, with a slow drive of the falling sand grains, the sand pile self-evolved into one-critical-point dynamics (Bak et al., 1987; Buendía et al., 2020). Here, energy-conserving means that the total energy or resource, *e.g.*, sands, remains constant and far greater than the drive when the system is very large. The critical point in true criticality is associated with a second order, smooth phase transition between a quiescent absorbing and active dissipating phase (Chialvo, 2010; Di Santo et al., 2016), and thus ensuing statistically stationary state and scaling behaviours (Bonachela and Muñoz, 2009).

On the other hand, *quasi*-criticality is observed in non-conserving, non-equilibrium systems equipped with a "soft loading" mechanism to counterbalance resource dissipation. Modeling work has shown that *quasi*-critical systems hover near the critical point and also produce scale-invariant dynamics (Bonachela et al., 2010; Buendía et al., 2020; Levina et al., 2007). In order to operate exactly at the critical point, *quasi*-critical systems require external fine-tuning between resource loading and dissipation.

The brain apparently is not an energy-conserving system, and it is also equipped with resource loading mechanisms across spatial scales to meet the constant resource demands from billions of neurons (Roh and Kim, 2016). Both theoretical and empirical research have suggested that the loading mechanism in local ensembles could be achieved through combined effects of synaptic depression and recovery (Markram and Tsodyks, 1996; Tsodyks and Markram, 1997). Furthermore, the loading in the brain is thought to fluctuate on a much slower time-scale than ensemble activity, which could have profound impacts on the dynamics of the fast ensemble activity on a long temporal scale (Roberts et al., 2017a). The classic brain criticality cannot address the dynamics specific to *quasi*-critical systems.

1.4.5 Why is bistability relevant to neuronal criticality?

Biological organisms can steadily operate in bistable mode, which is thought to reflect an abstract and universal building motif favourable to adaptation and survival (Bednarz et al., 2014; Dubnau and Losick, 2006). In humans,

bistability has been observed in various behaviours (Haken et al., 1985; Kelso, 2012) and perceptions (Cao et al., 2018; Miller et al., 2000). In neurophysiology, bistability is a pervasive class of phenomena. Although type II excitability by and large is bistability (Hodgkin, 1948), the concept of neuronal bistability was first explicitly referring to intraneuronal dynamics, in which a neuron, after firing, dwells in one of two preferred subthreshold states: a hyperpolarized down-state, or a more depolarized up-state (Wilson, 2008; Wilson and Cowan, 1972). Bistability phenomenon was later reported in LFP dynamics across cortical areas in felines (Steriade et al., 1993) and was proposed as an intrinsic property of the brain (Holcman and Tsodyks, 2005).

Henceforth, bistability phenomena have been generally referred to the coexistence of an up and a down state (Chialvo, 2010; Cocchi et al., 2017; Di Santo et al., 2016) and have been documented cross several scales including in spiking activity (Gu et al., 2015; Jercog et al., 2017; Koulakov et al., 2002; Miller and Wang, 2006), in neuronal oscillations during sleep or anesthesia in animals (Mejias et al., 2010; Millman et al., 2010), in switching modes in models and LFP recordings (Heitmann et al., 2017), and in EEG amplitude fluctuations in human resting-state brain activities (Freyer et al., 2011, 2009; Hidalgo et al., 2012). In addition to ensemble bistability, simulated large-scale cortical networks could also show bistable avalanches with coexisting regular (*i.e.*, power-law like) and "Dragon Kings" avalanche events (de Arcangelis, 2012; Kinouchi et al., 2019). Here, the Dragon Kings refer to extremely large avalanches that have a preferred size range and occur much more often than what is expected by a power-law distribution (Sornette and Ouillon, 2012).

In canonical ensemble models, the bifurcation mechanism for coexisting unimodal and bistable firing rate dynamics was proposed five decades ago (Wilson and Cowan, 1972), which has been recently revised with supporting evidence from generative models (Cowan et al., 2016). Specifically, bistability was proposed to be a result of the ensemble undergoing a saddle node bifurcation between two stable attractors, whereas unimodal dynamics be a result of the system operating close to the Bogdanov-Takens bifurcation point (Cowan et al., 2016, 2014; di Santo et al., 2018; Izhikevich, 2007). The Bogdanov-Takens point is a marginally stable critical point and suggestive of a wider parameter space for the second order transition to take place, which implies an ensemble does not require fine tuning to be critical-like. While the bifurcation mechanisms described with partial differential equations is important, they offer little insights into the neurophysiological underpinning of unimodal and bistable dynamics, and their links to critical scale-invariance and behavioural relevance.

1.4.6 The possible physiological underpinning of bistability in brain networks

Theoretical work has suggested a possible association between bistability and critical dynamics (Millman et al., 2010). Other theoretical and empirical studies have suggested that neuronal bistability be associated with first order phase transitions (Cocchi et al., 2017; Cowan et al., 2016). A recent modeling study offers a new perspective to the possible physiological underpinning that might drive both unimodal and bistable neuronal dynamics[32] (di Santo et al., 2018). The authors showed that, by manipulating the synaptic resource loading and available synaptic resource, both classic and bistable avalanche dynamics can be observed in a neural field model of Wilson-Cowan ensembles[33]. The authors tuned their network model in a 2-dimensional parameter space. The first parameter reflects the fluctuations in available synaptic resources that controls model to operate along the sub-critical ➔ critical ➔ super-critical axis of classic criticality. The second parameter reflects the fluctuations of resource depletion *vs*. recovery ratio and controls the switching between classic unimodal or bistable critical

[32] This work was motivated by the celebrated Landau-Ginzburg theory in physics that includes spatial dependence to fluctuations and is used as a phenomenological meta-model to study phase transitions in matters (Binney JJ et al., 1993).

[33] Introducing resource loading into a large-scale brain model suggests the assumption that the brain is quasi-critical.

avalanche dynamics. Specifically, when the model is controlled by a large depletion rate, by gradually increasing resource, the model demonstrates classic smooth transition from sub-critical down-state, to critical state, and to super-critical up-state in succession. When the model is controlled by a small depletion rate, by gradually increasing resource, the model demonstrates sub-critical, bistable neuronal avalanches, and super-critical up-state in succession. These observations have offered a promising avenue to further study coexisting unimodal and bistable criticality with plausible physiological basis.

1.4.7 Why studying bistability in ensemble dynamics?

High degree of bistability has been associated with detrimental effects and shifts to catastrophic events seen in a wide range of topics such as in aerodynamical systems (Qi and Zhongke, 2015), ecosystems (Boerlijst et al., 2013; Villa Martín et al., 2015), societies (Díaz, 2017), or coupled signals (Agu and Teramachi, 1978). One would naturally speculate a possible link between resource demand in normal or diseased brain and bistability reflected in electrophysiological signals of spontaneous brain activity. Existing network bistability model (di Santo et al., 2018) addresses bistable neuronal avalanche dynamics but offers no insights to specific loci. On the other hand, normal cognitive functions or neurological diseases are known to differentiate dynamics in distinct brain regions (Jirsa et al., 2014). Therefore, physio-markers for accurately identifying ensemble bistability could be scientifically and clinically useful. On the phenomenological level, it is also important to investigate how bistability in ensemble amplitude fluctuations is related to ensemble critical phenomena such as LRTCs. We hypothesized that the principle giving rise to bistable avalanches should also control bistable criticality in ensemble dynamics. That is, by tuning a slow variable reflecting the resource demand of an ensemble, bistability in its fast-fluctuating activity should progressively emerge from unimodal critical dynamics.

2 Aims

The aim of this thesis is to advance current theory and knowledge about critical bistability and large-scale synchrony in neuronal dynamics (PART ONE, Figure 4) and to make crucial contributions to method developments for studying functional connectivity using MEG/EEG (PART TWO, Figure 4).

PART ONE (empirical)

- **Study I (Bistability)** We aimed to addresses the mechanisms that generates critical bistability in neuronal ensemble dynamics and to investigate the functional relevance of neuronal bistability. The expected results will link critical bistability and the classic criticality hypothesis into a unified theoretical framework, which is currently missing.
- **Study II (HFO Synch**) We aimed to locate and define topologically the connectivity of long-range, high frequency oscillation (>100 Hz, HFO) synchrony using human intracerebral recordings. We also aimed to investigate the behavioural relevance of HFO synchrony.

PART TWO (methodological)

- **Study III (Ghost)** We aimed to formally describe and raise awareness to a severe yet not well documented ghost interactions (SIs) problem in MEG/EEG connectivity.
- **Study IV–V (Hyperedge)** We aimed to obtain simulation-informed knowledge of signal mixing between reconstructed MEG/EEG sources, with which we will bundle true interactions and false-positive SIs into "hyperedges", thereby to significantly suppress the SIs and improve interpretability of MEG/EEG connectivity.

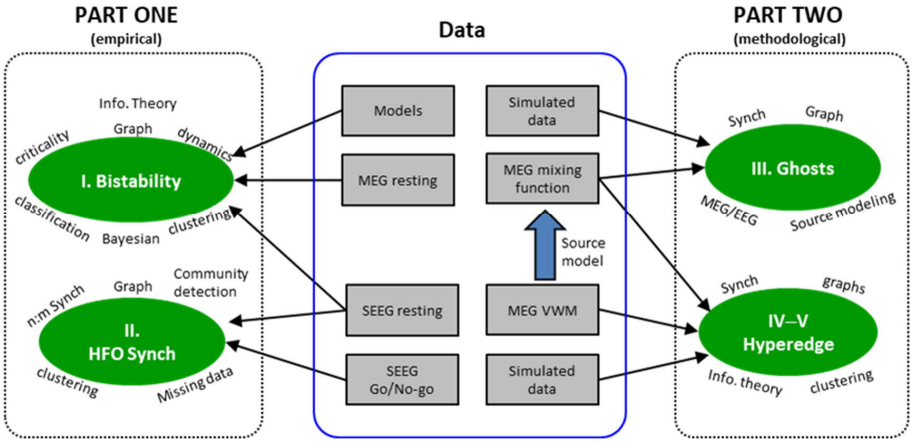

Figure 4 Thesis projects (in green), datasets, the theoretical frameworks, and the tools utilized.

3 Methods

The purpose of computing is insight, not numbers – Richard Hamming

3.1 Canonical and generative model (Study I)

In neurosciences, the Hopf bifurcation is recognized for its universality and simplicity, and it well predicts dynamics in a wide classes of data ranging from genetics (Freyer et al., 2012; Lebar et al., 2014; Oyarzun and Chaves, 2015), neuronal oscillations (Freyer et al., 2009; Heitmann et al., 2017), to sensation and perceptions (Pérez-Cervera et al., 2019; Rankin et al., 2014). The canonical model of Hopf bifurcation could be written as (Freyer et al., 2012):

$$\dot{r} = -r^5 + \lambda r^3 + \beta r + \eta[(1-\rho)\xi_a(t) + \rho r \xi_m(t)] \quad (1)$$

here $\dot{r}$ is the time derivative of a variable r (*e.g.*, a real number reflects neuronal activity); λ is the shape parameter and β the bifurcation parameter; η scales the overall influence of noise; where $\xi_a(t)$ and $\xi_m(t)$ are additive and state-dependent noise, respectively, and $\xi_a(t)$ and $\xi_m(t)$ are uncorrelated and independent Gaussian time series with zero mean and unit variance; the key parameter ρ weights the influence of state-dependent noise. Different combinations of λ and β result in either super-critical or sub-critical bifurcation (details in (Freyer et al., 2012)), which are associated with continuous second order or discontinuous first order phase transition, respectively (Cocchi et al., 2017; Di Santo et al., 2016; Kim et al., 1997).

To generate local synchrony dynamics, we build a stochastic Kuramoto model that consists of 200 fully coupled oscillators, each of which represents the collective activity of a number of neurons on a finer spatial scale (Breakspear et al., 2010). We introduce a stated-dependent noise ρ as a local positive feedback to the Kuramoto mode, which, as predicted by the canonical Hopf bifurcation should be able to generate both the classic unimodal and bistable dynamics (Breakspear, 2017; Freyer et al., 2012; Izhikevich, 2007). In the Kuramoto model, the dynamics of each oscillator n is a scalar phase time series $\theta_n (\theta \in 0{:}2\pi)$, and a population of such oscillators can be represented by a set of coupled differential equations in a simple form as:

$$\dot{\theta}_n = \omega_n + K_n + Z_n \quad (2)$$

where, for any given oscillator n, $\dot{\theta}_n$ is the time derivative of its phase time series θ_n, ω_n the natural frequency of n, K_n the coupling between n and rest oscillators of the network, and Z_n the noise term. The degree of synchrony of the population, or order parameter or mean field, embodies the outcome of tripartite competition for controlling the collective behaviours of all oscillators: ω_n and Z_n are desynchronizing factors whereas K_n is the synchronizing factor. Here, ω_n follows a normal distribution with mean of zero (Hz), meaning without loss of generality, the system can be observed on a rotating phase plan with arbitrary angular velocity. The coupling term K_n is defined as the n-th oscillator adjusts its phase according to interactions with all the rest oscillators in the system through pair-wise phase interaction function:

$$K_n = \frac{\kappa}{N} \sum_{n=1}^{N} \sin(\theta_n - \theta_m) \quad (3)$$

where κ is a scalar number representing coupling strength, N is number of oscillators (200 in our simulation). For simplicity, here we use a fully coupled network to avoid other families of emerging dynamics due to nodal or network structural disorders, *e.g.*, Griffiths phase (Moretti and Muñoz, 2013; Muñoz et al., 2010). In addition, we found that with a Gaussian nodal-weight distribution, the model behaved nearly identically to the fully coupled networks. Furthermore, we modify the noise term in line with the Hopf bifurcation (eq.1) as:

$$Z_n = \eta[(1-\rho)\zeta_a(t) + \rho(R_{MAX} - R)\,\zeta_m(t)] \quad (4)$$

where ρ is the weight of the state-depend noise; R_{max} is the maximal mean field the population can reach (*e.g.*, slightly below 1 due to the presence of noise) and R is the mean field (a scalar) that quantifies the degree of synchrony of the population at given time point t:

$$R(t) = \left|\frac{1}{N}\sum_{n=1}^{N} e^{\theta_n(t)}\right| \quad (5)$$

when viewing R from the complex phase plan, it essentially is the centroid vector of the population phase distribution; if the whole population is in full synchrony, $R \rightarrow 1$; when there is no synchrony, $R \rightarrow 0$ (see insets, Fig. 5F). For a local ensemble, the classic critical dynamics is associated with a *supercritical* Hopf bifurcation (Freyer et al., 2012; Izhikevich, 2007). Gradually increasing the coupling between units, the ensemble would reach the critical point, where the quiescent fix point (subcritical) loses stability where a smooth transition to a critical (active) phase takes place. The synchrony of an ensemble in such classic critical state follows a Gaussian distribution (Freyer et al., 2012, 2009; Roberts et al., 2015). When undergoing a *subcritical* Hopf bifurcation, the ensemble demonstrates bistable criticality. In this scenario, a seemingly quiescent ensemble could suddenly and unpredictably become supercritical (hyperactive) – before quiescent phase losing its stability. Thus, synchrony follows a bimodal distribution, or in some cases heavily tail, implying underlying hysteresis. When coupling is strong, the ensemble would only dwells on hyperactive phase – resembling epileptic seizures.

3.2 MEG resting-state recording (Study I)

We recorded 10 minutes of resting-state brain activity using magnetoencephalographic (MEG) from 18 subjects (11 males, 31.7±10.5, mean±std, yeas of age) at the BioMag Laboratory, HUS Medical Imaging Center, Helsinki Finland. Subjects were seated in a dimly lit room and instructed to focus on a cross on the screen in front of them. Recordings were carried out at Meilahti hospital in Helsinki (detailed in Study I Supp. Material). All subjects were free of neurological conditions. We also assessed working memory, attention and executive functions in these subjects with a battery of neuropsychological tests. These included: Zoo Map Time, Toulouse-Pieron test (TP), Digit Symbol Coding test, Zoo Map Plan, Digit Span forward and backward (BackDigits and ForwDigits, respectively), Letter-Number Sequencing (LNS), Trail Making Test parts A and B (TMT-A, TMT-B). Some subjects had missing/invalid behavioural scores, and we reported the neuro-behavioural correlations with dataset that had at least 16 valid subjects' scores. All subjects gave written consent and the study was performed according to the Declaration of Helsinki.

3.3 SEEG Resting-state recording (Study I, II)

We recorded 10 minutes of SEEG resting-state local-field potential (LFP) signals from 92 drug-resistant focal epilepsy patients. Among them, 25 subjects were later excluded from analyses due to previous brain surgery such as temporal lobotomy or an MRI-identified cortical malformation (Study II Suppl. Table 1). We used a 192-channel SEEG amplifier system (NIHON-KOHDEN NEUROFAX-1100) with a sampling rate of 1 kHz.

The platinum–iridium, multi-lead electrodes used in recording have 8 to 15 contacts, and each of which was 2 mm long and 0.8 mm thick with an inter-contact border-to-border distance of 1.5 mm (DIXI medical, Besancon, France). The implantation locations and amounts of electrodes varied in subjects according to individual surgical requirements. On average, each subject had 17 ± 3 (mean ± SD) shafts (range 9–23) with a total of 153 ± 20 electrode contacts (range 122–184, left hemisphere: 66 ± 54, right hemisphere: 47 ± 55 contacts, grey-matter contacts: 113 ± 16.2). The final cohort of 67 patients yielded a total of 7068 non-epileptic grey matter contacts (113 ± 16.2 per subject, mean ± SD, range 70-152) that gave a dense sampling across all neocortical regions and of seven canonical functional brain systems defined by fMRI intrinsic connectivity mapping (Schaefer et al., 2017; Yeo et al., 2011). Before electrode implantation, the subjects gave written informed consent for participation in research studies and for publication of results pertaining to their data. This study was approved by the ethical committee (ID 939) of the Niguarda "Ca' Granda" Hospital, Milan, and was performed according to the Declaration of Helsinki.

3.4 Simulation for study III

To model signal spread in the 2D grid sources, the measured source signals are simulated as an instantaneous linear mixture of underlying source time series, which is implemented in two steps. First, we model the underlying 'true' source time series as follows: one-dimensional random Gaussian time series n_i are linearly mixed using mixing parameters c_A and c_θ. The mixed time series are filtered using Morlet wavelets, and time series to be used as instantaneous amplitudes and phases are generated as:

$$A_x(t) = \left|F\left(n_1(t) + c_A n_2(t)\right)\right| = \sqrt{re\left(F\left(n_1(t) + c_A n_2(t)\right)\right)^2 + im\left(F\left(n_1(t) + c_A n_2(t)\right)\right)^2} \quad (6)$$

$$A_y(t) = \left|F\left(n_2(t) + c_A n_1(t)\right)\right| \quad (7)$$

$$\theta_x(t) = phase\left(F\left(n_3(t) + c_\theta n_4(t)\right)\right) = atan\left(\frac{im\left(F\left(n_3(t)+c_\theta n_4(t)\right)\right)}{re\left(F\left(n_3(t)+c_\theta n_4(t)\right)\right)}\right) \quad (8)$$

$$\theta_y(t) = phase\left(F\left(n_4(t) + c_\theta n_3(t)\right)\right) \quad (9)$$

where n_i is a vector containing (N=50,000) samples of Gaussian white noise from i^{th} realization; F denotes complex Morlet wavelet transform with basis function $\psi(x) = e^{-x^2/2}\cos(5x)$; c_A and c_θ are scalar mixing parameters; *re*() and *im*() are the real and imaginary part of complex number, respectively; A and θ are the amplitudes and phases, respectively. This approach allows us to model phase and amplitude interactions separately (Bruns et al., 2000).

Next, the amplitudes and phases (Eqs. 6–9) are used to assemble complex-valued time series as follows:

$$x(t) = A_x(t)e^{i\theta_x(t)} + mA_y(t)e^{i(\theta_y(t)+\phi_{xy})} \quad (10)$$

$$y(t) = A_y(t)e^{i(\theta_y(t)+\phi_{xy})} + mA_x(t)e^{i\theta_x(t)} \quad (11)$$

where m is the spatial mixing parameter, modelling the instantaneous signal spread; ϕ_{xy} is the phase shift [-π, π], controlling the mean phase difference across sources x and y.

To demonstrate the spatial effects of signal spread, we simulate source signals in a 13×13 square grid layout, with inter-source distance d_g. The signal spread was modelled as a truncated 2-dimensional Gaussian function with parameters $\mu = 0$ and $\sigma = d_g$ up to a range of three standard deviations σ so that,

$$m(d) = \frac{1}{\sigma\sqrt{2\pi}} e^{-\frac{(d-\mu)^2}{2\sigma^2}}, \qquad if\ d \leq 3\sigma \tag{12}$$

$$m(d) = 0 \qquad else$$

In addition to the simulations on the 2D source grid model, we investigate the effect of spurious synchrony in more realistic source-space derived from real MEG experiment. We simulate two correlated cortical parcels whereas all other cortical parcels are uncorrelated time series with equal amplitude distributions. Thus, the parcel pair with simulated correlation are different from other parcels in terms of their correlation. We next perform a virtual MEG/EEG experiment by forward-modeling simulated source activity, followed by minimum-norm source reconstruction. We next estimated all-to-all cortical interactions and plotted on a flattened brain surface (Figure 14C).

3.5 Simulation for study IV

Simulation of the parcel time-series X of 1,000 random ground-truth graphs on a 400-parcel cortical source-space (J. M. Palva et al., 2010a) of the Destrieux atlas (Destrieux et al., 2010; Fischl et al., 2002). Virtual MEG measurements and source reconstruction were performed by forward- and inverse-modeling X into the reconstructed time series $\hat{X}$ (detailed in Study V). The forward- and inverse-operators used here were derived from the visual working memory experiment described below. Finally, all-to-all FC of $\hat{X}$ was estimated with iPLV.

Each ground-truth graph contained 200 randomly connected nodes so that each node was connected only to a single other node. The narrow band time series $X(t, f_0) \in \mathbb{R}^{m \times n}$ (m=1,000 independent samples, n=400 parcels) of each ground-truth graph was simulated as follows. First, 400 parcels were first randomly divided into two groups V_1 and V_2 as source and target nodes. Next, the nodes from V_1 and V_2 were next randomly paired to create 200 edges E, thus for each edge $e_k = \{(v_1^{(i)}, v_2^{(j)}) \in E |\ v_1^{(i)} \in V_1;\ v_2^{(j)} \in V_2\}$, $1 \leq k \leq 200$. The time series of 200 source nodes in V_1 were obtained by convoluting uncorrelated white noise time series with Morlet wavelets $w(t, f_0)$, f_0 = 10 Hz, Morlet $m = 5$, f_s = 100 Hz. For each edge $e_k(v_1^{(i)}, v_2^{(j)})$, the time series of the target node $v_2^{(j)}$ was simulated to have a correlation coefficient of 0.9 with the time series of source node $v_1^{(j)}$ delayed by 3 samples. $X(t, f_0)$ were finally decimated into 1,000 independent samples before forward and inverse-modeling. To identify significant iPLV edges in the ground-truth graphs, we also estimated null hypothesis graphs G_{rawH0} *by* simulating uncorrelated time series $X_{H0} \in \mathbb{R}^{m \times n}$ (m=1,000, n=400 parcels) and estimating their *iPLV* as done for the ground-truth graphs. A range of five thresholds was obtained from G_{rawH0} that corresponded to significance levels ranging from relaxed to strict, *i.e.*, $T_{iPLV} = -log(p\text{-}value) \in \{1.3, 2, 3, 4, 5\}$.

3.6 MEG data preprocessing

3.6.1 MEG Source-reconstruction

We used Maxfilter with temporal signal space separation (tSSS) (Elekta Neuromag Ltd., Finland) to suppress extra-cranial noise in sensors and to interpolate bad channels (Taulu and Simola, 2006). We then used independent component analysis (Matlab Fieldtrip toolbox, http://fieldtrip.fcdonders.nl) to identify and extract

components that were correlated with ocular (identified using the EOG signal), heart-beat (identified using the magnetometer signal as a reference) or muscle artefacts (Oostenveld et al., 2011). We reconstructed MEG sources using the FreeSurfer software (http://surfer.nmr.mgh.harvard.edu/) for volumetric segmentation of MRI data, surface reconstruction, flattening, cortical parcellation, and neuroanatomical labeling with the Schaefer-2017 atlas (Schaefer et al., 2017) that favours functional networks topology over structural (gyral) topology (Destrieux et al., 2010). Each of the Schaefer-parcel belongs to a functional system (Yeo et al., 2011) which informed later systems-level analysis. We used the MNE software package to create head conductivity models and cortically constrained source models with 5000-7500 sources per subject and for the MEG-MRI co-localization and for the preparation of the forward and inverse operators (Hamalainen and Sarvas, 1989; Hämäläinen and Ilmoniemi, 1994). For Study I, we obtained a cortical parcellation of 400 Schaefer-parcels using reconstruction-accuracy optimized source-vertex-to-parcel collapsing method (Korhonen et al., 2014). For simulations used in Study III and IV, we obtained a cortical parcellation of 400 Destrieux-parcels using reconstruction-accuracy optimized source-vertex-to-parcel collapsing method (Korhonen et al., 2014).

3.6.2 Forward and inverse modeling

Consider a data matrix $X = \{x_{(1)}, x_{(2)}, \ldots, x_{(n)}\} \in \mathbb{R}^{n \times t}$ representing narrow-band time series of t samples from n neuronal populations. MEG recording of these neuronal signals linearly projects X to sensor-space (Hämäläinen and Ilmoniemi, 1994):

$$Y = \Gamma X + \varepsilon \tag{13}$$

where $Y \in \mathbb{R}^{s \times t}$ represents the forward-modeled time series from s sensors ($n > s$). Here, $\Gamma \in \mathbb{R}^{s \times n}$ is the forward operator (or the lead field) and $\varepsilon \in \mathbb{R}^{s \times t}$ is the model prediction error derived from measurement noise. Next, Y can be projected back into the source-space using L^2 minimum-norm estimation (MNE) based inverse modeling:

$$\hat{X} = WY = R\Gamma^T(\Gamma R \Gamma^T + \lambda^2 \chi)^{-1} Y \tag{14}$$

where $W \in \mathbb{R}^{n \times s}$ is the inverse operator (sources × sensors), the regularization parameter $\lambda^2 = 0.1$, R is the source covariance matrix, and χ is the noise covariance matrix computed from empty room recording. After inverse modeling, the source time series are collapsed into parcel time series for a cortical parcellation with 50–400 parcels using a reconstruction-accuracy optimized collapsing (Korhonen et al., 2014) and a maximum resolution of 400 parcels covering the whole cortex.

3.6.3 Quantifying mixing properties of the MEG sources

In MEG or EEG source connectivity studies, a resolution matrix $P = W\Gamma$ ($P \in \mathbb{R}^{n \times n}$) is often used to describe the relationship between true signals and modeled signals from n sources in the absence of noise (Farahibozorg et al., 2018; Hauk et al., 2011; Hauk and Stenroos, 2014; Liu et al., 2002). In P, each diagonal element quantifies the sensitivity for estimating signals from that source. Each row of P is the "cross-talk" function (CTF) that describes the amount of mixing between one source and all other sources. Each column of P is a "point-spread" function (PSFs) that describes how the modeled signal from any one source is spread across all other sources.

We used a fidelity (reconstruction accuracy) optimized cortical parcellation (Korhonen et al., 2014), for which we approximated the resolution matrix P numerically with a mixing matrix A_{mix} of dimension $n \times n$ parcels. Each element of A_{mix} is a *mixing function* (f_{mix}) that characterizes the signal mixing between two parcels. For uncorrelated true source signals, the magnitude of zero-lag correlations between reconstructed signals measures

the forward- and inverse-transform caused mixing between the sources. Thus, f_{mix} can be quantified by the zero-lag correlation between parcel time series estimated using simulated MEG/EEG measurements of uncorrelated source noise.

We first generate uncorrelated signals $X_0 \in \mathbb{R}^{n \times t}$, t samples for n parcels, and forward transform them to obtain sensor signals Y_0. We next inverse transform Y_0 to obtain reconstructed signals $\hat{X}_0$ In this process, the reconstructed signals $\hat{x}_0(v_i)$, $\hat{x}_0(v_j)$ of any two nearby sources v_i and v_j become correlated to a certain degree due to mixing. Thus, the mixing from the simulated "*true*" signal $x_0(v_i)$ to the *reconstructed* signal $\hat{x}_0(v_j)$ can be quantified as:

$$f_{mix}(v_i, v_j) = \left| re(cPLV(x_0(v_i), \hat{x}_0(v_j))) \right| \quad (15)$$

where *re*() denotes the real part of a complex number and *cPLV* is the complex-valued phase locking value (S. Palva and Palva, 2012):

$$cPLV(\mathrm{A},\mathrm{B}) = \frac{1}{T}\sum_{t=1}^{T}\left[e^{i(\theta_A(t)-\theta_B(t))}\right] = \frac{1}{T}\sum_{t=1}^{T}\left[\frac{S_A S_B^*}{|S_A||S_B|}\right] \quad (16)$$

where T denotes the number of samples, θ_A and θ_B are the instantaneous phases of signal A and B; S_A and S_A are complex-valued narrow-band signals from A and B, and z^* is the complex conjugate of z. Because mixing is instantaneous, re(cPLV*(A,B)*) captures all correlations caused by mixing. For parcel pairs that do not become correlated by signal mixing, f_{mix} is near zero. For parcel pairs influenced by signal mixing, $f_{mix} >> 0$ and reaches 1 for complete mixing. It is important to note that although we here measured mixing by phase correlation, practically identical quantification would be achieved by, for example, the correlation coefficient as well as by deriving the mixing values analytically from CTFs and PSFs. A_{mix} is thus interaction-metric independent.

3.7 SEEG data preprocessing

We excluded electrode contacts (1.3±1.2, range 0–10, contacts) that demonstrate non-physiological activity from analyses. We employed a novel referencing scheme for SEEG data where electrodes in grey-matter were referenced by the contacts located in the closest white-matter (cWM) (Arnulfo et al., 2015). This referencing scheme is proven optimal for preserving phase relationship between SEEG contact data. The final size of channels analyzed is on average 110±25 for each subject and 7491 in total. To validate some results such as those that in Study II, we also performed analyses with bipolar referenced SEEG data.

Prior to narrow-band analyses, SEEG contact time series were low-pass filtered with FIR filter with cut-off at 440Hz and stop-band at 500Hz (60Hz transition band, -6dB suppression at 475dB, maximal ripples in pass-band 2%). 50 Hz line-noise and its harmonics were excluded with a band-stop FIR filter with 53dB suppression and 1Hz band-stop widths. The LP filtered data were then separated into narrow frequency bands with 50 Morlet wavelets of (width $m = 7.5$) and frequency ranging from 2Hz to 450Hz.

Epileptic events such as interictal spikes are characterized by high-amplitude fast temporal dynamics as well as by widespread spatial diffusion. Due to possible filtering artefacts around epileptic spikes and the resultant increase in synchrony, we discarded periods of 500ms containing Interictal Epileptic Events (IIE). We defined such periods as the temporal windows where at least 10% of cortical contacts demonstrated abnormal concurrent sharp peaks in more than half of the 18 frequency bands. Such episodes were excluded from within- and cross-frequency synchrony analysis. To identify such periods, we divided the signal in multiple 500 ms non-

overlapping windows and detected IIE events in amplitude envelopes as the time point exceeding 5 times the standard deviation greater than the channel mean amplitude.

3.7.1 Defining epileptic zones in SEEG

The epileptogenic and seizure propagation zone are identified by clinical experts by visual analysis of the SEEG traces (Cardinale et al., 2013a; M Cossu et al., 2005). Epileptogenic areas are the hypothetical brain areas that are necessary and sufficient for the origin and early organization of the epileptic activities (Luders et al., 1993), from where contacts recording often show low voltage fast discharge or spike and wave events at seizure onset. Seizure propagation area are recruited during the seizure evolution, but they do not generate seizures (Bartolomei et al., 2013; Proix et al., 2017), from where contact recording show delayed, rhythmic modifications after seizure initiation in the epileptogenic areas. In this study, we combine epileptogenic and propagation areas as the epileptogenic zone (EZ) to distinguish from the rest of brain areas that are referred to as putative healthy zones (nEZ).

3.8 Narrow-band filtering

In Study I, the broadband time series from MEG parcels or cWM-referenced SEEG contacts were filtered into narrow-band time series using a bank of 20 Morlet filters with $m = 5$ and log-linearly spaced center frequencies ranging from 2 to 225 Hz. For group-level analysis of anatomical specificity and behavioural correlations, subject neuronal estimates (*e.g.*, LRTCs, bistability index) were morphed from 400 Schaefer-parcels into 100 Schaefer-parcels.

For Study II, Prior to the main analysis, SEEG time series were low-pass filtered with FIR filter with cut-off at 440 Hz and stop-band at 500Hz (60Hz transition band, -6dB suppression at 475dB, maximal ripples in passband 2%). 50 Hz line-noise and its harmonics were excluded with a band-stop FIR filter with 53dB suppression and 1Hz band-stop widths. The LP filtered data were then separated into narrow frequency bands with 50 Morlet wavelets of (width $m = 7.5$) and frequency ranging from 2 to 450Hz with equal $\log_{10}$ spacing. Epileptic events such as interictal spikes are characterized by high-amplitude fast temporal dynamics and widespread spatial diffusion.

3.9 Criticality and synchrony metrics

3.9.1 Theory: the memory of a physiological signal

The "memory" of a physiological signals, for instance in narrow-band ensemble amplitude fluctuations, refers to, in the time domain, the present or recent past could predict future in both short-term and long-term. At least two classes of physiological signals demonstrate long-range temporal correlations (LRTCs) reflecting the said memory process, and they are non-stationary fractional Brownian motions (fBm) and stationary fractional Gaussian noises (fGn) (Eke et al., 2002, 2000). Here, a stationary state refers to when descriptive statistics such as the mean, variance, and autocorrelations of a discretely sampled physiological time series[34] remains constant during the period of observation (Eke et al., 2000). For example, a Gaussian white (Gw) noise is a stationery process, whereas the Brownian motion (Bm) obtained by integrating the same Gw process is non-stationary.

[34] A time series X(t) is an array of discrete data points obtained by sampling a continuous signal at a fixed interval Δt, *i.e.*, sampling frequency $1/\Delta t$.

The fBm is a special case of Bm that have correlated increments across temporal scales. A positive correlation in a fBm process indicates persistency in LRTC, which expects, across temporal scales, an increasing trend in the past to be followed by an increasing trend in the future. On the other hand, a negative correlation in a fBm process indicates anti-persistency, which predicts, across temporal scales, an increasing trend in the past is likely to be followed by a decrease in the future. This fractal-like self-similarity across temporal scales in 1D data is referred to as self-affinity due to the different units of the *x* and *y* axis.

The fGn process is a series of successive increments in an fBm (Eke et al., 2002). This means that each fBm has its corresponding fGn, and both bear the same LRTCs which can be characterized using a variety of metrics including the classic Hurst exponent, fractal dimension, power-spectrum, and the scaling exponent obtained using dispersion analysis or linear detrend fluctuation analysis (DFA). Conventionally, the Hurst exponent (*H*) (Hurst, 1951) assesses the self-affine feature of LRTCs in a fGn or fBm signals. Mathematically, the *H* represents the asymptotic behaviour of the normalized range as a function of the time span as follows:

$$E\left[\frac{R(n)}{S(n)}\right] \propto Cn^H \qquad (17)$$

where $E[]$ is expected value, $R(n)$ and $S(n)$ the range and standard deviation of demeaned time series with observation length of n samples of out total N samples (n=N, N/2, N/4…), $\propto$ denotes direct proportionality, C is a constant, H is the Hurst exponent. The fractal dimension based on box-counting approach is written as (Eke et al., 2000):

$$N \propto \varepsilon^D \qquad (18)$$

which predicts that the quantity of observation (N) scales as a function of the measurement size (ε) by power of D. The H quantifies how likely that an event in a process is followed by a similar event, whereas D reflects the expanding symmetry of mono-fractal structure[35]. For 1D physiological signals, $1 < D < 2$ and $H = 2 - D$. A H smaller than 0.5 indicates anti-persistency, whereas a H greater than 0.5 indicates persistency. Visually, a H exponent close to one (*i.e.*, high degree of anti-persistency), the time series is very "rough" (Mandelbrot, 1983) or "hairy" (Eke et al., 2002). Stationary fGn and its corresponding fBm noise has $H = 0.5$, because fGn is a series of independent numbers and fBm has uncorrelated increments. A H exponent of one characterize pink noises.

3.9.2 Characterizing long-range temporal correlations

In study I, we used the exponent obtained with DFA for assessing the LRTCs of narrow-band neuronal amplitude fluctuations or the Kuramoto model mean field time series. The DFA exponent is a proxy of Hurst exponent and reflects the self-affinity in how fast the overall root mean square of local fluctuations after linear detrending grows with increasing sampling period width. Following the definition by (Hardstone et al., 2012), the process, Y, is self-affine if for all windows of length t:

$$Y(Lt) \equiv L^H Y(t) \qquad (19)$$

[35] An example is the cyclic Weierstrass processes, in which power is concentrated at discrete frequencies following a power-law PSD. A reference is the non-periodic processes like Gaussian white noise, the power is equally distributed across all possible frequencies.

where: $Y(Lt)$ and $Y(t)$ are values of a process at time windows of length Lt and t ($L > 0$), respectively; H is the Hurst exponent obtained with DFA; $\equiv$ denotes the standard deviations on both sides of the equation are identical.

In empirical data, the power law often holds only in the upper tail, *e.g.*, between a lower boundary cutoff t_{min} and an upper boundary t_{max} of t (Clauset et al., 2009; Virkar and Clauset, 2014). The selection of t_{min} has a strong impact on the estimated exponent. For example, choosing a too small t_m may positively bias the DFA exponent due to high non-stationarity in narrow-band amplitudes. On the other hand, selecting a too large t_{min} means discarding good data, which results in increased statistical uncertainty and not having enough range to claim legitimate power law scaling (Stumpf and Porter, 2012). Therefore, we prefer to be slightly conservative that is throwing away some good data and still having at least 2 orders on the x axis for fitting power law. Thus, we choose 20-cycle as t_{min} across frequencies (*e.g.*, $t_{min,10\,Hz} = 2$ s, $t_{min,\,40\,Hz} = 0.5$ s) to avoid the non-stationary regime, and 120 seconds (20% of total recording) as t_{max}.

3.9.3 Characterizing bistability using the BiS index

The bistability index (BiS) of a power time series (R^2) is the result of model comparison between a bimodal or unimodal fit of its probability distribution function (*pdf*); a large BiS means that the observed *pdf* is better fitted with bimodal, and when BiS → 0 the *pdf* is better described as unimodal. Here, we followed the approach used in (Freyer et al., 2012; Roberts et al., 2015) to compute BiS. First, to find the *pdf* of power time series R^2, we partition observation of R^2 into 200 equal-distance bins and then count the number of observations in each bin. Here, R^2 refers to the square of Kuramoto model mean field or narrow-band frequency amplitude time series of MEG and SEEG data. Next, we used the maximum likelihood estimate (MLE) to fit a single-exponential function (the square of a Gaussian process follows an exponential *pdf*):

$$P_x(x) = \gamma e^{-\gamma x} \tag{20}$$

and a bi-exponential function:

$$P_x(x) = \delta\gamma_1 e^{-\gamma_1 x} - (1-\delta)\gamma_2 e^{-\gamma_2 x} \tag{21}$$

where γ_1 and γ_2 are two exponents and δ is the weighting factor.

Next, we compute the Bayesian information criterion (BIC) for the said single- and bi-exponential fit using

$$BIC = ln(n)k - 2ln(\hat{L}) \tag{22}$$

where n is the number of samples; $\hat{L}$ is the likelihood function; k is the number of parameters: 1 for single-exponential BIC_{Exp} and 3 for bi-exponential model BIC_{biE} – thus BIC imposes a penalty to model complexity (Wit et al., 2012) because the bi-exponential distribution has two more parameters (second exponents and the weight δ) than a simple exponential distribution. Last, the BiS is computed as the difference between the two BIC estimates as

$$BiS = BIC_{Exp} - BIC_{biE} \tag{23}$$

Because the better model will yield a small BIC value, BiS should be a large value if the bi-exponential model fit the observed power time series better.

3.9.4 Assessing synchrony between narrow-band signals

Synchrony between two narrow-band neuronal signals band can be quantified in various manners such as measuring the consistency in phase differences, correlation of amplitude envelopes, or on a combination of both (Bastos and Schoffelen, 2016). Here, we quantified phase interactions with the phase-locking value (PLV), weighted phase lag index (wPLI), and amplitude interactions with correlation coefficient (CC) of amplitude envelopes. In addition, we used the imaginary part of the complex-valued PLV (iPLV) and the CC of orthogonalized amplitude envelopes (oCC) to account for the effects of instantaneous linear mixing.

The complex valued phase-locking value *(*cPLV*)* is defined as the magnitude of mean complex phase difference between amplitude-normalized source time courses (S. Palva and Palva, 2012),

$$cPLV = \sum_t e^{i\left(\theta_x(t)-\theta_y(t)\right)}/N \qquad (24)$$

where N is the number of samples; $\theta_x(t)$ and $\theta_y(t)$ are the phases of $x(t)$ and y(t), respectively. The phase locking value (PLV) is defined as:

$$PLV = |cPLV| \qquad (25)$$

and the imaginary part of phase locking value ($iPLV$):

$$iPLV = |im(cPLV)| \qquad (26)$$

Theoretically, PLV compares to iPLV are as coherence compares to the imaginary part of coherency[26]. Nevertheless, it is important to keep in mind that the reliability of phase estimation inherently depends on SNR and may generally be more accurate in the presence of higher signal amplitudes (J. M. Palva et al., 2010a). Using the imaginary part, and thus discarding all real-valued contributions to the estimated interactions, effectively discards all zero-lag interactions, most of which are caused by instantaneous mixing and thus are considered detrimental to correlation estimates.

Amplitude correlations were quantified using the Pearson correlation coefficient (CC) between amplitude envelopes of $x(t)$ and $y(t)$, $A_x(t)$ and $A_y(t)$,

$$CC = \frac{N^{-1}\sum_t\left(A_x(t)-\mu_{A_x}\right)\left(A_y(t)-\mu_{A_y}\right)}{\sigma_{A_x}\sigma_{A_y}} = corr\left(A_x, A_y\right) \qquad (27)$$

where N is the number of samples in signals $x(t)$ and $y(t)$; μ_{Ax} and σ_{Ax} refer to the average and standard deviation of A_x over time, respectively.

Linear mixing between two signals $x(t)$ and $y(t)$ also affects the correlation between their amplitude envelopes. There are two slightly different approaches for attenuating mixing effects in amplitude correlations (Brookes et al., 2012; Hipp et al., 2012), of which both involve the orthogonalization of two amplitudes prior to estimating CC. The orthogonalization removes all linear contribution from signal *x(t)* to signal *y(t)*, or vice versa, provided that the signals are Gaussian—residual zero-lag mixing may remain for non-Gaussian signals (Brookes et al., 2014). In the time domain, orthogonalization of signal y with respect to signal x is achieved by (Brookes et al., 2012):

$$y^{\perp}(t) = y(t) - x(t)[\boldsymbol{x}^{+}\boldsymbol{y}] \qquad (28)$$

where $\boldsymbol{x}^+$ is the pseudoinverse of the vector $\boldsymbol{x}$. Alternatively, orthogonalization can be performed in frequency domain (Hipp et al., 2012):

$$Y^{\perp}(\omega) = im\left(Y(\omega)\frac{X(\omega)^*}{|X(\omega)|}\right) \quad (29)$$

where * denotes complex conjugation.

The orthogonalized CC (oCC) is then computed as CC after orthogonalizing two amplitude envelopes,

$$oCC = \left(corr\left(A_x, A_{y^{\perp}}\right) + corr\left(A_y, A_{x^{\perp}}\right)\right)/2 \quad (30)$$

Because this seed-based orthogonalization can be performed in two directions, either to obtain $y^{\perp}(t)$ orthogonalized in relation to $x(t)$, or to obtain $x^{\perp}(t)$ orthogonalized in relation to $y(t)$, the final oCC is defined as the average of the two correlation coefficients. Such orthogonalization works, however, only under the assumption of data being normally distributed, which might not be accurate for the typically heavy-tailed oscillation amplitude distributions.

In addition to iPLV, we also use the weighted phase lag index (wPLI) where the sign of the phase difference between two signals is weighted by the magnitude of the imaginary component of the cross-spectrum (Vinck et al., 2011):

$$wPLI = \frac{|E\{im(P_{xy})\}|}{E\{|im(P_{xy})|\}} = \frac{|E\{|im(P_{xy})|sign(im(P_{xy}))\}|}{E\{|im(P_{xy})|\}} \quad (31)$$

where E{} is the expected value, *im*() is the imaginary part of a complex value, P_{xy} is the cross-spectrum, $P_{xy} = x(t)y^*(t)$, x and y are complex signals, and * is complex conjugate.

3.9.5 Cross-frequency phase amplitude coupling

The phase of a slow oscillation modulates the amplitude of a faster rhythm. In turn, the phase of the faster rhythm modulates the amplitude of an even faster one, and so on. Two signals of distinct rhythms are cross-frequency phase-amplitude coupled (PAC) if the phase of a slow neuronal oscillation modulates the amplitude fluctuations of the faster neuronal oscillations (Hülsemann et al., 2019). PAC can be estimated using phase synchronization, Euler's formula, or examining whether the power of fast rhythms is non-uniformly distributed over low-frequency phase (Canolty and Knight, 2010; Hyafil et al., 2015b; Jensen and Colgin, 2007; Jirsa and Müller, 2013; Tort et al., 2010).

The rationale is that if the power fluctuations of fast rhythms are modulated by the phase of the slow oscillations, the fluctuations of these two time-series should be synchronized. In this study, we estimated PAC with the phase locking value (PLV) as:

$$PLV_{PAC} = \left|\frac{1}{N}\sum_{n=1}^{N} e^{i(\theta_{amp}(n) - \theta_{phase}(n))}\right| \quad (32)$$

where $\theta_{amp}(n)$ is the phase time series of the power envelope of fast rhythm; $\theta_{phase}(n)$ is the narrow band phase time series of the slow rhythm. When there is a consistent relationship between these two time-series, the vector length of the mean phase differences (in the polar coordinate across all n samples) should be greater than zero, and a maximum value of 1 indicates perfect coupling. The significance of PAC PLV value was determined in the same manner in individual subjects as we conducted for 1:1 phase synchrony described earlier.

4 Results

… in all disorder (there is) a secret order … – p32, (Jung, 1981).

4.1 Study I: Critical bistability in the brain

Neuronal dynamics exhibit scaling behaviours throughout the spatial and temporal scales in the brain. The scaling behaviours have been thought to reflect brain criticality, which suggests that the brain, like many other complex systems, operate near a second order phase transition. However, when neuronal activity is constrained by resource depletion or limiting mechanisms, the dynamics may become bistable, which is the signature of an underlying discontinuous first order phase transition. Nonetheless, observations of bistability in awake human brain activity have remained scarce, and its functional significance and link to brain criticality unclear.

In this study, we assessed the emergence of bistability in oscillation amplitude dynamics using a generative model. Specifically, we hypothesized that bistability is caused by a high level of state-dependent noise that represents a positive local feedback. We next assessed bistability and long-range temporal correlation (LRTCs) in resting-state human brain activity recorded with magnetoencephalography (MEG) and intra-cranial stereo-encephalography (SEEG). To assess the functional significance of neuronal critical bistability, we inspected correlation between neuronal bistability, LRTCs, and behavioural assessments in healthy subjects. We also evaluated the predictive power of bistability and LRTCs in classifying epileptic pathophysiology.

4.1.1 State-dependent noise induces bistability in ensemble models

We introduced a state-dependent noise ($\boldsymbol{\rho}$) into a Kuramoto model (Figure 5A–B) to test if critical bistability can be induced in its ensemble activity as predicted by the Hopf bifurcation (Breakspear, 2017; Freyer et al., 2012; Izhikevich, 2007). Physiologically, the parameter ρ embodies a local positive feedback equating the slow resource loading mechanism that gives rise to bistability (di Santo et al., 2018; Di Santo et al., 2016). The second control parameter, the coupling strength (κ) of the Kuramoto model, determines how likely are the oscillators in the ensemble to oscillate in unison so that an increase in κ results in higher degree of synchrony which is captured by a larger order ($\boldsymbol{R}$) (Methods). Thus, this testing configuration resembles the 2-dimenstional parameter tuning in H_2O (Fig 3A).

Classic criticality: At small values of ρ, gradually increasing κ caused a monotonic increase in R, and meanwhile R exhibited sub-critical, critical and super-critical dynamics in succession, in which the critical regime is characterized by a long-range temporal correlations (LRTCs) deviating from random walk (*i.e.*, DFA exponent > 0.5, Methods) (Figure 5B, black dashed line in 5C, probability distribution in bottom of 5D , exemplary time series in Figure 5E, corresponding distribution and scaling function of 5E shown in 5G and H, respectively).

Bistability: As ρ increases, R progressively demonstrated bistability (Figure 5B, exemplary time series in 5F) within the critical regime (the area demarcated by solid red and black line in 5C, respectively). Here, bistability was operationalized as the bistability estimate (BiS), which is the model comparison outcome between a Gaussian fit and a bi-exponent fit to the probability function of the power (R^2) of the real valued R time series (Methods). As ρ gradually increases, there was a progressive transition from classic unimodal to bistable critical

dynamics (Figure 5C) as prescribed by the Hopf bifurcation (Figure 5A). Importantly, when in high bestiality phase, the model ensemble became more sensitive to κ to traverse from sub-critical down-state into super-critical up-state (red vector in bottom-left panel Figure 5B, dashed box in top panel, Figure 5D). Thus, to summarize, the model could demonstrate both classic and bistable critical dynamics, which was controlled by the value of parameter ρ, *i.e.*, the strength of local positive feedback.

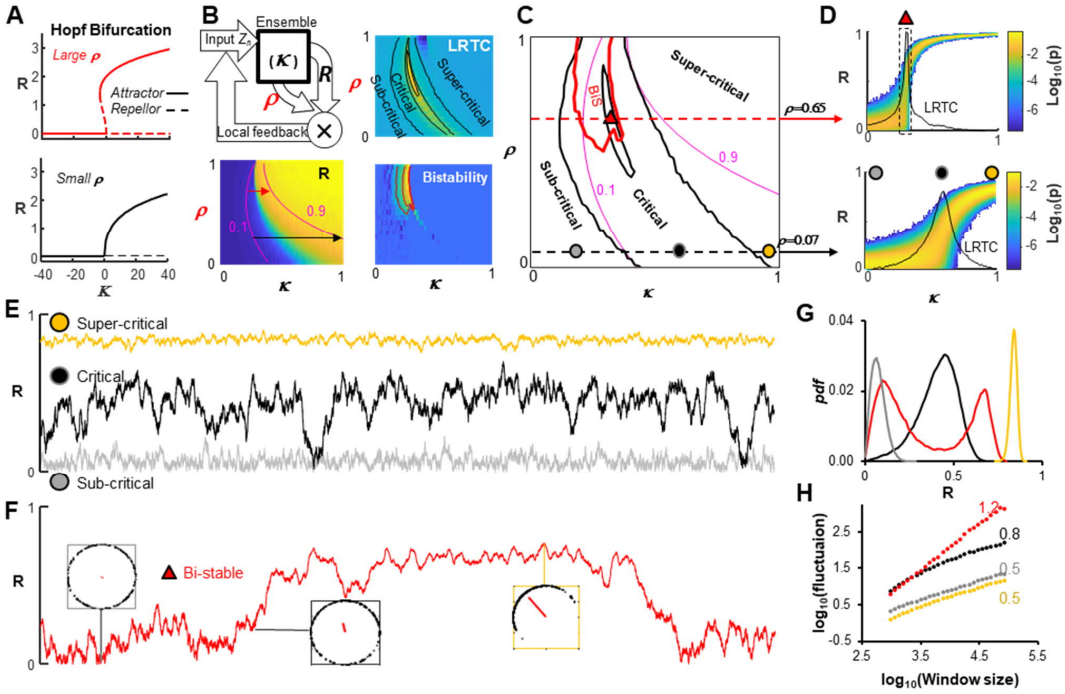

Figure 5 Bistability is caused by strong state-dependency. **(A)** The subcritical and supercritical Hopf bifurcations are associated with bistable and normal dynamics, respectively. (**B**) The Kuramoto order parameter (R) is controlled by state-dependency ρ and coupling κ. Colour maps are time-averaged R, the long-range temporal correlations (LRTCs) estimated using detrended fluctuation analysis of R, and bistability in R time series estimated with the bistability index. Each pixel is the average of 50 independent model realizations. (**C**) Overlapping dynamical regimes based on the maps from **(B). (D)** The probability density of R (z axis) in normal and bistable critical regime – indicated by black and red dashed lines in **(C)**, respectively. **(E–F)** Example Kuramoto R time series in the regimes in **(D)** indicated by corresponding markers; the insets in **(F)** show the moments of oscillators (n=200) in low-, mid- and high-order state (the real-valued order R is indicated by the red vectors). **(G)** Probability density (*pdf*) and (**H**) power law scaling of the detrended fluctuation functions of R time series from **(E–F)** colour-coded.

4.1.2 Neuronal bistability and LRTCs were spatially and spectrally prevalent

To explore the relationship between bistability and LRTCs in spontaneous brain activity, we acquired 10 minutes of resting-state recording from 18 healthy adults using MEG and from 64 focal epilepsy patients using intracranial SEEG recording. For MEG, we analyzed data in reconstructed cortical sources. SEEG sampling locations were inhomogeneous across patients, but with this large cohort, we obtained a full coverage of the neocortex (Supplementary Fig. 2 of Study I). For data in Figure 6, we only analyzed SEEG contacts located in neocortical grey matter outside of the epileptogenic zone (EZ). The EZ contacts were identified by medical

doctors during presurgical evaluation. After preprocessing, bistability and LRTCs were estimated for narrow-band filtered oscillation amplitude in the same manner as that for the model *R* time series.

Visual inspection of MEG and SEEG time series readily revealed numerous examples of bistability across brain regions and frequencies (Figure 6 A–B, Supplementary Fig. 3 of Study I). Pooled population distribution showed differences in BiS and DFA spectral profiles between SEEG and MEG (Figure 6C–E, sample number see Figure 6C). In line with prior arts (Freyer et al., 2009), the MEG BiS estimates showed a peak at 11 Hz, whereas, in SEEG, 2–30 Hz showed most prominent BiS estimates (Figure 6E). The small mean BiS in surrogate data is due to the algorithm reported the surrogate data as unimodal (Methods).

4.1.3 Clustering narrow-band bistability and LRTCs by topological similarity

To further inspect neuroanatomical features of bistability and LRTCs, we morphed narrow-band BiS and DFA estimates from 400 MEG parcels and SEEG contacts into a standard atlas of 100 parcels (Supplementary Fig 4). The morphed SEEG data include only the contacts recorded from non-epileptogenic zones (nEZ) across the neocortical areas. The mean parcel metrics (Supplementary Fig 5B of Study I) were identical to that of raw parcel and contact data (Figure 6D–E, Supplementary Fig 2 & 4 of Study I). The topological features of LRTCs and bistability were similar between neighbouring frequencies but different between slow and fast rhythms (Spearman's correlation coefficients, Figure 6 F–G). Based on these similarities (details in Supplementary Fig. 5C of Study I), we collapsed narrow-band maps into θ–α (5.4–11Hz) and γ-band (45–225 Hz) maps for further analyses (red boxes in Figure 6 F–G).

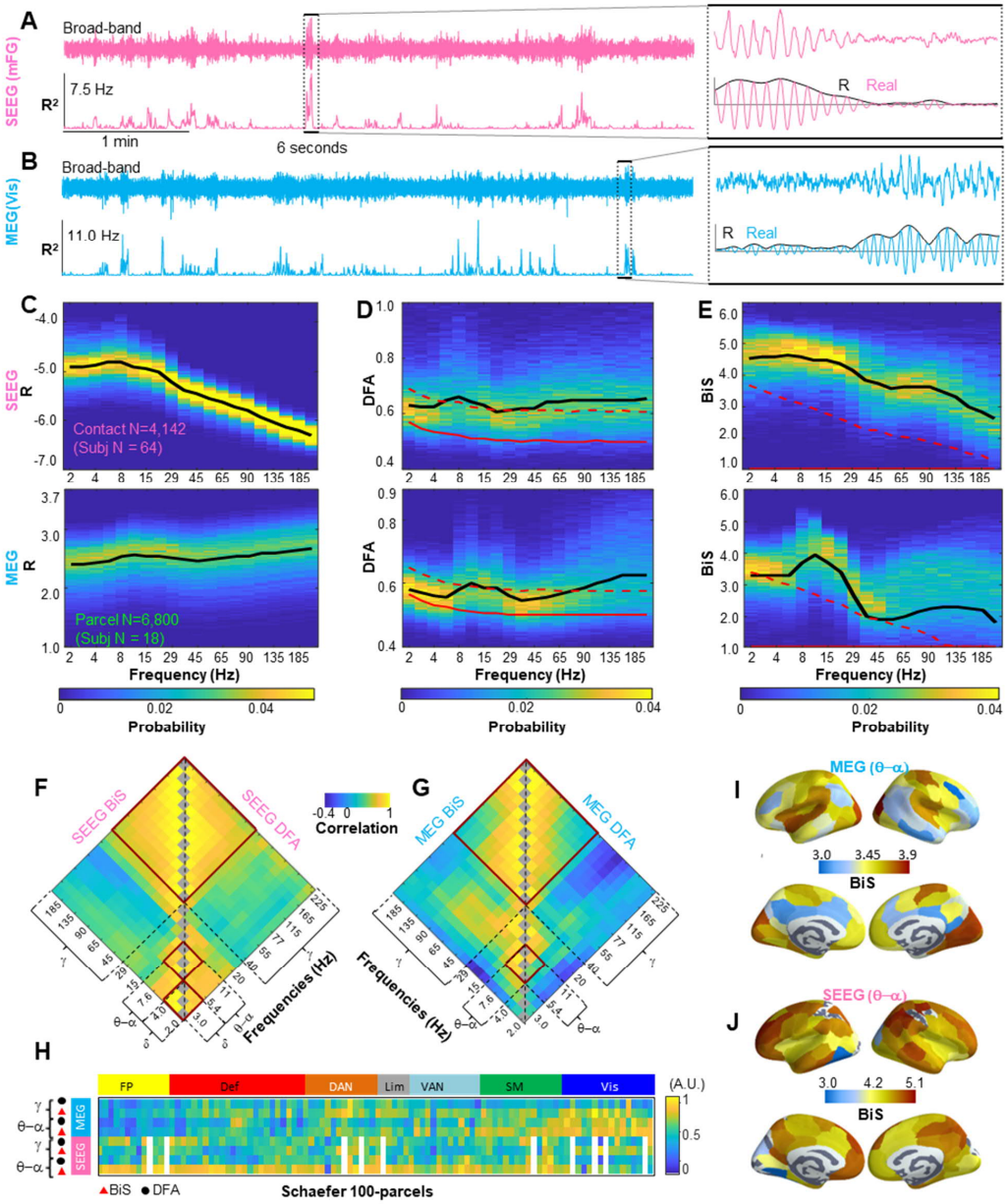

Figure 6 Bistability and LRTCs are robust, large-scale phenomena in the brain. **(A)** Five minutes of broad band and narrow band power (R^2) time series showing bistability in SEEG contact and (**B**) MEG modeled source; mFG: middle frontal gyrus; Vis: visual area. **(C–E)** Probability distribution of narrow-band amplitude (R), LRTCs estimated using DFA, and bistability estimated using BiS. Data pooled from all individual MEG parcels or SEEG contacts. Black lines indicate mean, red solid and dashed lines indicate mean and 99%-tile of surrogate observation, respectively. **(F)** Correlations between Schaefer-100-parcel narrow-band DFA and BiS estimates in SEEG and **(G)** MEG; red boxes indicate frequency clusters. **(H)** Frequency-collapsed θ–α and γ-band metrics; white-out columns in SEEG data were excluded parcels due to insufficient spatial sampling. **(I)** Cortical maps of group average α-band BiS estimates for MEG and **(J)** SEEG.

4.1.4 Topological features of bistability and LRTCs

In MEG, visual system, somato-motor, and dorsal attention systems showed prominent θ–α band bistability and LRTCs (Figure 6 H–I, statistical details see Supplementary Fig 9 of Study I). In SEEG, fronto-parietal, ventral attention, and the default networks showed pronounced θ–α band BiS, whereas the visual system showed the lowest BiS estimates (Figure 6 H & J, more details in Supplementary Figure 9 of Study I). Moreover, MEG data demonstrated high neuroanatomical similarity between bistability and LRTCs (Fig 3F & G of Study I) and in individual across functional systems (Supplementary Fig 7–8 of Study I).

4.1.5 Behaviourally relevant Bistability and LRTCs in MEG

We next inspected whether bistability and LRTCs would be behaviourally relevant. The MEG subjects took a battery of neuropsychological assessment for working memory, attention, and executive functions (Methods). We first looked for gross neuro-behavioural correlations. Within each subject, we collapse parcel BiS and DFA estimates into four gross neuronal scores, *i.e.*, θ–α LRTC, γ LRTC, θ–α BiS, and γ BiS (Supplementary Fig 10B of Study I). We next computed Spearman's correlation between subject neuronal and behavioural scores. The θ–α band BiS and DFA estimates showed negative correlation ($p < 0.05$, FDR corrected) with "zoo map time", which means that large BiS and DFA estimates predicted faster problem solving (Figure 7A, test statistics see Supplementary Fig 10C–D of Study I). We next investigated the spatial distribution of these correlations across cortical parcels as a post hoc analysis. A large fraction of the parcels showed neuro-behavioural correlations to the zoom map time ($p < 0.05$, FDR corrected; test statistics see Supplementary Fig 10E–F of Study I). Fronto-parietal, limbic, somato-sensory and visual areas show most prominent behavioural correlations (Figure 7 B–C, Supplementary Fig 10 of Study I).

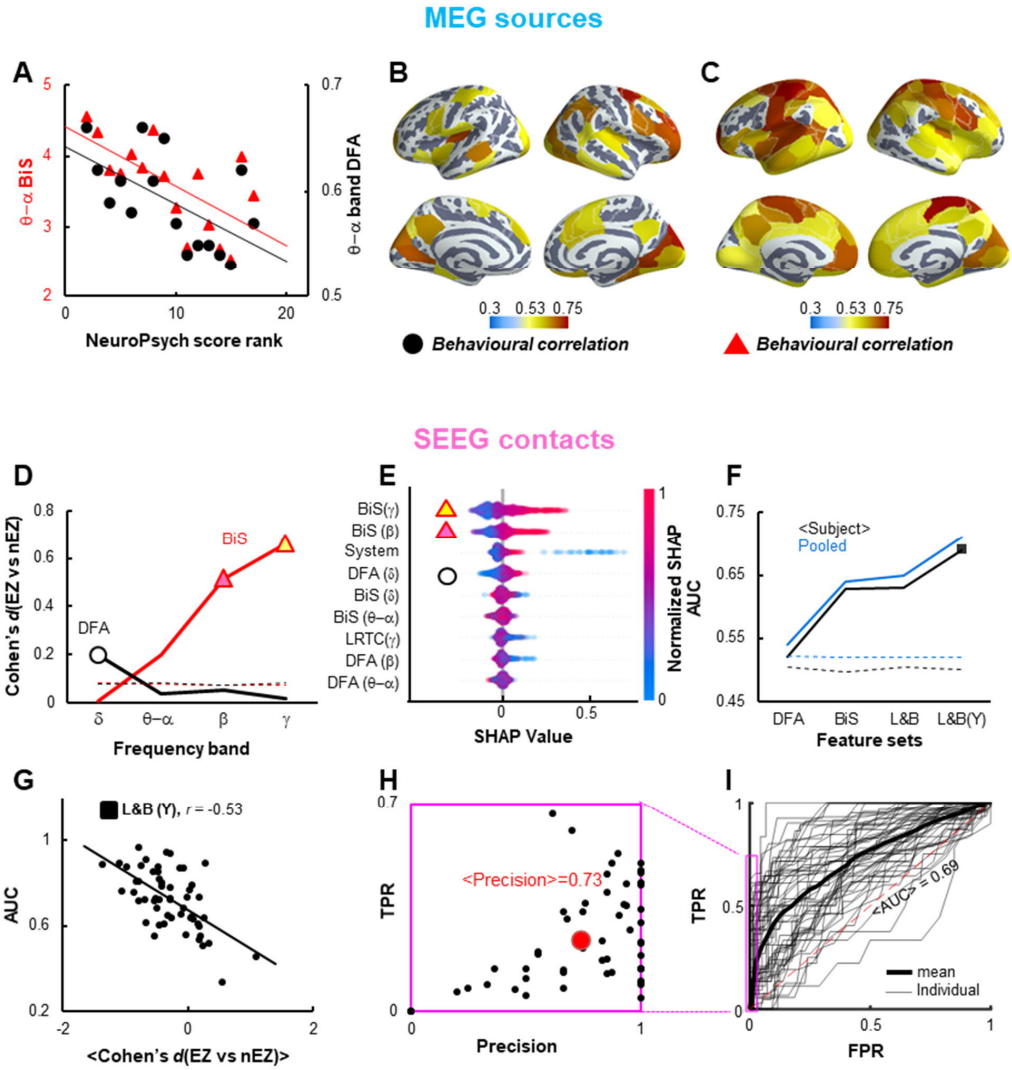

Figure 7 Behavioural correlation of bistability (BiS) and LRTCs (DFA) in MEG. **(A)** Correlations between subject Zoo Map Time Test ranks and within subject averaged-parcel θ–α band LRTCs and BiS estimates. **(B)** Cortical maps of significant correlations between subject Zoom Map Time tests and individual parcel DFA and **(C)**. **(D)** The effect size of the differences between EZ and nEZ contacts in BiS (red) and DFA (black) estimates; dashed line: 99%-tile from 1,000 label-shuffled surrogates. **(E)** Feature importance measured using the SHAP values. **(F)** The area under curve (AUC) of receiver operating characteristics derived from pooled (blue) and within individuals (black) when classifying EZ subject-by-subject using DFA or BiS alone; L&B: combining DFA and BiS; L&B(Y): L&B plus contact loci in Yeo systems. Dashed lines: 99%-tile of AUC observed from 1,000 surrogates created independently for each of the four feature sets. **(G–I)** Post-hoc inspection of results derived using L&B(Y) feature set, see black marker in (**F**). **(G)** Spearman's correlation ($p < 0.000001$, n=55) between individual AUC and within-patient mean Cohen's *d* between EZ and nEZ in band-collapsed DFA and BiS. **(H)** True positive rate as a function of within subject precision (TP ÷ predicted positives); red marker: population mean. **(I)** Receiver operating characteristics of within subject classifications.

4.1.6 Aberrant bistability characterized pathophysiology

When under the control of strong local feedback (*i.e.*, large ρ, Figure 5), our model became more sensitive to coupling κ to reach super-critical up-state. This suggests that high degree of bistability likely be a sign of catastrophic shifts to seizure-like hyper-synchronization. Therefore, we asked whether bistability and LRTCs estimated from seizure-free, inter-ictal-activity-free resting-state recording could distinguish healthy physiological signals from pathophysiology of EZ that might imply catastrophic shifts.

We first evaluated neurophysiological features that were to be used for identifying SEEG contacts located in EZ regions. Inspecting band-limited BiS and DFA estimates revealed different β and γ band BiS estimates (Cohen's $d > 0.5$) and a less prominent difference in δ band DFA between EZ and nEZ contacts Figure 7D). In addition to neuronal features, we also included the contact location in Yeo functional systems as an additional feature. To validate, we used the Shapley Additive exPlanations (SHAP) values (Breiman, 2001) to estimate the global and local feature importance for the random-forest classifier, and the results confirmed that γ and β band BiS, contact-locus, and δ band DFA were indeed the most important features for classifying EZ (Figure 7E). Thus, we ran 500 independent classification tests using the random-forest classifier, in which each test randomly chose 20% of the contacts as training set and the rest 80% as test set. The results revealed an area under the receiver operating characteristic AUC = 0.8 ± 0.002 (mean ± std) (an example see Supplementary Fig. 11C of Study I).

Last, we conducted EZ classifications for each patient. In each individual test, the contacts of the chosen patient were used as test set and the rest contacts training set. We used four incremental feature sets and evaluated the corresponding outcomes. The within individual receiver operating characteristic (ROC) analysis of the EZ classification yielded converging results as ROC analysis for population pooled classification (Figure 7F). Classification with combined BiS, DFA, and contact-locus yielded the best performance – with an AUC of 0.7 (black marker, Figure 7F). Using BiS alone yielded larger AUC than using DFA alone. Including contact-locus (L&B(Y) increased the AUC by 0.06 than combing DFA and BiS (L&B). Subject AUC values correlated with within-subject differences in DFA and BiS estimates between EZ and nEZ ($r=-0.53$, $p < 0.000001$) (Figure 7G), and was not affected by subjects' total contact number, EZ contact number, or the ratio between EZ and nEZ contacts (r= -0.06, -0.07 and -0.09, respectively). Last, despite the variability in individual ROC curves, the classifier on average yielded a precision of 0.73 and mean false-positive rate of 0.03 (Figure 7H–I).

4.2 Study II: Large-scale synchrony between cortical high-frequency oscillation (HFO)

Inter-areal synchrony between cortical oscillations at frequencies below ~100 Hz is a ubiquitous phenomenon and is thought to coordinate communications between ensembles in cortical networks. Broad band activities and oscillations faster than ~100 Hz have been considered as local-circuit-level phenomena and impossible to synchronize over long distance. We discover that, however, in the resting human brain, high-frequency oscillations (HFOs, 100–400 Hz) recorded with intracerebral Stero-EEG (SEEG) are synchronized between widely distributed cortical areas. After batteries of rigorous control analyses, we validated that the observed HFO synchrony was not due to technical or physiological artefacts. We also investigated the neurophysiological attributes and behavioural relevance of the large-scale HFO synchrony.

4.2.1 Probing large-scale resting-state brain connectivity with SEEG recording

We recorded 10 minutes of resting-state intra-cerebral local-field potential (LFP) signals from 92 patients using SEEG. Due to previous brain surgery or preexisting cortical malformations (Table 1 of Study II), 25 patients are excluded from analyses. After excluding contacts located in epileptic zone (EZ), this 67-subject cohort contains

a total of 7,068 contacts located in neocortical grey matter (mean ± std: 113 ± 16.2, range: 70–152), which, on the population level, offered a dense coverage across brain regions and functional systems (Schaefer et al., 2017; Yeo et al., 2011) (Fig 1 and Supplementary Figure 1 of Study II). We estimated phase synchrony between contact pairs located in neocortical grey-matter outside of the EZ (nEZ) and those that did not shared same reference channel, which yielded a total of 368,043 contact pairs (mean ± std: 5,500 ± 1,600, range: 2,094–9,947). Amalgamating the individual connectivity of this cohort offered 80% and 90% coverage of the left- and right-hemispheric connectome in the Schaefer 100-parcel atlas and a full coverage of the seven functional systems with abundant sampling. This dataset thus can offer a comprehensive description of large-scale cortical connectivity.

4.2.2 Cortical HFOs exhibited large-scale phase synchrony

Visual inspection of contact traces revealed short bursts of significant HFO coupling over several centimeters in the cortex, in which transient narrow-band HFO synchrony was observed in specific phases of low frequency amplitude fluctuations visible in the broad-band signals (Figure 8A–B). For the main analyses, we re-reference (cWM) every grey-matter contact to its nearest contact in the white matter (Arnulfo et al., 2015), which offers better performance in controlling for signal mixing effects and obtaining polarity-correct LFP recordings, *e.g.*, as comparing to bipolar referencing (Study II Supplementary). We computed phase-locking value (PLV) across frequencies (2–450Hz) and between all contacts and then averaged within subjects in quartiles of inter-contact distances (each quartile contains 92,011 contact pairs). We found that, across all spatial ranges, PLV increased from 2 to 7 Hz then decayed from 10 to 100 Hz. However, in the HFO frequencies (100–450 Hz), inter-areal synchrony exhibited two peaks at 150–210 Hz and 300–400 Hz (Figure 8C, test statistics see Supplementary Fig 1g of Study II). Importantly, as a corroborating evidence, we also observed HFO synchrony in a publicly available resting-state electrocorticography (ECoG) dataset (Supplementary Figure 2 j-m of Study II).

4.2.3 Control analyses for validating the HFO synchrony

Given the novelty of observing large-scale cortical HFO synchrony, we conducted a series of rigorous control analyses to exclude the possibilities that this finding is false positive due to technical or physiological artefacts. First, although highly localized SEEG signals are known to be largely unaffected by volume conduction, we estimated synchrony again with the imaginary part of the complex-valued PLV (iPLV) to verify that the PLV estimates of observed HFO synchrony was not falsely inflated due to residual volume conduction (the theory detailed in Study III). The spectral pattern of iPLV estimates was the same as PLV (Figure 8D). As one more extra control for volume conduction, we estimate PLV and iPLV between bipolar-referenced contacts, which again showed strong evidence of HFO synchrony (Figure 8E, Supplementary Figure 1g of Study II). Moreover, the HFO synchrony was also reliably observed from randomly split cohorts of matching anatomical sampling, which indicated that the HFO synchrony is preserved with only a half of the current cohort size (Supplementary Figure 2 a & b of Study II). Although observations with iPLV and bipolar data confirm that the PLV estimates of synchrony over “very short” distance (0–32 mm) was real, the PLV estimates in this range could have been inflated by residual volume conduction (Study III). Therefore, we exclude the “very short” contact pair from further analysis.

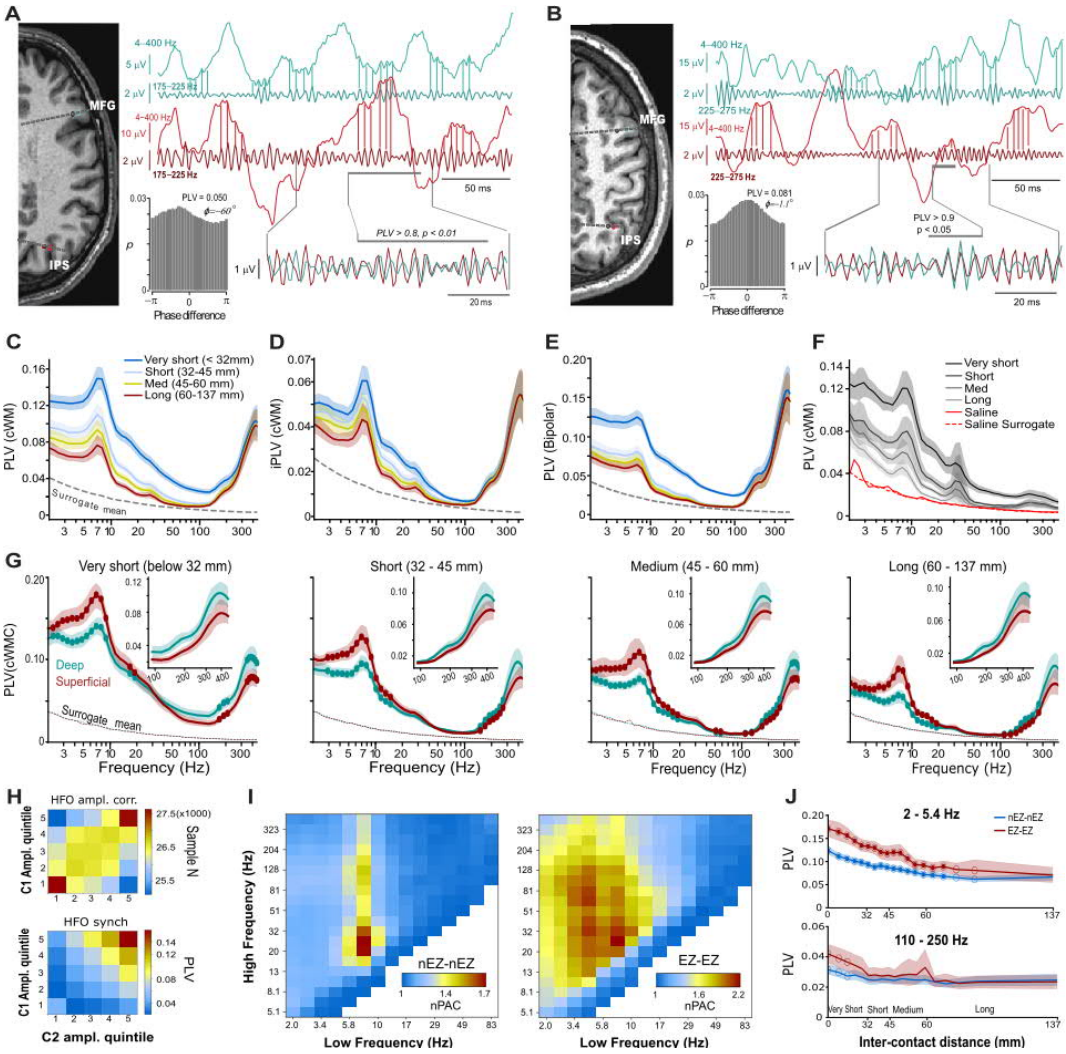

Figure 8 Large-scale synchrony between cortical high frequency oscillations (HFO). **(A)** Examples of long-range HFO synchrony with non-zero and **(B)** near-zero phase lag. **(C)** Population-level synchrony measured with PLV, **(D)** iPLV using closest white matter (cWM) and **(E)** bipolar referenced data across distance. **(F)** PLV between contacts in saline solution (red), **(C)** was used as reference (grey). In **(C–F),** dashed lines: 99.9%-tile of surrogate confidence intervals (CI) (N_{rand} = 100); Shades: 2.5–97.5%-tile bootstrap CI ($N_{bootstraps}$ = 100). **(G)** PLV between contacts from deep (teal) and superficial (red) cortical layers; Deep: -0.3 < GMPI ≤ 0; Superficial: 0.5 < GMPI < 1. GMPI: gray mater proximity index. The markers indicate differences (two-tailed permutation test, N_{perm} = 100, $p < 0.05$, FDR corrected). Dashed lines: 99.9%-tile of surrogate CI (N_{rand} = 100). Shades: 2.5–97.5%-tile of bootstrap CI ($N_{bootstraps}$ = 100). **(H)** Top: histogram of the HFO amplitude coincidences for all pairs (C1, C2) of contacts; bottom: moment-to-moment dependency of HFO synchrony on HFO amplitude between contacts. Each element is the mean of instantaneous PLV between all significant contact pairs as a function of their moment-to-moment normalized amplitudes. **(I)** Phase-amplitude coupling (PAC) of nEZ networks (left) and EZ networks (right); nPAC = $PAC_{observed}/PAC_{surrogate}$. **(J)** PLV between EZ (red) and between nEZ (blue) contact across distances (20 bins) for δ- and HFO band. Shade: 5% and 95 %-tile of bootstrap CI ($N_{bootstraps}=10^4$), markers: significant differences ($p < 0.05$, one-tailed randomization test), solid makers: differences after FDR correction. Figures adapted by permission from (Arnulfo et al., 2020); Creative Commons CC BY license.

We conduct more tests to assure that environmental or amplifier noise correlations could not have confounded the HFO synchrony. First, we acquired 10 minutes of recording with two SEEG electrode shafts (18 contacts each) fully immersed in saline solution. We analyzed the saline solution recording as bipolar-referenced data and found no evidence of synchrony either below 100 Hz or in the high-gamma frequencies (red line, Figure 8F). To control for other possible confounders beyond volume conduction and amplifier noise, we inspected whether HFO synchrony could be attributable to *i*) epileptiform neuronal activity, such as inter-ictal spikes (Study II Supplementary Figure 3d), *ii*) muscular signals (Study II Supplementary Figure 3b), *iii*) leakage of line noise or notch-filter artefacts (Study II Supplementary Figure 4), and *iv*) effects of filtering near the Nyquist frequency (Study II Supplementary Figure 5). The results converge to a conclusion that HFO synchrony was only explainable by true phase coupling between HFO signals from distinct neuronal ensembles.

4.2.4 Distinct laminae profiles of HFO synchrony

Below ~100 Hz, neuronal oscillations from deep and superficial laminae engage differently in long-range phase synchrony (Arnulfo et al., 2015). We next investigate whether HFO synchrony was functionally dissociable from the laminar differentiation of slower cortical rhythms. We categorized cWM-referenced SEEG contacts into "deep" or "superficial" by normalized depth of contact location in the grey matter using the Grey Matter Proximity Index (GMPI) (Arnulfo et al., 2015). We next averaged PLV and iPLV across spatial distance for deep and superficial contact pairs. From 3 to 20 Hz, superficial contact pairs exhibited stronger synchrony than deep contact pairs across all spatial range (Figure 8G), which was in line with previous finding of laminar localization of current sources underlying theta and alpha oscillations in macaques monkeys (Bastos et al., 2015) and humans (Arnulfo et al., 2015; Halgren et al., 2018a). However, in the HFO bands, deep contact pairs across all spatial range showed stronger and more prevalent synchrony ($p < 0.05$, FDR corrected, statistics detailed in Study II Supplementary Figure 7). The distinct laminar profile of slower and HFO synchrony was split-cohort reliable (Study II Supplementary Figure 2e–f) and evident also in bipolar-referenced data estimated using PLV and iPLV (Study II Fig. 5b and Supplementary Figure 7 b). Importantly, in bipolar-referenced data, abolished laminar difference in low frequencies concurs with enhanced laminar HFO synchrony difference and HFO PLV strength, which suggested that the HFO signals originated from highly local cell assemblies in the peri-electrode volume whereas the low frequency signals reflect larger assemblies with greater volume conduction. These results thus indicated that long-range synchronized HFO signals originate from current sources that are distinct, or at least partially, from those that underlies slower cortical oscillations.

4.2.5 Strong HFO phase synchrony associated with high-amplitude HFO

We next assessed the neurophysiological attributes of long-range HFO phase synchrony. Both high-gamma activity (HGA) and band-limited HFO amplitudes reflect the coherence of local neuronal MUA or the post-synaptic potentials (Ray et al., 2008) from at least a few hundreds of neurons in the immediate vicinity of the recording site up to ~50k neurons within a range of ~100 μm. Temporally aligned spiking activity is crucial for an ensemble to effectively signal its post-synaptic target ensembles, and therefore moments of strengthened HFO synchrony between two ensembles should be exclusively associated with high HFO amplitude in both ensembles.

To test this hypothesis, we picked SEEG contact pairs that exhibit significant HFO phase synchrony ($p < 10^{-3}$). For each contact pair, we deposited samples of HFO time series from two contacts (C1 & C2, Figure 8H) into a 2D matrix representing the joint distribution of HFO amplitude quintiles from the contact pair. The resulting population mean pooled across electrode pairs, subjects, and frequencies showed a slight positive correlation

between the pair of amplitudes. This meant that the probability of samples from both contacts being in the largest quintile or smallest quintile is ~8% (*i.e.*, 27.5÷25.5 – 1) more prevalent than one in the smallest quintiles and the other in the largest quintile (top, Figure 8H). This amplitude covariance indicated overall weak HFO amplitude correlations that deviates 1–5% from the null hypothesis level in HFO frequencies (detailed in Study II Fig. 6b).

Furthermore, strong HFO phase synchrony only occurred when both recording sites were in high HFO amplitude state. The mean phase synchrony was the highest when the amplitudes are in the largest quintile at both contacts whereas much weaker when the amplitude of either of the contacts is low (bottom, Figure 8H), which constituted a large difference of ~500 % (*i.e.*, 0.15÷0.03) comparing to ~8% of the difference in amplitude correlations (top, Figure 8H). To rule out the possibility that changes in the signal-to-noise ratio (SNR) could have confounded these results, we used recordings from saline solution to estimate the apparent SNR and compare with earlier study on how SNR influences PLV estimates. Given the SNR range of HFOs in our data (4–10), the mean PLV (~0.06) may be inflated by ~10 % due to any amplitude increase (Study II Supplementary and Fig. 3), which is an order smaller than what we have observed here. To summarize, these findings of HFO synchrony were robust and showed that high amplitude local HFO, as an indicator of high local HFO coherence (Ray et al., 2008), is a concurring network phenomenon of long-range HFO phase synchrony.

4.2.6 HFO synchrony differentiate not EZ and nEZ networks

We next addressed whether HFO synchrony could be a feature of putatively healthy brain activity or a byproduct of epileptic pathophysiology. Epilepsy is known to affect δ-band dynamics (Englot et al., 2010; Lundstrom et al., 2019). Enhanced fast oscillations often take place in specific phases of slow oscillations that are above 1Hz but below low γ-band (Nonoda et al., 2016; Scheffer-Teixeira et al., 2013) or slower rhythms below 1 Hz (Monto et al., 2008; Vanhatalo et al., 2004). We aimed to dissociate healthy from pathological cross-frequency phase-amplitude coupling (PAC). Hence, we computed all-to-all inter-contact PAC in all subjects and across frequencies for both EZ loci and putatively healthy non-EZ loci (nEZ). Between nEZ contact pairs, β- and low γ-band (20–40 Hz) oscillation amplitudes strongly coupled with the phase of θ- to α-band oscillations (5–10 Hz) with a peak at 8 Hz (Left, Figure 8I). The HFO amplitudes of 100-200 Hz also coupled with the phase of 5–10 Hz oscillations between nEZ contacts. Between EZ contact pairs, PAC intensity was stronger than that of nEZ contacts (right, Figure 8I). Between EZ contacts, PAC exhibit much broader slow-frequency and high-frequency coverage. Notably, in addition to the ~8 Hz low-frequency peak seen also in nEZ contacts, a strong effect of δ-band (1–4 Hz) low-frequency phase coupled with 100–300 Hz amplitudes. These putatively pathological δ-band PAC components were also evident in PAC between EZ and nEZ contact pairs (Study II Fig. 7c).

We further inspected whether HFO synchrony could be a characteristic of healthy brain activity or epileptic pathophysiology. We compared the HFO synchrony strength between EZ-EZ contact pairs and between nEZ-nEZ contact pairs. After controlling for inter-contact spatial distance, the EZ-EZ contact pairs exhibit stronger phase synchrony than nEZ-nEZ contact pairs only in frequencies below 100 Hz most pronounced in the δ-band across short to medium spatial distance (top, Figure 8J). Importantly, EZ-EZ and nEZ-nEZ networks did not show different HFO synchrony strength across all distances ($p > 0.05$, corrected for FDR, details in Study II Fig. 7). Moreover, HFO phase synchrony strengths did not correlate with inter-ictal spikes which would constitutes a proxy for the severity of epileptic pathology otherwise (Study II Supplementary Figure 3 d). Taken together, the δ-band network phase synchrony might have been compromised by pathophysiology, but the HFO synchrony was a predominant attribute of tentative healthy brain dynamics.

4.2.7 Neuroanatomical features of HFO connectome are far from random graphs

We aim to investigate the neuroanatomical characteristics of the population-level HFO connectome. To first screen for outliers and inspect individual variability, we compute the all-to-all similarity between subject HFO PLV spectra for which we exclude EZ contacts and the "very short" distance contact pairs (Figure 9A). Hierarchical clustering with optimal cost function yielded five subject clusters (Study II, Fig. 3b–c). The subjects belong to the first and second cluster exhibited two peaks at 150–210 Hz and 210–300 Hz (Figure 9 B–C), and these peaks were also evident in iPLV spectra and bipolar-referenced data (Study II, Fig. 3). The third and fourth cluster included thirteen subjects who were characterized by a peak in synchrony spectra at 300–400 Hz but lack the 150-300 Hz peaks. The fifth cluster included three subjects who exhibited a ramp in the synchrony spectra near the Nyquist limit of 500 Hz and were excluded from further analysis because the 1 kHz sampling rate is inadequate for estimating synchrony at range (Study II Supplementary Figure 5). The presence of individual variability in peaks refuted the possibility that the long-range HFO synchrony relates to broadband HGA.

We next morphed narrow-band individual inter-contact PLV from the first and second cluster subjects (n = 51, see Study II Supplementary Methods) into group-level connectomes, *i.e.*, all-to-all connectivity between 100 Schaefer parcels. Because the interhemispheric connectivity was insufficiently sampled, we inspected left and right hemispheres separately (Study II Fig. 1c). The topological similarity matrices did not show widespread correlations between all HFO frequencies but demonstrated three frequency clusters as 150–210 Hz, 210–300 Hz, and 300–400 Hz (Figure 9E) refuting that HFO synchrony was due to broad-band MUA-like HGA signals. Taken together, the PLV connectome similarity, network node strengths similarity (Study II Supplementary Figure 6 a–c), and the individual PLV spectra (Figure 8 B–D) shared the same frequency clusters, which supports that HFO synchrony is a network-level emergent phenomenon in distinct frequency bands.

We next inspected the topological features of the HFO connectomes. First, both hemispheres exhibited modular structures with significant modularity z-scores throughout HFO frequencies and a prominent peak in 150–210Hz range (see Study II Fig. 4b, Supplementary Figure 6 d). Partitioning left and right hemisphere 150–210Hz synchrony similarity across clustering resolution reveals 2 to 11 and 2 to 7 modules, respectively (Figure 9F). At mid-range resolution (γ = 1.25) both hemispheres showed five modules (Figure 9G), among which two large modules were similar across hemispheres and corresponding to a posterior and a fronto-central constellation (blue/light blue and yellow/orange, respectively, Figure 9H). Thus, the HFO connectome had a coarse bilaterally symmetric community structure similar to the anterior-posterior gradient observed in structural and functional networks and grey matter thickness (Paquola et al., 2019). At coarse spatial resolution, the 150–210Hz between-system connectivity was inhomogeneous and most pronounced within the limbic and between the limbic and other systems (details and statistics in Study II Fig. 4c & Supplementary Figure 2g-i and split-cohort reliability see Supplementary Figure 2 c, d). To summarize, the population-level HFO synchrony connectome showed robust modular structures that were not influenced by individual variability in synchrony spectra, individual pathogenesis, or electrode placements.

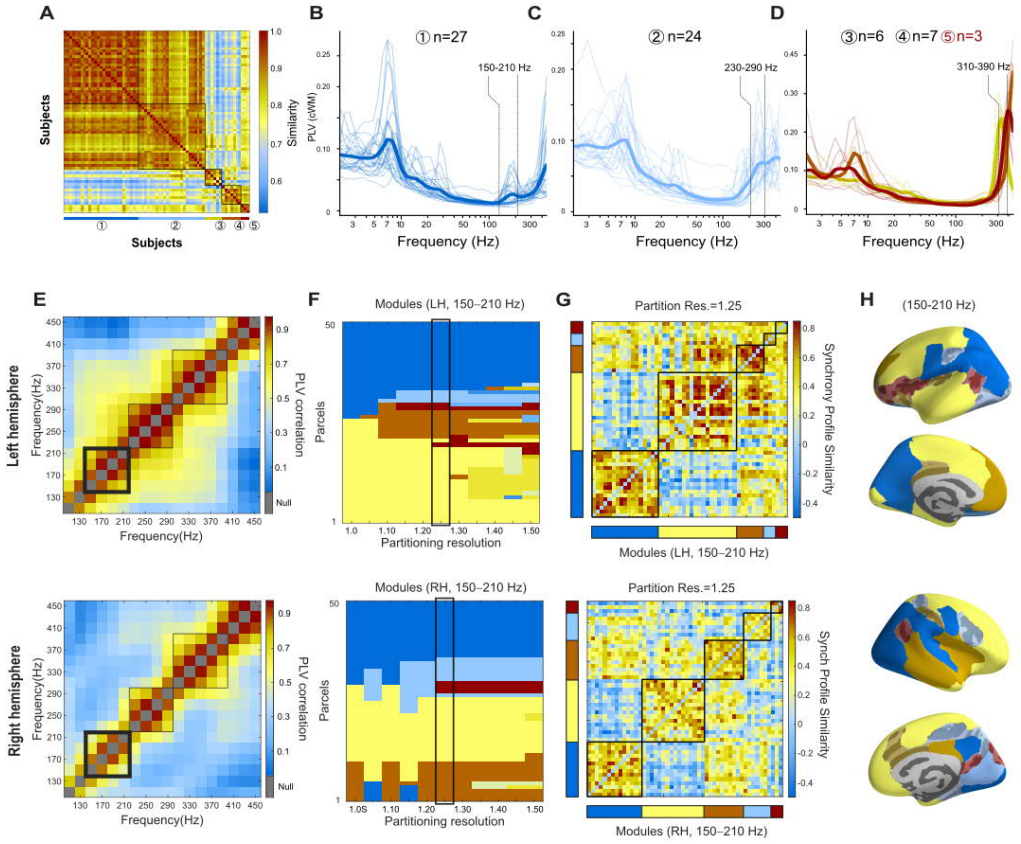

Figure 9 Neuroanatomical localizations and communities of HFO connectomes. **(A)** Between-subject HFO synchrony (PLV) similarity matrix shows five subject clusters. **(B–D)** Individual and mean synchrony spectral profiles of the subject clusters defined in **(A)**. Individual connectomes of cluster (1) and (2) were morphed into group HFO connectome for community detection. **(E)** Similarity between group-level HFO connectomes for left and right hemispheres (top and bottom row, respectively) in the Schaefer 100-parcel atlas. **(F)** Community assignments to parcels as a function of the resolution (γ) of the Leiden algorithm. **(G)** Communities at resolution $\gamma = 1.25$ as marked in **(F)**. **(H)** Visualization of communities defined in **(G)**. Parcels with stable community assignment are rendered opaque; assignments to 22% left and 14% right hemispheric parcels were unstable and rendered as semi-transparent (one-tail test, $p > 0.05$, parcel module-allocation stability, Study II Supplementary). Figures adapted by permission from (Arnulfo et al., 2020); Creative Commons CC BY license.

4.2.8 Transiently increased HFO synchrony during tasks

Last, to investigate whether HFO synchrony would show task-specific modulations, *i.e.*, potential functional relevance, we inspected time-resolved HFO synchrony when patients perform a visuomotor Go/No-Go task. A subset (N=11) of the patients participated this experiment, during which they were asked to respond with a button press to “Go” cues and withheld responses to less frequent “NoGo” cues (a ratio of 1/3). This type of response inhibition is known to induce large-scale frontoparietal brain activation, and therefore, we first examined peri-stimulus amplitude dynamics from local HFOs for the localization of task-relevant brain regions (Buzsáki and Silva, 2012; Jones et al., 2000; Khodagholy et al., 2017; Logothetis et al., 2012; Nitzan et al., 2020; Novitskaya et al., 2016; Vaz et al., 2019). From 150 to 350 ms after cue onset, the mean HFO amplitude

increased two SDs above the baseline in 4–11% grey matter contacts in nine subjects (range: 103–139, an example subject see Figure 8a). Two subjects showed no HFO amplitude responses and hence were excluded from analyses.

We next examined time-resolved HFO synchrony between the top 5% contacts that exhibited greatest task-induced HFO amplitude dynamics (Task+ in top-right, Figure10A). In individual subjects, time-resolved HFO synchronization and desynchronization relative to baseline formed clusters in time-frequency domain (see Figure 10B for the same subject shown in 10A) which could be identified with cluster permutation (Figure 10C). Pooling three largest clusters across subjects revealed a population-level prevalence (*K*) of transient increase in wideband HFO synchrony near 200 ms post-cue and sustained narrow-band synchrony in the range of 110–150 and 300–400 Hz (left, Figure 8d). Moreover, the HFO synchrony clusters concurred with a population-level 150–250 Hz desynchronization most prominent during 200-600 ms post-cue (right, Figure 10D).

Finally, we performed additional tests to validate that observed time-frequency clusters of HFO synchrony (Figure 10D) were robust against threshold of ΔPLV, the spatial extent of sampled brain areas, and subject prevalence (*K*). First, we tallied the size of the three largest clusters with increasingly strict ΔPLV threshold. As ΔPLV threshold became stricter, total clusters area decreased, but all subjects showed cluster sizes larger than the 95%-tile of surrogate observation (Figure 10E). Next, to inspect how widespread the brain areas (in terms of contact number) where the time-frequency clusters of HFO synchrony were observable, we computed the difference of areas between observed and surrogate clusters with increasingly larger networks by gradually adding contacts for the positive and negative clusters. The greatest area difference was seen when below 10% of all contacts were involved (Figure 10F), converging with the amount of task+ contacts seen in HFO amplitude dynamics (see Figure 10A). To validate that the transient HFO synchrony (Figure 10D) was localized to task-relevant brain areas, we evaluated the observed-vs-surrogate area difference for every 5% of contacts along the Task+ … Task– axis (see top-right, Figure 10A). Significant cluster area difference was observed for positive HFO synchrony in the first two 5%-bins (Figure 10G), which confirmed that HFO synchrony was limited to task-relevant areas and was not artificially inflated by the analysis procedure. Among nine subjects, seven (*K*=0.78) and four (K=0.44) subjects exhibited significant positive effect in the first two 5%-bins, respectively.

To summarize, HFO synchrony was transiently strengthened during task-relevant neuronal processing specifically in the task-positive cortical areas. We suggest that HFO synchrony in the sampled circuits reflect the neuronal communications underlying large-scale coordination of visuo-motor processing in this Go/NoGo task.

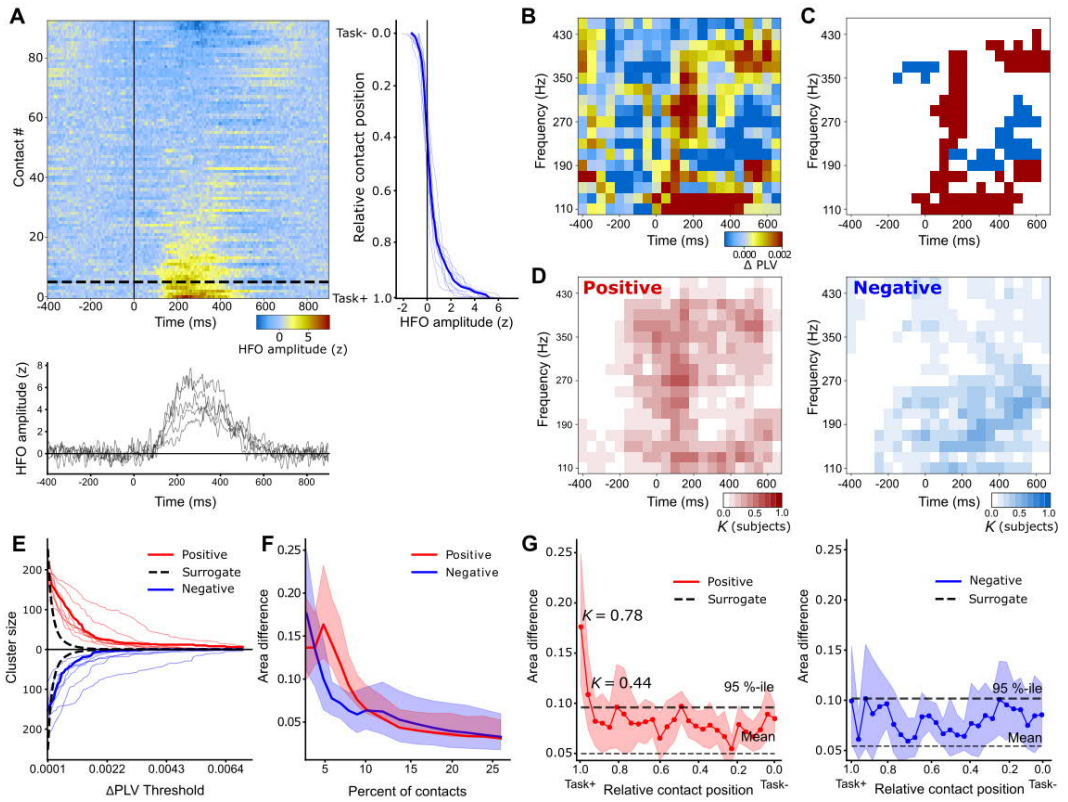

Figure 10 Transiently enhanced HFO synch between task-relevant areas. **(A)** Top-left: increased HFO amplitude in a subset of contacts in one exemplary subject following stimulus onset. Contacts were sorted by (150–350 ms) amplitude, averaged across 110–430 Hz, z-score normalized by pre-stimulus baseline 500–10 ms. Top-right: mean (thick) and individual HFO responses in 150–350 ms post-stimulus period. Bottom: individual subjects' temporal evolution of HFO responses averaged for the top 5% of SEEG contacts. **(B)** Change in PLV from baseline levels among the top 5 % of electrode contacts from the same subject shown in **(A)**. **(C)** Three largest positive (red) and negative (blue) time-frequency clusters for the representative subject (threshold for PLV change: 0.001). **(D)** Superposition of three largest task positive and negative clusters of all subjects, where *K* is the fraction of subjects with a cluster contributing to each time-frequency element. **(E)** Sum of the time-frequency elements in the three largest clusters as a function of the clustering threshold for the positive and negative clusters (thick lines: group mean; thin lines: individual; black dashed lines: 95%-tile of the cluster sizes observed from surrogate data). **(F)** Difference of total cluster-size areas (area under curves in **(E)** from threshold of 0 to inf) from threshold between the data and surrogate mean for varying fractions of contacts used in synchrony estimation (averaged across subjects, shaded areas indicate bootstrapped 5 and 95 %-ile confidence limits of the means). **(G)** Cluster-size areas (data minus surrogate as in **(F)**) for synchronization evaluated in 5 % contact sets along the Task+ … Task- axis defined by sorted HFO amplitudes (black lines indicate the 95%-ile (thick line) and mean (thin line) of surrogate data. Figures adapted by permission from (Arnulfo et al., 2020); Creative Commons CC BY license.

4.3 Study III: signal linear mixing in MEG/EEG results in ghost interactions

To date, MEG and EEG are the only non-invasive electrophysiological tools for studying large-scale cortical interactions. Unlike highly localized intracranial SEEG recording, estimating source connectivity with MEG/EEG is hindered by signal linear mixing. Mixing among MEG/EEG sources introduces false positive

correlations, biases to estimates, poor separability of true sources, and misrepresented topological features of functional connectivity (FC). Mixing directly results in inflated correlational estimates and artificial interaction (AI) when using mixing-sensitive metrics such as phase-locking value (PLV) or amplitude correlations (CC).

Several phase- and amplitude-correlation metrics, such as the imaginary part of the complex PLV (iPLV) or orthogonalized amplitude correlation (oCC) have been proposed to correct AIs and thus have become increasingly popular in FC studies. Although these AI-free metrics are indeed immune to the zero-lag AIs, they do report a multitude of false positive ghost interactions (SI) due to the signal mixing in the vicinity of a true pairwise interaction (1.3, Figure 2). Here, we defined the AIs and SIs and demonstrated how signal mixing, the strength of phase or amplitude coupling, and phase different may affect pairwise synchrony estimates in different manners. We used the most popular PLV and iPLV as phase metrics, and CC and oCC as amplitude metrics. However, signal linear mixing effects persist irrespective of the specific metrics or source model. The ghost SIs problem affects region-of-interest analyses and significantly limits the separability of true cortical interactions, which in turn confounds the overall interpretability the FC connectomes. The ghost SIs must be carefully considered in FC analyses with MEG/EEG.

4.3.1 Mixing biases the estimates of phase synchrony

Mixing biases individual PLV estimates of phase synchrony between two signals (1.3.3, Figure 2). To illustrate this, we first we simulated two signals with a phase coupling (C_Θ) of 0.4 and a lag of 0.3 π in the absence of signal mixing (m=0) (Methods) (Figure 11A). The observed phase difference distribution across samples peaked at the simulated phase lag of -0.3 π (green, Figure 11C). Next, we introduced mixing (m = 0.4) into the two signals while kept the same coupling and lag (Figure 11B). Observed phase difference distribution became narrower (i.e., larger PLV) and the peak of the distribution shifts towards zero (magenta, Figure 11C). Thus, mixing inflates the PLV value, biases the phase lag of the estimated synchrony, and diminishes the iPLV estimate due to the biased lag towards zero-degree (Figure 11D).

4.3.2 Mixing biases the estimates of amplitude coupling

Signals mixing biases amplitude metrics in the same manner as it does to PLV and iPLV. First, we simulated two amplitude-coupled signals (C_A=0.4) in the absence of mixing (m=0) (Fig 11E). The CC is the correlation coefficient between the samples of two amplitude envelopes and characterizes the instantaneous coupling over time – thus an equivalent of PLV in amplitude domain (left, Figure 11G). The oCC first orthogonalizes the two signals by linearly removing the instantaneous component of one signal from the other, and then computes the CC between the orthogonalized signals (right, Figure 11G). Introducing mixing (m=0.4) (Figure 11F) significantly increased the similarity between the samples from two amplitude envelopes, which artificially inflated the estimates of both CC and oCC (Figure 11H). Note that mixing artificially inflates oCC but dampens iPLV. In the absence of true amplitude coupling, the mixing of signals from one source into its neighbouring sources results in numerous artificial CC but not oCC interactions between the source and neighbouring sources (Study III, Fig 2), which was virtually identical to what was observed with PLV and iPLV (Figure 2 B–C). Likewise, when a long-range a true amplitude correlation is present, mixing, in addition to generating artificial CC interactions, results in ghost SIs in both CC and oCC graphs in the vicinity of the true interaction as what was observed in PLV and iPLV (Figure 2 D–F). Therefore, mixing biases CC and oCC measure of amplitude coupling nearly in the same manner as it does to PLV and iPLV, respectively.

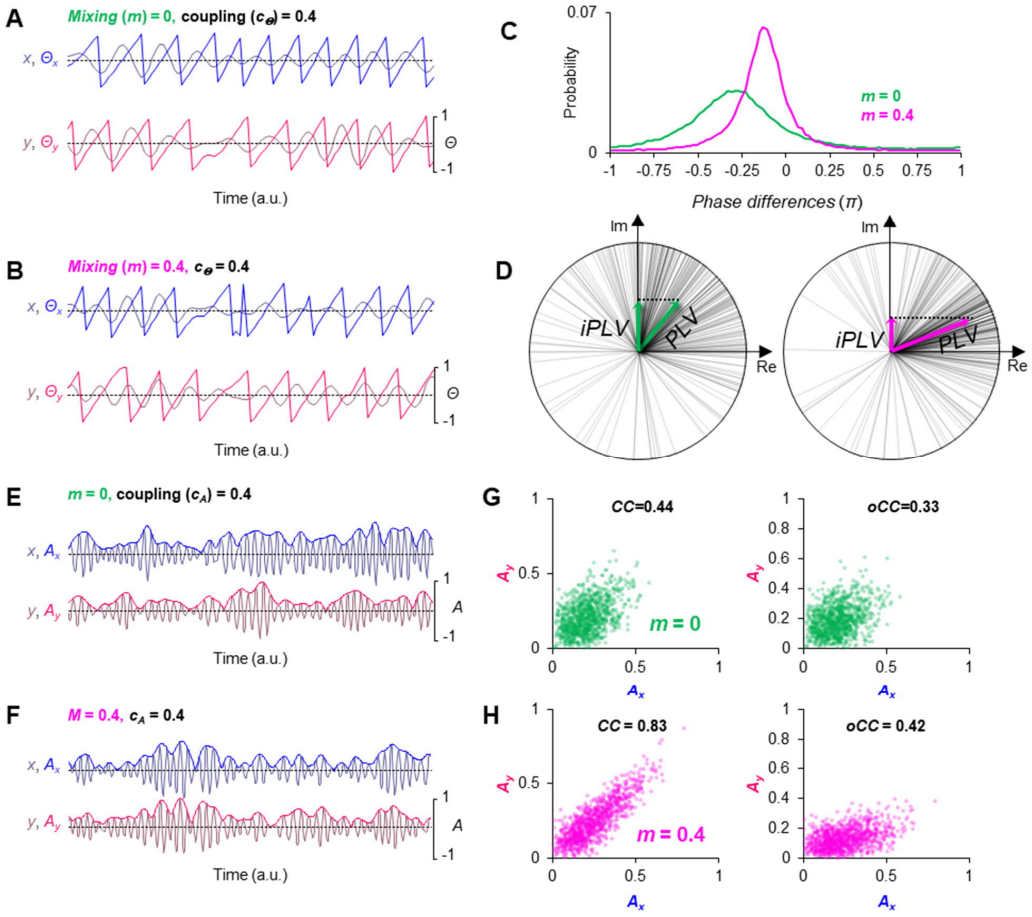

Figure 11 Mixing bias to phase and amplitude coupling estimates. **(A–B)** Coupled ($c_\Theta = 0.4$) real-valued signals $x(t)$ and $y(t)$ and their phase times series $\Theta_x(t)$ and $\Theta_y(t)$ in **(A)** the absence and **(B)** presence of linear mixing. **(C)** Distribution of Phase difference between $\Theta_x(t)$ and $\Theta_y(t)$ with and without mixing (magenta and green, respectively). The true phase difference (φ_{xy}) = –0.3π. **(D)** The same phase distribution of **(C)** in complex plan. Left: m=0; right: m = 0.4. Mixing biases phase difference distribution towards ϕ_{xy} = 0, and therefore inflates PLV while decreases iPLV. **(E–F)** Coupled (c_A = 0.4) real-valued signals $x(t)$ and $y(t)$ and corresponding amplitude envelopes $A_x(t)$ and $A_y(t)$ in **(E)** the absence (m = 0) and **(F)** presence (m = 0.4) of mixing. **(G–H)** Temporally aligned $A_x(t)$ and $A_y(t)$ values (each dot represents a sample) in the **(G)** presence and absence **(H)** of mixing for estimating CC and oCC using $A_x(t)$ and $A_x(t)$ orthogonalized $Ay(t)$ values. Figures adapted with permission from (Palva et al., 2018); Creative Commons license(CC BY-NC-ND 4.0).

4.3.3 Mixing, phase coupling strength, and lag affect PLV and iPLV differently

To assess the behaviours of PLV and iPLV in measuring phase synchrony, we systematically manipulated three parameters: phase coupling strengths ($C_\Theta = 0 \ldots 1$), phase lag ($\phi_{xy} = -\pi \ldots \pi$), and linear mixing ($m = 0 \ldots 0.6$) between two simulated signals $x(t)$ and $y(t)$. For each realization of the $x(t)$ and $y(t)$ time series, we estimated the phase coupling with both PLV and iPLV. When there is a constant phase lag of 0.3π between $x(t)$ and $y(t)$, both PLV and iPLV estimates monotonically increased as phase coupling increased (Figure 12 A & B). Linear mixing inflated PLV estimates, and this bias was strongest when phase coupling was small (coloured lines,

Figure 12A). Moreover, this positive bias to PLV saturated at higher values of true coupling because by definition PLV is bounded to a maximum value of one. On the other hand, mixing dampened iPLV estimates because mixing shifts the phase difference distribution towards zero degree (Figure 11 C & D) and iPLV is the projection of the complex number on the imaginary axis. Contrary to PLV, the dampening effect of mixing to iPLV was the strongest when phase coupling was high (coloured lines, Figure 12B).

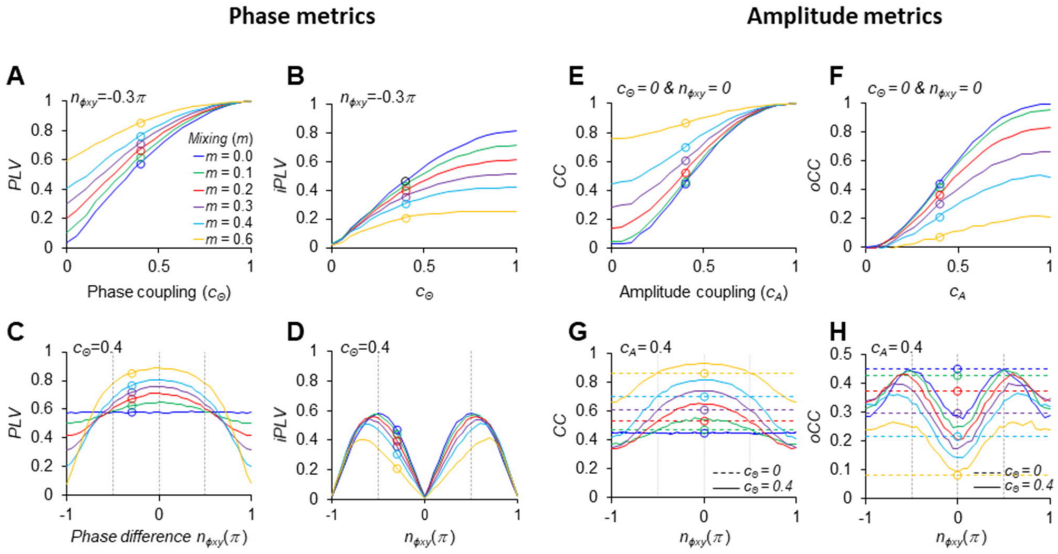

Figure 12 Lag, coupling, and mixing affect phase and amplitude synch estimates. Two signals with distinct coupling strength for amplitude (c_A) and phase (c_Θ), and phase difference ($n_{\phi xy}$) were simulated and linearly mixed with a range of mixing strengths (m). The mean phase or amplitude coupling were then estimated. **(A)** PLV and **(B)** iPLV estimates as a function of phase coupling (c_Θ) and mixing (m) given phase difference ($n_{\phi xy}$) of -0.3π as indicated by markers in **(C–D)**, respectively. **(C)** PLV and **(D)** iPLV as a function of $n_{\phi xy}$ given $c_\Theta = 0.4$ as indicated by markers in **(A)** and **(B)**, respectively. Mixing has strong influences on both PLV and iPLV estimates. Near zero $n_{\phi xy}$ positively biases PLV, whereas the mixing biased to iPLV is strongest near $n\phi_{xy} = \pm 0.5\pi$ and iPLV approaches zero when $n\phi_{xy} = 0$ or $n\phi_{xy} = \pm\pi$. **(E)** *CC* and **(F)** oCC with regression-based orthogonalization (Brookes et al., 2012) estimates as a function of c_A and m when $c_\Theta = 0$ and $n_{\phi xy} = 0$ as indicated by markers in **(G–H)**, respectively. **(G)** *CC* and **(H)** oCC estimates as a function of $n_{\phi xy}$ when $c_A = 0.4$ and $c_\Theta = 0.4$ (solid lines) $c_\Theta = 0$ (dashed lines). When a phase coupling is present in addition to the amplitude coupling, both *CC* and *oCC* are biased by $n_{\phi xy}$, but in different manners. Figures adapted with permission from (Palva et al., 2018); Creative Commons license(CC BY-NC-ND 4.0).

When there is a constant phase coupling (C_Θ=0.4), PLV estimates can be either positive or negatively biased by mixing depending on the phase lag of the true interaction (coloured lines, Figure 12C). As phase-lag approaching zero-degree, positive bias to PLV was at maximum because the phase lag of true coupling works 'synergistically' with zero-degree phase lag contributed by linear mixing. On the other hand, when phase lag approaching +π or -π, the true interaction became anti-phase with zero-degree phase lag of mixing. Therefore, the PLV estimates of the true interaction was partially cancelled by mixing, and the magnitude of this negative bias depended on the strength of mixing. On the other hand, iPLV estimates depended on the phase lags in a non-linear manner, and it failed to detect the true interaction with zero-degree, +π, and -π phase lag (Figure 12D) because iPLV is the projection of the vector of the complex-valued PLV on to the imaginary axis (Figure 11D).

4.3.4 Mixing, amplitude coupling, and phase dynamics affect CC and oCC estimates

The anecdotal example (Figure 11) and grid-source model (Fig 2 of Study III) showed that mixing affects CC and oCC in the same manner as mixing does to PLV and iPLV respectively on local-level as biased estimates and on graph-level. We systematically manipulated three parameters as amplitude coupling (c_A = 0 … 1; Eqs. 1–2), mixing (m = 0 … 0.6), phase lag (ϕ_{xy} = −π … π) when simultaneously introducing phase coupling (C_Θ = 0.4) and amplitude coupling (C_A= 0.4) between two simulated signals $x(t)$ and $y(t)$. For each realization of the $x(t)$ and $y(t)$ time series, we estimated the amplitude coupling with CC and oCC. In the absence of concurrent phase coupling and lag (C_Θ=0, ϕ_{xy} =0), both CC and oCC estimates increased monotonically as coupling increased (Figure 12E–F), and the overall effects of mixing to CC and oCC estimates were similar to that of PLV and iPLV, respectively (Figure 12 A–B).

However, when simultaneously introducing phase coupling (C_Θ = 0.4) and amplitude coupling (C_A=0.4) into the signals, CC and oCC estimates showed more complex non-linear dependency on linear mixing and phase lag (solid lines, Figure 12 G & H) comparing to in the absence of phase coupling (dashed lines, Figure 12 G & H). Mixing inflated the CC estimates (Figure 12 G) by aligning the peaks and troughs in two signals. Similar to the observation of PLV (Figure 12 C), phase lag inflated CC estimates when approaching in-phase and dampened CC estimates as approaching anti-phase with instantaneous effects of mixing – which was due to the alignment or misalignment of the peaks and troughs of the two signals in these two extreme cases of phase lag, respectively.

When only amplitude coupling is present (C_A=0.4, C_Θ=0, ϕ_{xy} =-π…+π), oCC progressively underestimated the amplitude coupling as mixing increases (dashed lines, Figure 12 H). In the presence of concurrent amplitude (C_A=0.4) and phase coupling (C_Θ = 0.4), the oCC estimates (Solid lines, Figure 12 H) showed a complex nonlinear dependency on phase lag and mixing resembling that of iPLV (Figure 12D). The oCC estimates were most dampened when phase lag approaching zero and most inflated as phase lag near +0.5π or -0.5π. Prior to computing correlation, the orthogonalization either regresses out the real-valued contribution of signal $x(t)$ to $y(t)$ (Brookes et al., 2014) or uses the imaginary component of the cross-terms between $x(t)$ and $y(t)$ (Hipp et al., 2012). In either way, the real or imaginary part of a complex-valued signal mixes phase with amplitude information. Phase coupling resulted in a deviation from a uniform distribution of phase lag, which affected orthogonalization in a non-trivial way. For example, for two originally highly similar time series (*i.e.*, zero-degree phase lag), after orthogonalization, their correlation will become negligible because the highly similar component is removed from one signal. On the other hand, when the phase lag approaching ±0.5π, the orthogonalization would have virtually no effects even if there are correlations induced by signal mixing.

To summarize, CC and oCC estimates of amplitude correlation can be significantly impacted by concurrent phase and amplitude coupling in two signals. Irrespective of the orthogonalization procedure used, the oCC estimates are always affected by the presence of phase coupling with a non-linear dependency on phase-lag and mixing strength. This means that, in the most extreme cases, the oCC could falsely report amplitude coupling in the absence of true amplitude coupling (Supplementary Fig 1 & 2 of Study III).

4.4 Study IV–V: hyperedge bundling as a practical solution to ghost interactions

As detailed in study III, irrespective of the choice of phase or amplitude metrics, mixing causes ghosts SIs in measured FC connectomes that are difficult to remove. We advanced a generic approach for correcting false-positive (FP) ghost (SIs) interactions in FC connectomes of source-reconstructed MEG/EEG data. This novel approach aims to bundle observed FC raw edges, regardless of their true-positive (TP) or FP nature, into

hyperedges by their inter-edge signal mixing adjacency. With realistic simulations, we showed that bundling of raw edges yielded hyperedges with much improved separability of TP and suffers little loss in true positive rate (TPR). Moreover, hyperedge significantly decreased graph noise by maximizing the TP to FP ratio. We also demonstrated the advantage of edge bundling in visualization of large-scale cortical networks derived from real MEG experiments. In summary, hypergraphs yielded by this bundling approach well represented the true long-range cortical interactions that were detectable and dissociable using MEG/EEG source data.

4.4.1 Theory of hyperedge bundling demonstrated with a toy model

Signal linear mixing smears one true interaction into a multitude of ghost SIs in the vicinity of the true interaction (Figure 13 A, see also Figure 2). Thus, finding the edge adjacency (Figure 13B) between the true interaction and its ghost neighbours could offer a solution to bundle raw edges into one hyperedge (Figure 13C–D).

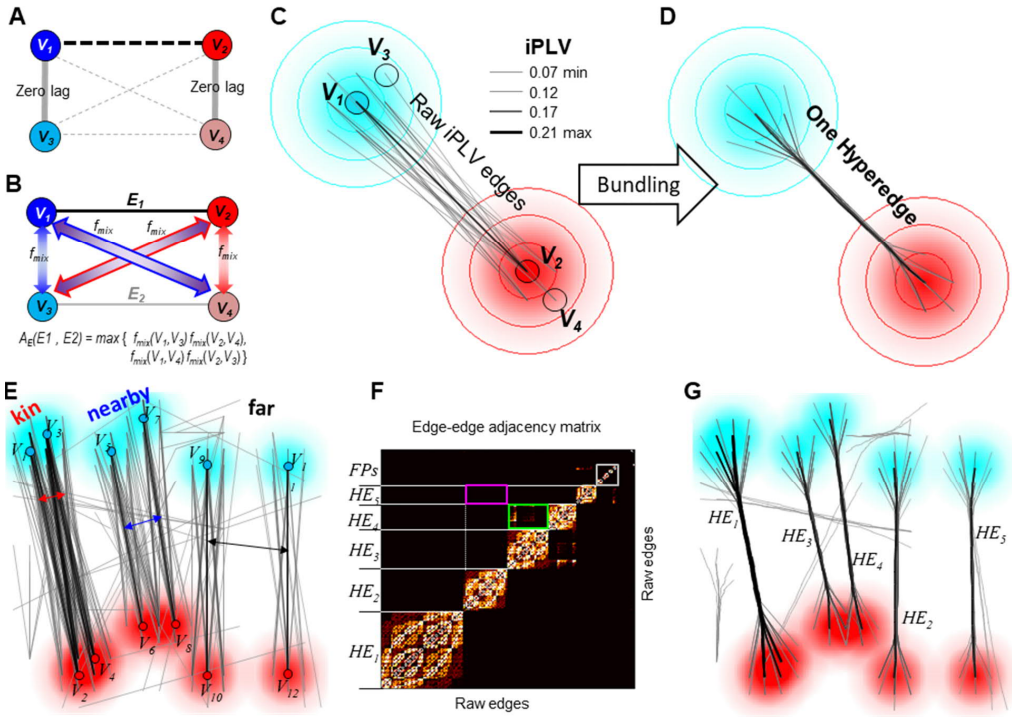

Figure 13 Theory: raw edges can be bundled into hyperedges. (**A**) Mixing is instantaneous so false positive artificial interactions (AIs) are zero-lag (thick grey), but ghost SIs inherit the lag of the true interaction (dashed). **(B)** The edge adjacency (A_E) between two raw edges E_1 and E_2 is the maximum product of constituent nodes' mixing function (f_{mix}). **(C)** Non-zero lag ghost interactions (SIs) arise from the mixing neighbourhood of true interactions and thus share large edge adjacency with the true interactions. **(D)** Characterizing the mixing between the true-positive and its ghosts allows bundling of raw iPLV edges from **(C)** into one true-positive hyperedge. **(E)** Three pairs of true edges of varying spatial distance were simulated and the all-to-all connectivity was estimated with iPLV. **(F)** To bundle raw edges, first we estimate the edge-edge adjacency between all pairs of raw edges, then partition the resulting adjacency matrix into clusters. Thereby, each row represents one raw edge and each cluster represents a hyperedge ($HE_{1–5}$). The grey box indicates false-positive hyperedges (FPs); the magenta and green boxes indicate the inter-hyperedge similarity between the "far" and "nearby" pair. **(G)** Visualization of the hyperedges defined in **(F)**. Figures adapted with permission from (Wang et al., 2018); Creative Commons license(CC BY-NC-ND 4.0).

To show that bundling is applicable to separate multiple true interactions, we simulated a scenario with six true edges of three degrees of adjacency as “kin”, “nearby”, and “far”. The estimated raw graph using iPLV contains all six TP raw edges and dozens of surrounding FP ghost SIs (Figure 13E). Estimating and then partitioning the edge adjacency matrix revealed that the two TP “kin” raw edges together with their ghost SIs were inseparable and thus bundled into the largest hyperedge HE_1 (Figure 13F); the “far” pair and their ghost were bundled into two clearly separable hyperedges HE_2 and HE_5; the “nearby” pair and their ghost SIs were also clustered into two distinct hyperedges HE_3 and HE_4 with greater inter-hyperedge similarity as measured by mean-linkage (green box) than the “far” pair (magenta box). Additionally, a few scattered random FP edges were also observed and clustered into several hyperedges (gray box), each of which was much smaller in size than any of the hyperedges containing TP raw edge(s).

Thus, if a hyperedge containing at least one true raw edge is considered as a TP observation, bundling greatly decreased graph noise in terms of the FP/TP ratio. For example, FP/TP in raw graph was 239/6 and 4/5 in the hypergraph, which was a remarkable reduction in the fraction of FPs by a factor of 50. Visualizing these bundles showed that the hypergraph had less visual cluttering and better facilitated the identification of true interactions compared to the raw graph (Figure 13G).

4.4.2 Quantifying the mixing function is a prerequisite to hyperedge bundling

We next quantified the mixing function between MEG sources. The signal mixing between the measurement of two sources is instantaneous and therefore always leads to inflated zero-lag correlations (Figure 11). The mixing between reconstructed cortical sources used in this study was quantified by a matrix A_{mix} of dimension $n \times n$ (parcels), in which, each element was a mixing function (f_{mix}) that characterizes the amount of mixing between two parcels, *e.g.*, $f_{mix}(V_1, V_3)$ (Figure 13B). For truly uncorrelated signals between V_1 and V_3, the zero-lag correlation between reconstructed signals measures the mixing captured in forward- and inverse-transform. Here, f_{mix} was quantified as the PLV between reconstructed parcel time series of uncorrelated noise using simulation (illustrated in Figure 3, 5, & 6 of Study V).

Observed mixing and ghost SIs in the MEG parcels resembled that of toy model (Figure 14A–B), where all three AI-free phase metrics reported highly similar ghost SIs connection patterns (Figure 14C). The mixing effect between sources persisted across spatial resolution of the source space or cortical parcellation scheme (Figure 14D). Parcels having high mixing with neighbours located mostly in sulci and predominantly in deep sources such as the cingulate, insula, inferior parts of occipital, temporal, and fontal region (Figure 14E). In contrast, the parcels having high modeling accuracy (fidelity) situated mostly on the dorsal and lateral aspects of the brain, predominantly on gyri (Figure 14F). Parcel mixing and fidelity were negatively correlated (Figure 14G, Spearman's rank correlation coefficient $\rho=-0.82$), which indicates that high fidelity parcels tend to have low residual spread. Additionally, for Monte Carlo simulation of 200 uniformly distributed edge with coupling of 0.9, the iPLV estimates of TP edges were highly correlated with edge fidelity (Spearman's correlation $\rho=0.91$, Figure 14H). Therefore, the geometric features of the source reconstruction accuracy might also bias the FC estimates in addition to mixing.

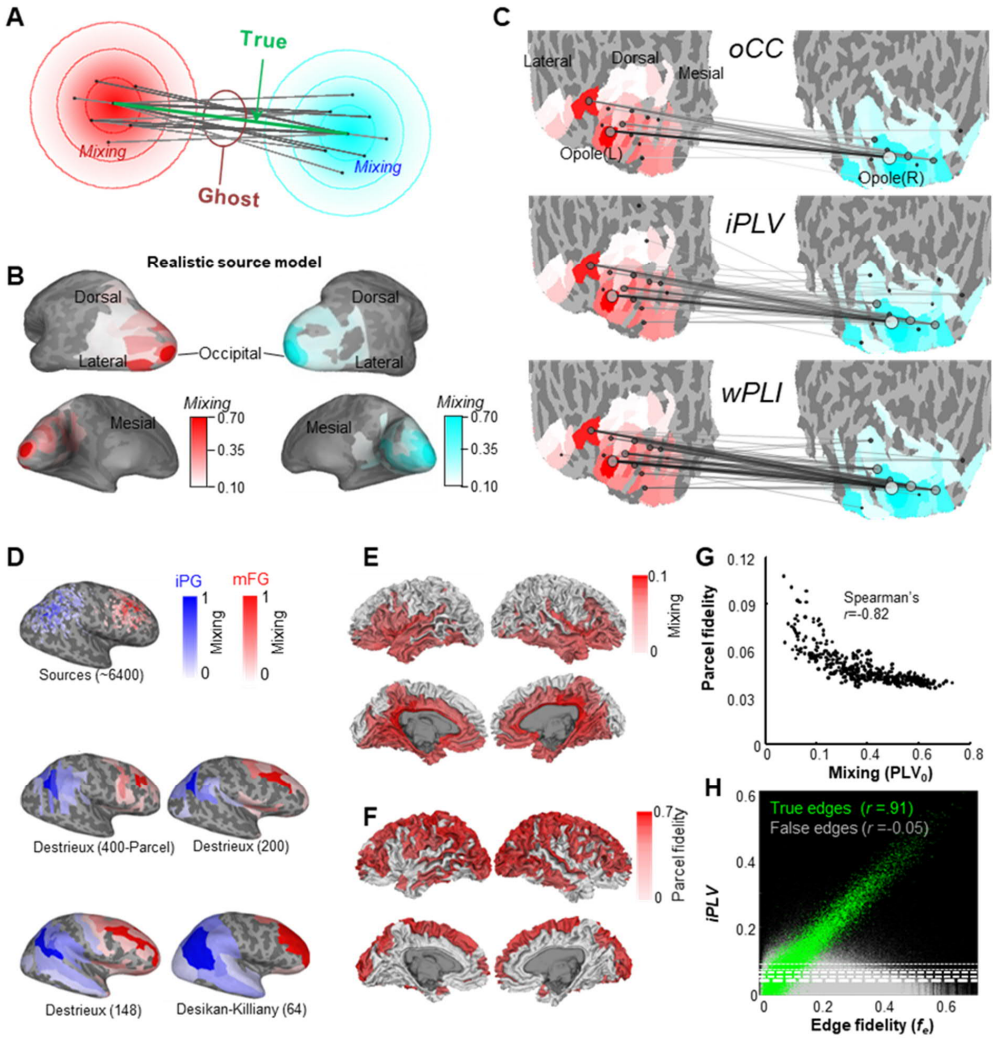

Figure 14 Quantifying mixing in cortical sources. **(A)** The toy model predicts the mixing between MEG/EEG sources and the observation of ghost SIs in the vicinity of true interaction(s). **(B)** An example of mixing from two MEG sources to neighbouring sources, where mixing (PLV_0) is the PLV between uncorrelated null hypothesis time series from parcels. **(C)** SIs were seen in graphs estimated using amplitude and phase metrics. Amplitude or phase coupling were simulated between left and right occipital while the rest parcels were uncorrelated. All-to-all synchrony were estimated with *oCC*, *iPLV* and *wPLI*. The strongest 60 edges were shown. oCC graph (Brookes, 2012) was computed using time series that was simulated with $c_A = 0.9$, $c_\Theta = 0$. *iPLV* and *wPLI* graphs were computed using time series that were simulated with $c_A = 0$, $c_\Theta = 0.9$, $n\varphi_{xy} = -0.5$. **(D)** An example of persistent effects of mixing from two sources to their neighbours across several spatial resolutions or cortical parcellation of MEG/EEG source models; iPG: inferior parietal gyrus; mFG: medieal frontal gyrus. **(E)** Mean PLV_0 between one parcel to the rest of the parcels characterizes the mixing of that parcel. **(F)** Parcel fidelity quantifies the accuracy of source reconstruction. **(G)** Correlation between group-level mean PLV_0 and parcel fidelity. **(H)** Estimated iPLV of simulated edges (green dots) are correlated with edge fidelity even when all ground-truth interactions are simulated with identical strength. These iPLV edges were pooled from 100 simulations containing 2×10^4 true- and 8×10^6 false-interactions; dashed lines indicate the threshold criteria ranging from $-\log_{10}(p) = 1.3$ (thin) to 5 (thick). **(A–D)** adapted with permission from (Palva et al., 2018); Creative Commons license(CC BY-NC-ND 4.0). **(E–H)** adapted with permission from (Wang et al., 2018); Creative Commons license(CC BY-NC-ND 4.0).

4.4.3 How to bundle raw edges into hyperedges

As illustrated with the toy model (Figure 13), we aimed to bundle raw edges from a raw graph (A_{FC}) (Figure 15A) into hyperedges for improved graph quality and better visualization (Figure 14B). First, the raw edges of $A_{FC} \in \mathbb{R}^{n \times n}$ of n parcels (Figure 15C) were parsed into a list of node pairs (Figure 15D). Next, the mixing f_{mix} between all involved nodes of these raw edges were fetched from the A_{mix} matrix (Figure 15E) for computing edge adjacency (Figure 15F) for all edges, which resulted in an edge-edge adjacency matrix $A_E \in \mathbb{R}^{m \times m}$ for m number of raw edges (Figure 15G).

The rows of matrix A_E are the *mixing profiles* of individual raw edges (Figure 15H). For example, $A_E(i)$ and $A_E(j)$ are the mixing profiles of edges E_i and E_j respectively, and $A_E(i)$ and $A_E(j)$ indicate mixing adjacency of E_i and E_j to all other raw edges in the graph. If E_i and E_j are close in mixing, there will be a high correlation between their mixing profile $A_E(i)$ and $A_E(j)$; and there will be no correlation otherwise (Figure 15I). Thus, assessing the mixing profiles similarity between all pairs of edges resulted in a mixing similarity matrix $S_E \in \mathbb{R}^{m \times m}$ for m raw edges (Figure 15J). Hyperedge bundling is based on the notion that a measured matrix S_E can be partitioned into clusters of raw edges. Thus, raw edges from a cluster are similar to each other in mixing and therefore to collectively reflect a shared true underlying interaction (Figure 15K).

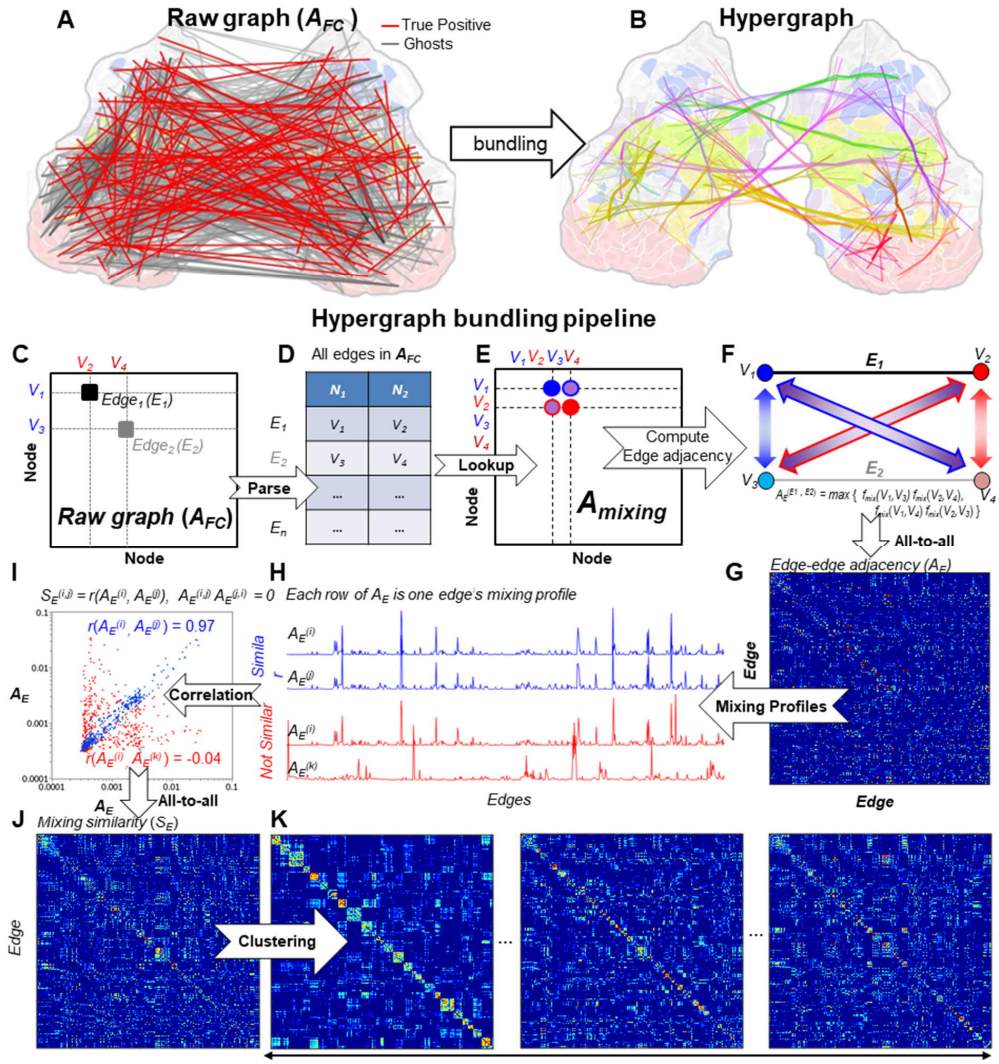

Figure 15 Bundling of raw edges into hyperedges in MEG/EEG data. **(A)** In an example of estimated iPLV graph, the ghost SIs (gray) overwhelm true positives (red, n=200). The edges are overlaid on a flattened cortical map colour-coded by Yeo systems. **(B)** After applying bundling to **(A)**, the resulting hypergraph contains mostly true positive hyperedges. **(C–K)** The hyperedge bundling procedure. **(C)** E_1: a true interaction and E_2, one of E_1's SIs, from raw graph A_{FC} are schematically shown in matrix form. A_{FC} is a sparse matrix containing only significant edges. **(D)** Parsing A_{FC} into a list edges, *i.e.*, node pairs. **(F)** For true positive E_1 and its ghost E_2, we look up the mixing (f_{mix}) between all of their constituent nodes from the mixing matrix A_{mix}. **(F)** Computing the edge adjacency A_E between E_1 and E_2, *i.e.*, the maximum product of constituent nodes' f_{mix}. **(G)** Computing Edge Adjacency for all edges pairs from **(D)**. **(H)** Examples of edge-pairs that are similar (blue) and not similar (red) in mixing profiles. **(I)** The Edge Mixing Similarity (S_E) between an edge-pairs is the correlation between that edge-pair's mixing profiles. **(J)** The resulting S_E matrix. **(K)** Partitioning S_E will yield hypergraphs with varying degree of resolution. Figures adapted with permission from (Wang et al., 2018); Creative Commons license(CC BY-NC-ND 4.0).

4.4.4 Hyperedge bundling drastically improves graph quality

We conducted realistic simulations to assess the performance of hyperedges in detecting TP cortical interactions (technical details in Figure 3 of Study V and Figure 3 of Study IV). The simulation included a large number of ground-truth graphs containing TP interaction of a varying degree of average coupling strength and a variety of distribution in coupling strength.

First, a bootstrap procedure was used together with two clustering methods for identifying the resolution range that yields stable partitioning solutions for hyperedges (detailed in Methods of Study IV, and Figure 2 of Study V). When the resolution parameter CL was below 0.4, both UPGMA and Louvain clustering methods yielded significantly more stable partitions in terms of variation of information (Meila, 2007) of measured iPLV graphs than their randomly rewired counterparts (Figure 16A). For graphs containing 640 raw edges, this CL upper bound corresponded to ~250 hyperedges. Within the stable clustering range ($0.05 < CL < 0.45$), as resolution increased, the resulting hypergraphs showed a systematic shift towards increasing number of smaller hyperedges. The Louvain algorithm consistently yielded more hyperedges of small sizes than UPGMA (Figure 16B).

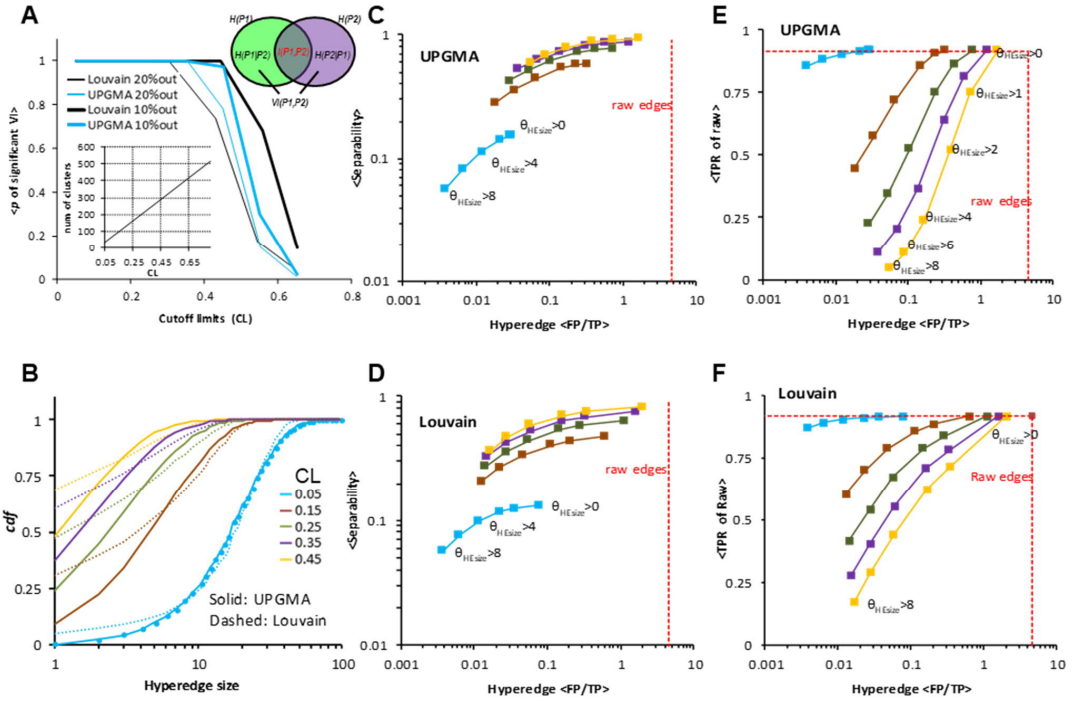

Figure 16 Hyperedge bundling greatly improves the graph quality. **(A)** Hypergraphs created with both UPGMA and Louvain algorithms were stable below cut-off limit (CL) of 0.4 that is the 40% of the dendrogram; inset: hyperedge number as a function of CL; top-right: the variation of information $VI = H(P_1) + H(P_2) - 2I$; H: entropy; I: mutual information; P1 and P2 are clustering solutions (Meila, 2007). **(B)** The cumulative distribution (cdf) of hyperedge size at different levels of CL; the cdf was obtained with hyperedges pooled from 500 simulated graphs and within each graph 100 iterations. **(C–D)** Increasingly strict hyperedge size threshold, where size referring to raw edge number within a hyperedge (θ_{HEsize} varying from 0 to 8) resulted in a monotonic decrease in separability and noise (FP/TP). **(E–F)** The retained true positive raw edges decreased as hyperedge size threshold increased. As a reference, in **(C–F)** the performance of raw edges was shown as red dashed lines. Figures adapted with permission from (Wang et al., 2018); Creative Commons license(CC BY-NC-ND 4.0).

There is a trade-off between separability of TP raw edges, true positive rate (TPR), and graph noise. Bundling aims to detect and separate as many TP interactions as possible while rejecting as many FP as possible, which involves finding an optimal balance among these competing interests by taking into account two aspects of hyperedges: *separability* and *noise* level. Here separability was defined as the ratio between singleton TP hyperedges (containing only one TP raw edge) and all TP hyperedges, and noise as the FP/TP ratio of the hyperedges. An ideal hyperedge partitioning would thus has separability of 1 and noise FP/TP near 0, and a TPR equal to the TPR of raw edges.

As we increased clustering resolution, both separability and noise increased for both clustering methods (Figure 16C–4D). This was due to the fact that at low resolutions, multiple TP raw edges were partitioned into one hyperedge and there were few FP hyperedges. At high resolutions, separability was improved but at the cost of having greater numbers of FPs. Meanwhile, excluding small hyperedges would likely decrease noise because in the toy model FP hyperedges contains fewer raw edges than TP hyperedges (Figure 13). Across all hypergraph resolution, excluding small hyperedges lead to a decrease in noise (markers along the curves, Figure 16C–D). Nevertheless, this benefit in graph quality came at the cost of reduced separability (Figure 16C & D) and a reduced TPR (Fig 16E–F) which was due to the removal of small-sized TP hyperedges together with FP hyperedges.

To summarize, hypergraphs across all resolutions were consistently less noisy than raw edge graphs. In the least noisy hypergraph (*e.g.*, Louvain, CL = 0.05 and $\theta_{HEsize} > 8$), 87% of the 125 TP raw edges were retained while noise decreased from (640-125)/125 = 4.1 in raw graphs to 3.8×10^{-3} (leftmost filled box on the cyan curve, Fig 15F). This marked a 10^3-fold decrease in noise compared to its original raw graph. Nevertheless, this improvement was achieved at the cost of poor separability, meaning many hyperedges in CL = 0.05 graphs contained several true edges. For analyzing with experimentally mapped raw FC, one option for balancing the trade-off would be using CL ≥ 0.15 and $\theta_{HEsize} > 2$, with which in simulations there was an expected reduction of FP/TP to 0.1 (comparing 4.1 in raw edges) with negligible reduction in TPR and adequate separability (0.5).

4.4.5 Applying hyperedge bundling to real MEG data

Last, to assess the feasibility of hyperedge, we tested bundling with FC derived from real MEG measurement during a visual working memory task. We applied bundling to raw FC graphs that reflected significant strengthening of inter-areal phase synchrony during memory retention compared to pre-stimulus baseline. The iPLV estimates in α- and γ-band were greater during memory retention than in pre-stimulus baseline. We plotted the 1000 strongest iPLV edges on a flattened cortical surface (Figure 17A–B). After applying hyperedge bundling (using UPGMA with CL=0.15, $\theta_{HEsize}>6$) to these raw graphs, the resulting hypergraphs, like that of simulated graphs (Figure 15B), offered better visualization of large-scale FC than raw graphs, emphasizing the long-range synchrony (Figure 17C–D). The bundling approach has also been applied to study large-scale 1:1 phase synchrony (Hirvonen et al., 2017)and cross-frequency synchrony (F. Siebenhühner et al., 2016).

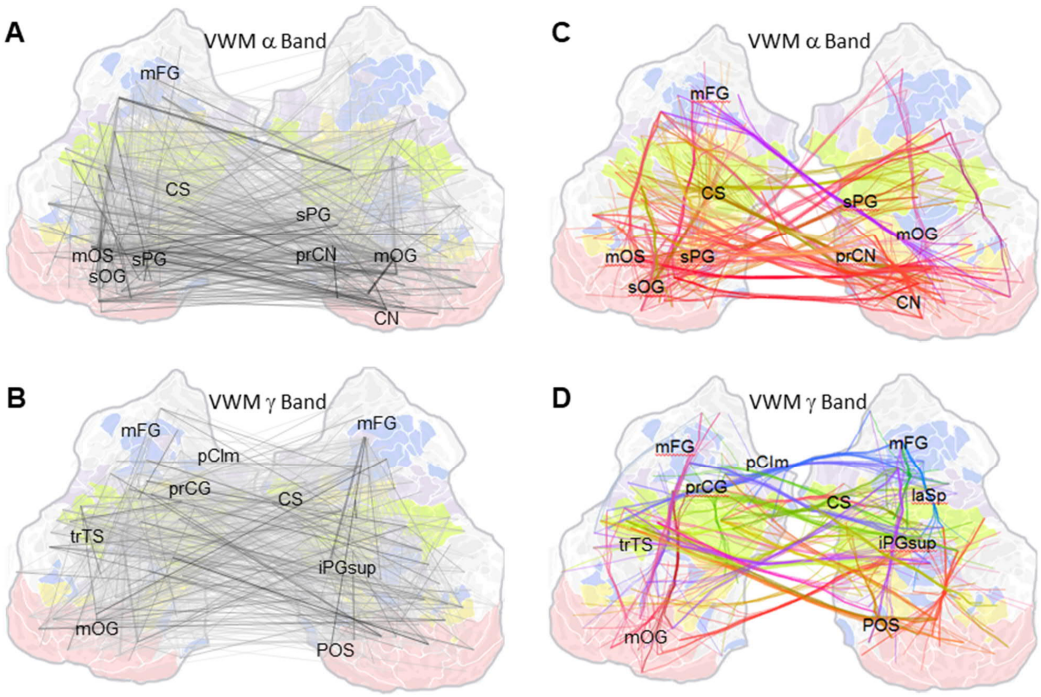

Figure 17 Hypergraphs improve visualization of real and simulated data**. (A)** Estimated group-level iPLV edges in α-band and **(B)** γ-band 1:1 phase synchrony during the retention period of a visual working memory MEG experiment show significant visual crowding. **(C–D)** Hypergraphs of **(A–B)**, respectively. Hyperedges are created with CL=0.15, $\theta_{HEsize} > 6$. On these 2D maps, different parcel colours indicate functional sub-systems defined by (Yeo et al. 2011) and in hypergraphs, edge colours are obtained by mixing of the colours of connected parcels. CN: cuneus; CS: central sulcus; iPGsup: supramarginal gyrus; mFG: middle frontal gyrus; mOG: middle occipital gyrus; mOS: middle occipital sulcus and lunatus sulcus; laSp: posterior ramus; prCG: precental gyrus; pCIm: middle posterior cingulate; prCN: precuneus; sPG:superior parietal lobule; sOG: superior occipital gyrus. Figures adapted with permission from (Wang et al., 2018); Creative Commons license(CC BY-NC-ND 4.0).

5 Discussion

We may regard the present state of the universe as the effect of its past and the cause of its future – Pierre Simon Laplace

5.1 Study I: Critical bistability in the brain

We presented converging evidence from a generative model and two experimental datasets to advance the proposal that critical bistability, as a hallmark of first order phase transition, be an important extension to the classic second order neuronal criticality. Our model showed that bistability was associated unambiguously with a local positive feedback loop and occurs exclusively within the critical regime. With increasing state dependency, first order phase transition emerged progressively from the classic criticality of second order phase transition. In the resting-state human brain, bistable critical dynamics was a robust large-scale phenomenon observed in the amplitude dynamics of neuronal oscillations from δ (2Hz) to high γ (40–225 Hz) frequencies. Corroborating with the modeling results, the neuronal bistability positively correlated with LRTCs in θ–α (5.4–11 Hz) and γ band (45–225Hz) frequencies. As evidence for functional significance, moderate bistability was positively correlated with executive functions in healthy subjects, which makes bistability a favourable neuronal feature. However, excessive bistability was associated with epileptic pathophysiology and predictive of the epileptogenic zone. Critical bistability thus characterized spontaneous human brain dynamics in awake resting-state with both physiological and pathophysiological roles. We suggest that these findings expand the framework of brain criticality and imply that near-critical neuronal dynamics involves both first and second order phase transitions in a frequency-, neuroanatomy-, and brain-state-dependent manner.

5.1.1 Dominating positive feedback generates bistability

Positive feedback is one of the few elementary modules that engage in the construction of complex living systems from bottom up (1.1). On the other hand, negative feedback is a key module for homeostasis and conservation. As positive feedback overpowers effective negative feedback, irreversible switching behaviours from one state to another ensues (Nurse, 2008). A growing body of empirical and modeling literature has shown the link between positive feedback or self-facilitation and various forms of bistability across levels of organization including gene regulations (Dubnau and Losick, 2006; Kuwahara and Soyer, 2012), intra-cellular signaling (Bednarz et al., 2014; Mitrophanov and Groisman, 2008), models of local ensembles (Cowan et al., 2016), and large-scale models of cortical bistability (di Santo et al., 2018). Thus, a dominating positive feedback causing bistability is likely universal (Di Santo et al., 2016).

Our model showed that Gaussian (unimodal) and bistable critical regimes were separated by the strength of a positive local feedback loop implemented here by the non-linearity of state-dependent noise ρ. The canonical Hopf bifurcation (Freyer et al., 2012; Izhikevich, 2007) predicts that under the influence of a weak ρ, the dynamics of local ensemble undergoes a super-critical bifurcation, where the ensemble activity (R) only become critical as the control parameter (κ) increases and reaches the exact critical point. This is a second order phase transition conceptually identical to the critical transition from liquid to supercritical matter in H_2O (Figure 3). When under the influence of a strong ρ, the dynamics of R undergoes a sub-critical bifurcation, where R can reach supercritical hyper-synchronized state (*i.e.*, limit cycle) before the fixed-point attractor losing its stability,

which conceptually equates the first order phase transition of H_2O in bistable state (inside the liquid-gas dome, Figure 3). Furthermore, the variable ρ fluctuates at a much slower rate than the fast population activity R, and thus equates a slow physiological variable (Jirsa et al., 2014) reflecting cortical excitability and corresponding resource demand (Cowan et al., 2016; di Santo et al., 2018) that causes bistability in faster neuronal oscillations (Costa et al., 2015).

5.1.2 LRTCs and bistability are coexisting large-scale phenomena and behaviourally relevant

In the model, bistability was positively correlated with LRTCs and the values of the slow variable ρ. In MEG and SEEG recording of resting-state human brain activity, bistability and LRTCs were coexisting phenomena observed in a large portion of cortex in fluctuations of neuronal oscillation from δ to γ-band frequencies. In both MEG and SEEG, the group-level cortical maps of LRTCs and bistability were correlated in α- and γ-band. Interestingly, only SEEG show differences in bistability and LRTCs between functional systems of the brain, with stronger effects in γ-band frequencies.

As the evidence for functional relevance, MEG θ–α band bistability and LRTCs were positively correlated with the assessment of subject executive functions, which suggested high bistability and LRTCs be beneficial. However, in SEEG, β- and γ-band bistability but not LRTCs were the most important features for classifying epileptogenic zones, which supported the proposal that high bistability in fast brain oscillations is indicative of pathologically elevated excitability and higher demand for resources.

5.1.3 High level bistability signals catastrophic shifts

Although linking model observation of high SEEG bistability to the nonlinearities of ρ and positive feedback with the current empirical observation seems speculative, we suggest subsystem-specific high bistability such as in limbic system be indicative of a shift towards catastrophic events – a phenomenon similar to many other complex systems undergoing a strong subcritical Hopf bifurcation (see (Villa Martín et al., 2015) and references). The bistable phases of sub- and super-critical dynamics associate with hysteresis, which means a tendency to dwell in either a hyper-synchronized up-state or a subcritical disordered down-state. In other words, the ensemble avoids the 'moderate' level of synchrony as expected by the classic criticality models. Physiologically, the hyper-synchronized state corresponds to a resource-demanding phase of large amplitude oscillations, whereas the down-state (a fixed-point attractor) reflects resource recharging or recovery after depletion.

In a wide range of systems, high degree of bistability is invariably associated with maladaptive behaviours or catastrophic shifts (Bak, 1996; Thom, 1972; Zeeman, 1976). Such examples include catastrophes in noise systems (Agu and Teramachi, 1978), unpredictable and violent vibrations in aerodynamical systems (Qi and Zhongke, 2015), irreversible environmental changes in ecosystems (Boerlijst et al., 2013; Villa Martín et al., 2015), wars and conflicts in societies (Díaz, 2017), and seizures in the brain (Breakspear et al., 2006; Jirsa et al., 2014; Roberts et al., 2017b; Robinson et al., 2002). In these examples, slowly varying driving forces or changing in individual component behaviours leads to abrupt changes in system-level behaviour, and hence it embodies a theory of great generality between gradualism or catastrophism in all aspects of nature (Bak, 1996; Thom, 1972; Zeeman, 1976).

5.2 Study II: Large-scale HFO synchrony

High-gamma activity (HGA) and high-frequency oscillations (HFOs) are two forms of fast neuronal activity that have been thought to emerge from local circuits with no long-range coupling but HGA amplitude

correlations (Vidal et al., 2012) and co-occurrence of oscillatory ripple bursts (Buzsáki and Silva, 2012; Khodagholy et al., 2017; Logothetis et al., 2012; Novitskaya et al., 2016; Vaz et al., 2019). Here, we reported in wakeful resting human brain activity, neocortical HFOs (100–400 Hz) showing long-range phase synchrony that indicated millisecond-order transmission of temporally aligned neuronal spiking on large-scale brain networks. We showed with a battery of rigid tests and control analyses that HFO synchrony was a reliable large-scale phenomenon and unlikely due to pathophysiology and other physiological or technical artefacts. These findings were further supported by the separability of different HFO components in the micro-scale laminar profiles. On systems-level, HFO synchrony exhibited laminar specific connectivity and non-random connectivity patterns with the most pronounced connectivity within limbic and between limbic and other functional systems. Hence, unlike HGA amplitude correlations or HFO burst co-occurrence, the HFO phase synchrony constituted direct evidence for the transmission of HFO signals *per se*. These findings hence open a new avenue in understanding how the putative rhythmic spike synchrony in locally coherent assemblies can evoke HFO potentials in distal target ensembles.

5.2.1 HFOs were different from broad-band HGA

Several lines of evidence in our results have suggested that HFO synchrony – rather than broadband HGA correlation – engage in phase coupling of rhythmic population activity. First, the grand-average synchrony spectra showed a peak in the range of 150–210 Hz (Figure 8C–E). Clustering analysis of individual synchrony spectra confirmed that a majority of the subjects show three peaks in their phase synchrony spectra at 150–210 Hz, 210–300 Hz, and 300–400 Hz (Figure 9). Assessing the similarity between HFO narrow-band connectomes (in Schaefer 100-parcel) revealed that subdivision of HFO bands showed separable macro-scale cortical topological features (Figure 9E–H). Taken together, the demarcation of subdivisions of HFO frequencies in these data indicated that the HFO synchrony did not arise from inter-areal coupling of broadband MUA.

5.2.2 Laminar differentiation between slow-rhythm and HFO synchrony

Sampled locations in deep cortical layers demonstrated stronger HFO synchrony than in superficial layers, which constituted an opposite laminar profile in the range of 2–20 Hz (Figure 8G). This laminar differentiation between slow-rhythm and HFO synchrony indicated that HFOs originate from current sources distinct from those of low-frequency oscillations (Arnulfo et al., 2015; Halgren et al., 2018b). This finding was in line with previous studies in animals that have shown ripple oscillation demonstrating maximum amplitude in layer V ensembles (Buzsáki and Silva, 2012) whereas θ- and α-band oscillations current sources are strongest in superficial cortical layers (Bastos et al., 2015; Lee et al., 2013). Therefore, the HFO synchrony was unlikely a by-product of neuronal interactions between slower cortical oscillations, but rather a hitherto poorly understood component in the organization of large-scale brain dynamics.

5.2.3 HFO show task modulation in task-relevant regions

In addition to characterizing resting-state brain activity, HFO synchrony was also functionally significant during tasks. We used a visuomotor task to induce event-related HFO synchronization and desynchronization in separate sub-band in the HFO frequencies, which is commonly seen for task-related synchrony in slower frequencies (Lobier et al., 2018). This functional significance of HFO synchrony is in line with a recent study in non-human primates that showed local synchrony between inter-neuronal spikes and 180–220 Hz LFP high-gamma oscillations to be predictive of visuomotor reaction times (Khamechian et al., 2019). Moreover, the HFO phase synchrony was dependent on contact-pair concurrent large HFO amplitude, with the latter reflecting the internal coherence of the local assemblies (Ray et al., 2008). Therefore, both local and long-range HFO

synchrony may be functionally significant in neuronal communication. We propose that the bursts of synchronized HFO oscillations observed here reflect the broadcasting and transmission of brief packets of information in large-scale neocortical networks.

5.2.4 The HFO synchrony does not reflect pathophysiology

It is non-trivial to distinguish physiological HFOs from pathological HFOs (pHFOs) because they do share overlapping spectrum (for review see (Frauscher et al., 2017; Jefferys et al., 2012; Köhling and Staley, 2011)). A large body of studies has reported physiological HFOs in animals (Buzsáki and Silva, 2012; Engel and da Silva, 2012; Jones et al., 2000; Logothetis et al., 2012; Novitskaya et al., 2016). On the other hand, pHFOs remain a matter of contention. Documented pHFOs include 80 –250Hz ripples to 250–500 Hz fast ripples (Bragin et al., 2002; Jacobs et al., 2009), and 500–1,000Hz very fast ripples to 1,000-2,000Hz ultrafast ripples (Brázdil et al., 2017). These pHFOs have been suggested as biomarkers for epileptogenic brain tissues and epileptogenicity (Bragin et al., 2002; Brázdil et al., 2017), seizure-onset zone (Jacobs et al., 2009), and predictor of surgical outcome (Jacobs et al., 2010). However, recent studies also have shown that HFOs are not necessarily better markers of epileptogenic tissues than epileptic spikes as earlier research has suggested (Jacobs et al., 2018; Roehri et al., 2018), which questions the usage of HFO as a biomarker for pathology in an indiscriminating manner.

We address the concern on the physiological or pathophysiological origin of long-range HFO synchrony. First, for the primary analysis of HFO synchrony (*i.e.*, all results but when contrasting nEZ with EZ) we only included contact data recorded from putatively healthy regions (nEZ). Moreover, we excluded inter-ictal spiking events in the primary analyses of HFO synchrony. It is important to dissociate physiological spikes (action potentials) from epileptic spikes that are massive population events with large numbers of action potentials riding 50–100 ms depolarization waves preceded by HFOs (Alvarado-Rojas et al., 2013). If our HFO observations reflected pHFOs, the exclusion of spikes should have greatly diminished the observation of long-range HFO synchrony. Meanwhile, between EZs should have shown more prevalent HFO synchrony if these HFO synchrony were indeed pathological. The nEZs and EZs areas showed no differences in HFO synchrony, although the synchrony spectra in frequencies below HFO differentiated EZ and nEZ. Moreover, the epileptic spike rate was not correlated with HFO synchrony, which further supported the non-pathological origin of HFO synchrony. Last, nEZ and EZ displayed clearly distinct cross-frequency phase-amplitude coupling (PAC) patterns in slow but not fast HFO rhythms (Figure 8I). In nEZ, the phases of θ-band oscillations dominated HFOs amplitudes. In EZ, the phases of θ- and δ-band oscillations coupled with HFOs amplitudes, which was in line with prior finding of coupling between pHFOs and interictal spikes as well as δ waves (Lee et al., 2019; Nonoda et al., 2016). Thus, the HFOs and their long-range synchrony most likely is a property of healthy brain dynamics that is still preserved in epileptogenic areas.

5.3 Study III: the ghost interaction problem

5.3.1 Global and local impacts of signal linear mixing to synchrony estimates

Our simulation showed that, on whole-graph level, signal linear mixing resulted in instantaneous coupling which caused PLV and CC to report a multitude of artificial interactions (AIs) in the absence of true interactions. Although the AI-free metrics such as oCC, iPLV, or weighted phase lag index (wPLI) do not report AIs in the absence of true interaction, they discover a large number of ghost interactions (SIs) among uncorrelated sources in the vicinity of the truly interacting sources. Moreover, mixing affected the phase and amplitude coupling

estimates in different manners. In the presence of mixing, PLV and CC overestimated the true coupling, whereas iPLV and oCC underestimated the coupling strength. The observation of biased iPLV and oCC thus questions the widely accepted concept that linear mixing does not affect the estimates of the AI-free metrics. Furthermore, both mixing and phase lag of the true coupling impacted PLV and iPLV estimates. Therefore, when comparing two contrasted conditions, a change in PLV or iPLV estimates is ambiguous because a change in phase-lag or coupling strength, or the combination of both could all results in a difference in PLV and iPLV estimates – in a signal-mixing dependent manner. Although signal mixing does not affect wPLI estimates, wPLI estimates are dependent on the phase lag and therefore still ambiguous.

As a major methodological discovery, phase coupling among the signals can impact the estimation of amplitude coupling using CC and oCC, which can be further amplified by increasing amounts of linear mixing between the signal sources. Importantly, phase coupling combined with varying degree of phase lag can impact CC and oCC estimates even in the absence of true amplitude coupling. These observations raise serious concerns regarding distinguishing pure phase-coupling from pure amplitude-coupling phenomena, which generally limits the interpretability of such measures in isolation. We assess the performance of phase and amplitude synchrony metrics by tuning all principal parameters. Although we did not inspect the effect of additive noise, our main findings are expected to be identical in the presence of noise. Most importantly, the concerns raised here based on simulations are valid for real experimental conditions including spontaneous activity and evoked-response with or without a contrast experiment condition.

5.3.2 Challenges in identifying synchrony in MEG/EEG data

Our simulations illustrated two primary problems regarding false interpretations of confounded connectivity. First, using AI-free metrics is no guarantee against FP because they are still prone to detecting ghost SIs. All forms of cross-frequency couplings, albeit insensitive to AI, also suffer from the ghost SIs. The ghost SIs are "second order" FP caused by crosstalk between the sources, which persists across all spatial resolutions of the source model. Importantly, the crosstalk as a function of Euclidian distance between MEG/EEG sources is generally not as smooth as the Gaussian crosstalk function in our grid-source simulation. Therefore, ghost interactions could arise at locations rather far away from the true cortical sources. Although the exact crosstalk function is a property of specific inverse solutions, it universally leads to mixing among sources. Therefore, the problem of ghost SIs is qualitatively identical among all source modeling methods. Second, phase correlations combined with linear mixing have complex impacts on CC and oCC estimates of amplitude correlation, which indicates a major limitation on separability of phase and amplitude coupling in experiment data. For instance, in the presence of linear mixing, a strong phase coupling with a near 0.5π phase lag will lead to a large oCC estimate even in the absence of true amplitude coupling between ensembles. Conversely, through the effect of signal-to-noise ratio on the accuracy of phase estimates, phase correlations can also be affected by amplitude dynamics and correlations (J. M. Palva et al., 2010b). We consider the above limitations to be of major importance to the field of EEG and MEG research.

In order to counteract the ghost SI problem, a crucial step is to first obtain the full connectivity graph by estimating synchrony between all MEG/EEG sources, *i.e.*, connectome, instead of analyzing between only few regions-of-interest (ROI). The potential problems of synchrony analysis between ROIs include misinterpreting neuroanatomical original of truly coupled sources, mistakenly identifying a ghost interaction as a true interaction, or falsely identifying the detected interaction as the only present connectivity but failing to discover potential important coupling in the vicinity. When a strong phase correlation is present, linear mixing can lead to

erroneous amplitude correlation estimations. Therefore, systematically assessing phase and amplitude coupling might be helpful for interpreting the findings even when the main interest is to investigate the amplitude coupling.

In a connectivity graph measured using iPLV or oCC, the ghost SIs are discovered mostly in the vicinity of the true connections. Due to the ambiguity of the iPLV or oCC estimates, the strongest estimate or statistically most significant interactions does not necessarily correspond to the true underlying coupling (Figure 14H), which questions the legitimacy of thresholding by the strongest coupling. There are promising new analysis approaches for attenuating the ghost SI problem such as multivariate correction (Brookes et al., 2012; Colclough et al., 2015; Soto et al., 2016) or hyperedge bundling (Study IV).

5.4 Study IV: hyperedge solution to the ghost SI problem

5.4.1 Hyperedge effectively suppress ghost SIs

Hyperedge bundling is superior to the conventional thresholding by edge strength approach. Our simulations showed that due to signal mixing, the true interactions wre overwhelmed by ghost SIs (Figure 13, 16). If left untreated, the ghost SIs would render both the edge localization and FC graph property erroneous (Drakesmith et al., 2015, 2013). Imposing strict select criteria, *e.g.*, by edge strength, is commonly used for increasing the fraction of TP among all observations and useful for focusing on only the most robust effects. Due to the geometric feature of source models, a large portion of interaction with true strong coupling could be estimated to have weak coupling. Moreover, TP weak cortical connections may also play an important role in cognitive functions (Santarnecchi et al., 2014). Thus, under strict threshold, these weak true interactions would have become false negative. Furthermore, biases and instability of graph topological features will be introduced when using arbitrary selection criteria on raw edges (Drakesmith et al., 2015; van Wijk et al., 2010). In our simulation, when applying a strict threshold to raw graphs, the noise (FP/TP) dropped from 4 to 0.1, but the TPR reduced to 0.15. In contrast, hyperedge could preserving a TPR of up to 0.88 while obtain the same noise level 0.1 (see brown line, Figure 16F).

5.4.2 Hyperedge bundling is a generic solution to ghost SIs

Hyperedge bundling is flexible with synchrony metrics and MEG/EEG source models used in FC analysis. We evaluated the mixing function using PLV and used the iPLV for estimating FC connectomes, both the approach and the results are generalizable to other interaction metrics (Figure 14). Essentially identical mixing functions may be obtained by other metrics that quantify a linear relationship, such as the correlation coefficient, or analytically, as suggested by Farahibozorg et al. (2018), and hence there is no need to adapt the mixing function estimation to the choice of the interaction metric applied in the specific analyses. On the other hand, the choice of the MEG/EEG reconstruction methods influences source connectivity analysis through their differences in sensitivity to point-like, distributed, or time-varying source topographies (Hincapié et al., 2017). Although, this thesis employed only linear L2 minimum-norm based inverse operators (Hamalainen and Sarvas, 1989; Hämäläinen and Ilmoniemi, 1994; Lin et al., 2006), the hyperedge bundling can apply to FC derived from other source reconstruction methods as long as the source mixing functions are quantified. Likewise, any parcellation-generation approach, such as the reconstruction-accuracy-optimized (Korhonen et al., 2014) or adaptive (Farahibozorg et al., 2018) parcellations with a reasonable number of sources or parcels (Figure 14) will work well with hyperedge bundling.

5.4.3 Balancing the trade-off between TPR, noise, and separability

In the current setup, hyperedge bundling is controlled by two parameters as the cut-off limit (CL) and the hyperedge size threshold (θ_{HEsize}). CL determines hypergraph resolution and balance between noise (FP/TP) and *separability* of TP hyperedges. Low hypergraph resolution lead to low noise but poor separability. θ_{HEsize} can be used to prune the smallest hyperedges to further reduce noise, albeit at a cost of pruning some TP hyperedges. We compared the performance of two clustering methods. While there are some technical differences (Figure 5 of Study IV), overall, when tuning CL = 0.15–0.25 and θ_{HEsize} = 1–2, hypergraphs created by both methods have greatly reduced graph noise (a drop from 4 to 0.1–0.2 in FP/TP) with satisfactory separability and negligible reduction in TPR. When applying hyperedge bundling to experimentally measured FC data where the truth of interactions is unknown, choosing parameters can be based on both our simulation results and objectives of the research. For example, if the main objective requires high separability such as establishing connectivity between specific visual areas, one should choose high resolution hypergraphs, but this will be accompanied by sub-optimal noise reduction. On the contrary, if the objective is to establish overall connectivity between occipital and parietal regions, a low-resolution hypergraph (with low noise) is sufficient.

Acknowledgements

I carried out this work under the supervision of Drs. J Matias Palva and Satu O Palva at the Neuroscience Center, Helsinki Institute of Life Sciences, and under the doctoral programme Brain and Mind (B&M) at the University of Helsinki. I am meanwhile a visiting researcher at the Department of Neuroscience and Biomedical Engineering, Aalto University. The MEG data acquisition was carried out by Santeri Rouhinen, Felix Siebenhühner, and I at the BioMag Laboratory, Helsinki University Central Hospital. The SEEG data were recorded at Claudio Munari Epilepsy Surgery Centre, Niguarda Hospital of Milan, Italy and were kindly provided by Dr. Lino Nobili. Below a list of people to whom I would like to extend my gratitude.

I first thank **Satu** and **Matias** for financially supporting me to complete this work. I thank my primary advisor **Matias** for training me, graciously sharing his experiences, and advising me in all aspects of work life. The things that have benefited me the most in the recent years and will be doing so throughout the rest of my career are not those that I have learned from classrooms but from numerous conversations and other forms of interactions with my mentor – with or without a beer. Many thanks to **Satu** and my committee members Drs. **Lauri Parkkonen**, **Petri Ala-Laurila** for overseeing my work and helpful advice. I thank Dr. **Juha Voipio** for kindly advising and supporting me in preparing my thesis submission and serving as my Custos. I thank Drs. **Krish Singh** and **Olaf Hauk** for reviewing this thesis and their kind compliments. I thank Dr. **Philippe Ciuciu** for examining my thesis and serving as my opponent**.** I thank **Gabriele** for not only top-notch collaboration, teaching me useful engineering skills but also for the fun of hanging out together. I thank **Felix** for working together throughout these years; as I have enjoyed countless nice conversations with him, I much appreciate his kind nature as well as his dedication to our BBQ socials. I thank current lab comrades **Santeri**, **Hamed**, **Vlad**, **Ehtasham**, **Joonas (J)**, **Joonas (K)**, **Marco**, and **Gabi** and former members **Muriel**, **Sami**, **Jaana**, **Anna**, **Nitin** and **Tuomas** (ordered by the time we first met) for good company and for sharing time and space in the lab. Special thanks to former lab members (*aka* the old Beer Club Gang). They are **Jonni**, **Alex**, **Pantelis, Shrikanth**, **Anton**, and **Isa** (ordered by the time we first met) for sharing beautiful memories – the first a few years of my life in Helsinki were truly the good old time that I cherish! Specifically, I thank **Jonni** for showing me the beauty of Finnish wildness, **Isa** and **Alex** for those lovely weekend coffee dates and including me in their most important life events; **Shrikanth** for numerous adventures as well as numerous witty conversations we have shared; **Pantelis** and **Krista** for including me to their lovely family time and offering those memorable superb culinary and cultural exposures; and **Anton** for leading beer-hunting adventures around the globe. I thank **Lea** for reading and commenting this thesis and **Joonas** for translating the abstract into Finnish. Many thanks to **Katri** for supporting me during my study and kindly spending extra time for helping me preparing my thesis submission. I thank the ***doctoral program Brain & Mind*** **(B&M)**, the ***Doctoral School in Health Sciences*** for nearly every year funding my conference travels. I thank Dr. **Kai Kaila** for many constructive conversations and very helpful advice. I thank Dr. **Michael Breakspear** for introducing me to the theories and tools that inspired my work. I thank Drs. **Doug Cheyne**, **Paul Ferrari,** and **Joe DeSouza** for supporting me to apply to this PhD position with Matias and Satu. Especially **Paul**, I probably could not have accomplished the MEG project for my MA thesis without him. Hence, I have regarded him as my mentor and a big brother even though his name is not formally on the record. I thank **Arja**, and **Vesa** for supporting me and embracing my Kitty and me as a part of the family. I especially thank **Taija** for her constant, unconditional care for me, without which I could not have made it this far.

I am extremely grateful and feeling lucky for having been surrounded by so many good and kind people all along in these years! Thank you all – I had a good time!

References

Abbott, L.F., DePasquale, B., Memmesheimer, R.M., 2016. Building functional networks of spiking model neurons. Nat. Neurosci.

Agu, M., Teramachi, Y., 1978. Prediction of catastrophes in bistable systems using externally applied random force. J. Appl. Phys. 49, 3645–3648.

Alonso, J., Chen, Y., 2009. Receptive field. Scholarpedia. https://doi.org/doi:10.4249/scholarpedia.5393

Alvarado-Rojas et al. 2013. Single-unit activities during epileptic discharges in the human hippocampal formation. Front. Comput. Neurosci.

Anderson, P.W., 1972. More Is Different. Science (80). 177, 393–396.

Aristotle, 1991. The Metaphysics. Prometheus books, New York.

Arnulfo, G., Hirvonen, J., Nobili, L., Palva, S., Palva, J.M., 2015. Phase and amplitude correlations in resting-state activity in human stereotactical EEG recordings. Neuroimage 114–127.

Aru, Juhan, et al., 2015. Untangling cross-frequency coupling in neuroscience. Curr. Opin. Neurobiol.

Arviv, O., Goldstein, A., Shriki, O., 2019. Neuronal avalanches and time-frequency representations in stimulus-evoked activity. Sci. Rep. 9.

Azevedo, F.A.C., et al., 2009. Equal numbers of neuronal and nonneuronal cells make the human brain an isometrically scaled-up primate brain. J. Comp. Neurol. 513, 532–541.

Baillet, S., 2017. Magnetoencephalography for brain electrophysiology and imaging. Nat. Neurosci.

Bak, P., 1996. How Nature Works: The Science of Self-Organized Criticality. Copernicus, New York.

Bak, P., Tang, C., Wiesenfeld, K., 1987. Self-Organized Criticality: An Explanation of 1/f Noise. Phys. Rev. Lett. 59, 381.

Bancaud, J., Talairach, J., 1965. La stéréo-électroencéphalographie dans l'épilepsie: informations neurophysiopathologiques apportées par l'investigation fonctionnelle stéréotaxique. Masson.

Bar-Yam, Y., 2002. General Features of Complex Systems, in: Encyclopedia of Life Support Systems. EOLSS UNESCO Publishers, Oxford, UK.

Bartolomei, F., Guye, M., Wendling, F., 2013. Abnormal binding and disruption in large scale networks involved in human partial seizures. EPJ Nonlinear Biomed. Phys.

Bassett, D.S., Bullmore, E., 2006. Small-world brain networks. Neuroscientist.

Bassingthwaighte, J.B., Liebovitch, L.S., West, B.J., 2012. Fractal physiology. Springer.

Bastos, A.M., Schoffelen, J.M., 2016. A tutorial review of functional connectivity analysis methods and their interpretational pitfalls. Front. Syst. Neurosci.

Bastos, A.M., Vezoli, J., Fries, P., 2015. Communication through coherence with inter-areal delays. Curr. Opin. Neurobiol. 31, 173–180.

Bechtel, W., 2007. Mental Mechanisms. Psychology Press.

Bedau, M.A., 1997. Weak Emergence. Philos. Perspect. 11.

Bednarz, M., Halliday, J.A., Herman, C., Golding, I., 2014. Revisiting bistability in the lysis/lysogeny circuit of bacteriophage lambda. PLoS One 9.

Beggs, J.M., 2008. The criticality hypothesis: How local cortical networks might optimize information processing. Philos. Trans. R. Soc. A Math. Phys. Eng. Sci. 366, 329–343.

Beggs, J.M., Plenz, D., 2004. Neuronal avalanches are diverse and precise activity patterns that are stable for many hours in cortical slice cultures. J. Neurosci. 24, 5216–5229.

Beggs, J.M., Plenz, D., 2003. Neuronal Avalanches in Neocortical Circuits. J. Neurosci. 23, 11167–11177.

Beggs, J.M., Timme, N., 2012. Being critical of criticality in the brain. Front. Physiol.

Benchenane, K. et al., 2010. Coherent Theta Oscillations and Reorganization of Spike Timing in the Hippocampal- Prefrontal Network upon Learning. Neuron 66, 921–936.

Beran, J., 1994. Statistics for Long-Memory Processes. New York: Routledge.

Bernstein, H., Byerly, H.C., Hopf, F.A., Michod, R.A., Vemulapalli, G.K., 1983. The Darwinian Dynamic. Q. Rev. Biol. 58.

Bertschinger, N., Natschläger, T., 2004. Real-Time Computation at the Edge of Chaos in Recurrent Neural Networks. Neural Comput. 16, 1413–1436.

Binney JJ, Dowrick, D., Fisher, A., Newman, M., 1993. The Theory of Critical Phenomena: An Introduction to the Renormalization Group (Oxford Science Publications). Oxford Univ Press, Oxford.

Boccaletti, S., Latora, V., Moreno, Y., Chavez, M., Hwang, D.U., 2006. Complex networks: Structure and

dynamics. Phys. Rep.
Boedecker, J., Obst, O., Lizier, J.T., Mayer, N.M., Asada, M., 2012. Information processing in echo state networks at the edge of chaos. Theory Biosci. 131, 205–213.
Boerlijst, M.C., Oudman, T., de Roos, A.M., 2013. Catastrophic Collapse Can Occur without Early Warning: Examples of Silent Catastrophes in Structured Ecological Models. PLoS One 8.
Bonachela, J.A., De Franciscis, S., Torres, J.J., Mũoz, M.A., 2010. Self-organization without conservation: Are neuronal avalanches generically critical? J. Stat. Mech. Theory Exp.
Bonachela, J.A., Muñoz, M.A., 2009. Self-organization without conservation: True or just apparent scale-invariance? J. Stat. Mech. Theory Exp.
Brading, K., Castellani, E., Teh, N., 2017. Symmetry and Symmetry Breaking. Stanford Encycl. Philos.
Bragin, A., Wilson, C.L., Staba, R.J., Reddick, M., Fried, I., Engel, J., 2002. Interictal high-frequency oscillations (80-500Hz) in the human epileptic brain: Entorhinal cortex. Ann. Neurol. 52, 407–415.
Brázdil, M., et al., 2017. Very high-frequency oscillations: Novel biomarkers of the epileptogenic zone. Ann. Neurol. 82, 299–310.
Breakspear, M., 2017. Dynamic models of large-scale brain activity. Nat. Neurosci.
Breakspear, M., Heitmann, S., Daffertshofer, A., 2010. Generative Models of Cortical Oscillations: Neurobiological Implications of the Kuramoto Model. Front. Hum. Neurosci.
Breakspear, M., et al., 2006. A unifying explanation of primary generalized seizures through nonlinear brain modeling and bifurcation analysis. Cereb. Cortex.
Breiman, L., 2001. Random Forests, in: Machine Learning. Kluwer Academic Publishers, pp. 5–32.
Brookes, M.J., et al., 2014. Measuring temporal, spectral and spatial changes in electrophysiological brain network connectivity. Neuroimage 91, 282–299.
Brookes, M.J., Woolrich, M.W., Barnes, G.R., 2012. Measuring functional connectivity in MEG: A multivariate approach insensitive to linear source leakage. Neuroimage 63, 910–920.
Bruns, A., Eckhorn, R., Jokeit, H., Ebner, A., 2000. Amplitude envelope correlation detects coupling among incoherent brain signals. Neuroreport 11, 1509–1514.
Bu, D., et al., 2003. Topological structure analysis of the protein-protein interaction network in budding yeast. Nucleic Acids Res. 31, 2443–2450.
Buendía, V., di Santo, S., Villegas, P., Burioni, R., Muñoz, M.A., 2019. Self-organized bistability: is it relevant for brain dynamics?
Buendía, V., di Santo, S., Bonachela, J.A., Muñoz, M.A., 2020. Feedback Mechanisms for Self-Organization to the Edge of a Phase Transition. Front. Phys.
Bullmore, E., Sporns, O., 2012. The economy of brain network organization. Nat. Rev. Neurosci. 13, 336–349.
Bullmore, E., Sporns, O., 2009. Complex brain networks: Graph theoretical analysis of structural and functional systems. Nat. Rev. Neurosci.
Buzsáki, G., 2018. Neural oscillation. Encycl. Br.
Buzsáki, G., 2012. Brain rhythms and neural syntax: implications for efficient coding of cognitive content and neuropsychiatric disease. Dialogues Clin Neurosci 14, 345–367.
Buzsáki, G., 2006. Rhythms of the Brain. Oxford University Press, New York.
Buzsáki, G., Anastassiou, C.A., Koch, C., 2012. The origin of extracellular fields and currents-EEG, ECoG, LFP and spikes. Nat. Rev. Neurosci. 407–420.
Buzsáki, G., Draguhn, A., 2004. Neuronal Oscillations in Cortical Networks. Science (80). 304, 1926.
Buzsáki, G., Silva, F.L. da, 2012. High frequency oscillations in the intact brain. Prog. Neurobiol. 241–9.
Cabral, J., Hugues, E., Sporns, O., Deco, G., 2011. Role of local network oscillations in resting-state functional connectivity. Neuroimage 57, 130–139.
Cabral, J., Kringelbach, M.L., Deco, G., 2014. Exploring the network dynamics underlying brain activity during rest. Prog. Neurobiol.
Canolty, R.T., et al., 2006. High gamma power is phase-locked to theta oscillations in human neocortex. Science (80). 313, 1626–1628.
Canolty, R.T., Knight, R.T., 2010. The functional role of cross-frequency coupling. Trends Cogn. Sci.
Cao, T., Wang, L., Sun, Z., Engel, S.A., He, S., 2018. The independent and shared mechanisms of intrinsic brain dynamics: Insights from bistable perception. Front. Psychol. 9.
Cardinale, F., et al., 2013a. Stereoelectroencephalography: Surgical methodology, safety, and stereotactic application accuracy in 500 procedures. Neurosurgery.
Cardinale, F. et al., 2013b. Stereoelectroencephalography: Surgical methodology, safety, and stereotactic

application accuracy in 500 procedures. Neurosurgery 72, 353–366.
Chialvo, D.R., 2010. Emergent complex neural dynamics. Nat. Phys. 6, 744–750.
Ciranna, L., et al., 2006. Serotonin as a modulator of glutamate- and GABA-mediated neurotransmission: implications in physiological functions and in pathology. Curr. Neuropharmacol 4, 101–114.
Clauset, A., Shalizi, C.R., Newman, M.E.J., 2009. Power-Law Distributions in Empirical Data. SIAM Rev.
Cocchi, L., Gollo, L.L., Zalesky, A., Breakspear, M., 2017. Criticality in the brain: A synthesis of neurobiology, models and cognition. Prog. Neurobiol.
Cohen, M.X., 2017. Where Does EEG Come from and What Does It Mean? Trends Neurosci.
Colclough, G.L., Brookes, M.J., Smith, S.M., Woolrich, M.W., 2015. A symmetric multivariate leakage correction for MEG connectomes. Neuroimage 117, 439–448.
Corning, P.A., 2002. The Re-emergence of "Emergence": A Venerable Concept in Search of a Theory One Solution: The "Synergism Hypothesis." Complexity 7, 18–30.
Cossu, M., et al., 2005. Stereoelectroencephalography in the presurgical evaluation of focal epilepsy: a retrospective analysis of 215 procedures. Neurosurgery 706–18, 706–18.
Costa, A. de A., Copelli, M., Kinouchi, O., 2015. Can dynamical synapses produce true self-organized criticality? J. Stat. Mech. Theory Exp.
Cowan, J.D., Neuman, J., van Drongelen, W., 2016. Wilson–Cowan Equations for Neocortical Dynamics. J. Math. Neurosci. 6, 1–24.
Cowan, J.D., Neuman, J., van Drongelen, W., 2014. Self-Organized Criticality and Near-Criticality in Neural Networks, in: Criticality in Neural Systems. Wiley-VCH, Weinheim, Germany, p. 465.
D'Andrea, A., et al., 2019. Alpha and alpha-beta phase synchronization mediate the recruitment of the visuospatial attention network through the Superior Longitudinal Fasciculus. Neuroimage 188, 722–732.
Darley, V., 1996. Emergent Phenomena and Complexity, in: Artificial Life V. MIT Press., Cambridge, MA.
de Arcangelis, L., 2012. Are dragon-king neuronal avalanches dungeons for self-organized brain activity? Eur. Phys. J. Spec. Top. 205, 243–257.
Deco, G., Jirsa, V.K., 2012. Ongoing cortical activity at rest: Criticality, multistability, and ghost attractors. J. Neurosci. 32, 3366–3375.
Deco, G., Jirsa, V.K., McIntosh, A.R., 2011. Emerging concepts for the dynamical organization of resting-state activity in the brain. Nat. Rev. Neurosci
Deco, G., Kringelbach, M.L., 2014. Great expectations: Using whole-brain computational connectomics for understanding neuropsychiatric disorders. Neuron.
Deco, G., Kringelbach, M.L., Jirsa, V.K., Ritter, P., 2017. The dynamics of resting fluctuations in the brain: Metastability and its dynamical cortical core. Sci. Rep. 7.
Deco, G., Rolls, E.T., Romo, R., 2009. Stochastic dynamics as a principle of brain function. Prog. Neurobiol.
Deco, G., Tononi, G., Boly, M., Kringelbach, M.L., 2015. Rethinking segregation and integration: Contributions of whole-brain modelling. Nat. Rev. Neurosci.
Destexhe, A., Contreras, D., Steriade, M., 1999. Spatiotemporal Analysis of Local Field Potentials and Unit Discharges in Cat Cerebral Cortex during Natural Wake and Sleep States.
Destrieux, C., Fischl, B., Dale, A., Halgren, E., 2010. Automatic parcellation of human cortical gyri and sulci using standard anatomical nomenclature. Neuroimage.
Di Santo, S., Burioni, R., Vezzani, A., Muñoz, M.A., 2016. Self-Organized Bistability Associated with First-Order Phase Transitions. Phys. Rev. Lett.
di Santo, S., Villegas, P., Burioni, R., Muñoz, M.A., 2018. Landau–Ginzburg theory of cortex dynamics: Scale-free avalanches emerge at the edge of synchronization. Proc. Natl. Acad. Sci. 115, E1356–E1365.
Díaz, F.A., 2017. Inequality, Social Protests and Civil War. OASIS 25–39.
Doesburg, S.M., Bedo, N., Ward, L.M., 2016. Top-down alpha oscillatory network interactions during visuospatial attention orienting. Neuroimage 132, 512–519.
Doesburg, S.M., Roggeveen, A.B., Kitajo, K., Ward, L.M., 2008. Large-scale gamma-band phase synchronization and selective attention. Cereb. Cortex 18, 386–396.
Drachman, D.A., 2005. Do we have brain to spare? Neurology.
Drakesmith, M., Caeyenberghs, K., Dutt, A., Lewis, G., David, A.S., Jones, D.K., 2015. Overcoming the effects of false positives and threshold bias in graph theoretical analyses of neuroimaging data. Neuroimage 118, 313–333.
Drakesmith, M., El-Deredy, W., Welbourne, S., 2013. Reconstructing coherent networks from electroencephalography and magnetoencephalography with reduced contamination from volume

conduction or magnetic field spread. PLoS One 8.
Dubnau, D., Losick, R., 2006. Bistability in bacteria. Mol. Microbiol. 61, 564–572.
Dusenbery, D.B., 1992. Sensory ecology : how organisms acquire and respond to information. New York : W.H. Freeman.
Edelman, G.M., 1993. Neural Darwinism: Selection and Reentrant Signaling in Higher Brain Function-Review, Neuron.
Eke, A., et al., 2000. Physiological time series: Distinguishing fractal noises from motions. Pflugers Arch. Eur. J. Physiol.
Eke, A., Herman, P., Kocsis, L., Kozak, L.R., 2002. Physiological Measurement Fractal characterization of complexity in temporal physiological signals Related content Relationship between DFA and spectral analysis. Physiol. Meas 23 R1.
Ellis, G.F., 2005. Physics, complexity and causality. Nature 435.
Ellis, G.F.R., 2008. On the nature of causation in complex systems. Trans. R. Soc. South Africa 63, 69–84.
Engel, A.K., Fries, P., Singer, W., 2001. Dynamic predictions: Oscillations and synchrony in top-down processing. Nat. Rev. Neurosci. 2, pages704–716.
Engel, J., da Silva, F.L., 2012. High-frequency oscillations - Where we are and where we need to go. Prog. Neurobiol. 316–8.
Englot, DJ, et al., 2010. Impaired consciousness in temporal lobe seizures: Role of cortical slow activity. Brain 133, 3764–3777.
Eronen, M.I., 2013. No levels, no problems: Downward causation in neuroscience. Philos. Sci. 80, 1042–1052.
Farahibozorg, S.R., Henson, R.N., Hauk, O., 2018. Adaptive cortical parcellations for source reconstructed EEG/MEG connectomes. Neuroimage 169, 23–45.
Felleman, D.J., Van Essen, D.C., 1991. Distributed Hierarchical Processing in the Primate Cerebral Cortex. Cereb. Cortex, 1, 1–47.
Fischl, B., Dale, A.M., 2000. Measuring the thickness of the human cerebral cortex from magnetic resonance images. PNAS 97, 11050–11055.
Fischl, B., et al., 2002. Neurotechnique Whole Brain Segmentation: Automated Labeling of Neuroanatomical Structures in the Human Brain. Neuron 33, 341–355.
Fornito, A., Zalesky, A., Breakspear, M., 2015. The connectomics of brain disorders. Nat. Rev. Neurosci.
Frauscher, B., et al., 2017. High-frequency oscillations: The state of clinical research. Epilepsia.
Freyer, F., Aquino, K., Robinson, P.A., Ritter, P., Breakspear, M., 2009. Bistability and Non-Gaussian Fluctuations in Spontaneous Cortical Activity. J. Neurosci.
Freyer, F., Roberts, J.A., Becker, R., Robinson, P.A., Ritter, P., Breakspear, M., 2011. Biophysical Mechanisms of Multistability in Resting-State Cortical Rhythms. J. Neurosci.
Freyer, F., Roberts, J.A., Ritter, P., Breakspear, M., 2012. A Canonical Model of Multistability and Scale-Invariance in Biological Systems. PLoS Comput. Biol.
Fries, P., 2015. Rhythms for Cognition: Communication through Coherence. Neuron.
Friston, K., 2013. Life as we know it. J. R. Soc. Interface 10.
Friston, K., 2010. The free-energy principle: A unified brain theory? Nat. Rev. Neurosci.
Friston, K., 2009. The free-energy principle: a rough guide to the brain? Trends Cogn. Sci. 13, 293–301.
Friston, K.J., 1994. Functional and Effective Connectivity in Neuroimaging: A Synthesis. Hum. Brain Mapp. 2, 56–78.
Gautam, S.H., Hoang, T.T., McClanahan, K., Grady, S.K., Shew, W.L., 2015. Maximizing Sensory Dynamic Range by Tuning the Cortical State to Criticality. PLoS Comput. Biol. 11.
Gell-Mann, M., 1995. The Quark and the Jaguar: Adventures in the Simple and the Complex. St. Martins Press-3PL.
Gilden, D.L., Wilson, S.G., 1995. On the nature of streaks in signal detection. Cogn. Psychol.
Godfrey-Smith, P., 2013. Philosophy of Biology. Princeton University Press.
Goldstein, J., 1999. Emergence as a Construct: History and Issues. Emergence 1, 49–72.
Gollo, L.L., Mirasso, C., Sporns, O., Breakspear, M., 2014. Mechanisms of Zero-Lag Synchronization in Cortical Motifs. PLoS Comput. Biol. 10.
Gollo, L.L., et al., 2018. Fragility and volatility of structural hubs in the human connectome. Nat. Neurosci.
Gross, J., et al., 2013. Good practice for conducting and reporting MEG research. Neuroimage.
Gu, H., Zhao, Z., Jia, B., Chen, S., 2015. Dynamics of on-off neural firing patterns and stochastic effects near a sub-critical Hopf bifurcation. PLoS One 10.

Hafting, T., Fyhn, M., Molden, S., Moser, M.-B., Moser, E.I., 2005. Microstructure of a spatial map in the entorhinal cortex. Nature 436, 801–806.
Hagmann, P., et al., 2008. Mapping the structural core of human cerebral cortex. PLoS Biol. 6, 1479–1493.
Haken, H., Kelso, J.A.S., Bunz, H., 1985. A theoretical model of phase transitions in human hand movements. Biol. Cybern.
Haldeman, C., Beggs, J.M., 2005. Critical branching captures activity in living neural networks and maximizes the number of metastable states. Phys. Rev. Lett. 94.
Halgren, M., Fabó, D., Ulbert, I., Madsen, J.R., Eross, L., Doyle, W.K., Devinsky, O., Schomer, D., Cash, S.S., Halgren, E., 2018a. Superficial Slow Rhythms Integrate Cortical Processing in Humans. Sci. Rep. 8.
Halgren, M., et al., 2018b. Superficial Slow Rhythms Integrate Cortical Processing in Humans. Sci. Rep. 2055.
Hämäläinen, M., Hari, R., Ilmoniemi, R.J., Knuutila, J., Lounasmaa, O. V., 1993. Magnetoencephalography—theory, instrumentation, and applications to noninvasive studies of the working human brain. Rev. Mod. Phys. 65, 413–497.
Hamalainen, M.S., Sarvas, J., 1989. Realistic Conductivity Geometry Model of the Human Head for Interpretation of Neuromagnetic Data, IEEE Transactions on Biomedical Engineering.
Hämäläinen, M.S.R., Ilmoniemi, R.J., 1994. Interpreting magnetic fields of the brain: minimum norm estimates. Med. Biol. Eng. Comput. 32, 35–42.
Hansen, P., Kringelbach, M., Salmelin, R., 2010. MEG: An Introduction to Methods. Oxford, New York.
Hardstone, R., Poil, S.S., Schiavone, G., Jansen, R., Nikulin, V. V., Mansvelder, H.D., Linkenkaer-Hansen, K., 2012. Detrended fluctuation analysis: A scale-free view on neuronal oscillations. Front. Physiol.
Hari, R., Parkkonen, L., Nangini, C., 2010. The brain in time: Insights from neuromagnetic recordings. Ann. N. Y. Acad. Sci.
Hari, R., Salmelin, R., 2012. Magnetoencephalography: From SQUIDs to neuroscience. Neuroimage 20th Anniversary Special Edition. Neuroimage.
Hauk, O., Stenroos, M., 2014. A framework for the design of flexible cross-talk functions for spatial filtering of EEG/MEG data: DeFleCT. Hum. Brain Mapp. 35, 1642–1653.
Hauk, O., Wakeman, D.G., Henson, R., 2011. Comparison of noise-normalized minimum norm estimates for MEG analysis using multiple resolution metrics. Neuroimage 54, 1966–1974.
Hawkins, J., Ahmad, S., Cui, Y., 2017. A theory of how columns in the neocortex enable learning the structure of the world. Front. Neural Circuits 11.
Hebb, D., 1950. The organization of behavior. John Wiley and Sons, Inc., New York.
Heitmann, S., Rule, M., Truccolo, W., Ermentrout, B., 2017. Optogenetic Stimulation Shifts the Excitability of Cerebral Cortex from Type I to Type II: Oscillation Onset and Wave Propagation. PLoS Comput. Biol. 13.
Hellyer, P.J., Jachs, B., Clopath, C., Leech, R., 2016. Local inhibitory plasticity tunes macroscopic brain dynamics and allows the emergence of functional brain networks. Neuroimage 124, 85–95.
Herculano-Houzel, S., 2011. Scaling of brain metabolism with a fixed energy budget per neuron: Implications for neuronal activity, plasticity and evolution. PLoS One 6.
Herculano-Houzel, S., Mota, B., Wong, P., Kaas, J.H., 2010. Connectivity-driven white matter scaling and folding in primate cerebral cortex. Proc. Natl. Acad. Sci. U. S. A. 107, 19008–19013.
Hidalgo, J., Seoane, L.F., Cortés, J.M., Muñoz, M.A., 2012. Stochastic amplification of fluctuations in cortical up-states. PLoS One 7.
Hill, S., 2014. Cortical Columns, Models of, in: Encyclopedia of Computational Neuroscience. Springer New York, pp. 1–4.
Hipp, J.F., Engel, A.K., Siegel, M., 2011. Oscillatory synchronization in large-scale cortical networks predicts perception. Neuron 69, 387–396.
Hipp, J.F., Hawellek, D.J., Corbetta, M., Siegel, M., Engel, A.K., 2012. Large-scale cortical correlation structure of spontaneous oscillatory activity. Nat. Neurosci. 15, 884–890.
Hirvonen, J., Monto, S., Wang, S.H., Palva, J.M., Palva, S., 2017. Dynamic large-scale network synchronization from perception to action. Netw. Neurosci. 2, 442–463.
Hodgkin, A.L., 1948. The local electric changes associated with repetitive action in a non-medullated axon. J. Physiol. 107, 165–181.
Hodgkin, A.L., Huxley, A.F., 1952. A quantitative description of membrane current and its application to conduction and excitation in nerve. J. Physiol 117, 500–544.
Hoel, E.P., Albantakis, L., Tononi, G., 2013. Quantifying causal emergence shows that macro can beat micro. Proc. Natl. Acad. Sci. U. S. A. 110, 19790–19795.

Holcman, D., Tsodyks, M., 2005. The emergence of Up and Down states in cortical networks. PLoS Comput. Biol. preprint, e23.
Horton, J.G., Adams, D.L., 2005. The cortical column: A structure without a function. Philos. Trans. R. Soc. B Biol. Sci.
Hubel, D.H., Wiesel, T.N., 1959. Receptive fields of single neurons in the cat's striate cortex. J. Physiol 148, 574–591.
Hülsemann, M.J., Naumann, E., Rasch, B., 2019. Quantification of phase-amplitude coupling in neuronal oscillations:comparison of phase-locking value, mean vector length, modulation index, and generalized-linear-modeling-cross-frequency-coupling. Front. Neurosci. 13.
Hurst, H.E., 1951. Long-term storage capacity of reservoirs. Trans. Am. Soc. Civ. Eng. 116, 770–799.
Huys, R., Perdikis, D., Jirsa, V.K., 2014. Functional architectures and structured flows on manifolds: A dynamical framework for motor behavior. Psychol. Rev. 121, 302–336.
Hyafil, A., Giraud, A.L., Fontolan, L., Gutkin, B., 2015a. Neural Cross-Frequency Coupling: Connecting Architectures, Mechanisms, and Functions. Trends Neurosci.
Hyafil, A., Giraud, A.L., Fontolan, L., Gutkin, B., 2015b. Neural Cross-Frequency Coupling: Connecting Architectures, Mechanisms, and Functions. Trends Neurosci.
Ihlen, E.A.F., Vereijken, B., 2010. Interaction-dominant dynamics in human cognition: Beyond 1/f fluctuation. J. Exp. Psychol. Gen.
Izhikevich, E.M., 2007. Dynamical systems in neuroscience: the geometry of excitability and bursting. MIT Press.
Jacobs, J., Levan, P., Chtillon, C.D., Olivier, A., Dubeau, F., Gotman, J., 2009. High frequency oscillations in intracranial EEGs mark epileptogenicity rather than lesion type. Brain 132, 1022–1037.
Jacobs, J., et al., 2018. Removing high-frequency oscillations. Neurology 11.
Jacobs, J., et al., 2010. High-frequency electroencephalographic oscillations correlate with outcome of epilepsy surgery. Ann. Neurol. 67, 209–220.
Jefferys, J.G.R., et al., 2012. Mechanisms of physiological and epileptic HFO generation. Prog. Neurobiol. 98, 250–64.
Jensen, M.H., Bak, P., Bohr, T., 1983. Complete Devil's Staircase, Fractal Dimension, and Universality of Mode-Locking Structure in the Circle Map. Phys. Rev. Lett. 50, 1637.
Jensen, O., et al., 2010. Exploring the electrophysiological correlates of the default-mode network with intracerebral EEG. Front. Syst. Neurosci. 4.
Jercog, D., et al., 2017. UP-DOWN cortical dynamics reflect state transitions in a bistable network. Elife 6.
Jirsa, V., Müller, V., 2013. Cross-frequency coupling in real and virtual brain networks. Front. Comput. Neurosci.
Jirsa, V.K., et al., 2017. The Virtual Epileptic Patient: Individualized whole-brain models of epilepsy spread. Neuroimage.
Jirsa, V.K., Stacey, W.C., Quilichini, P.P., Ivanov, A.I., Bernard, C., 2014. On the nature of seizure dynamics. Brain.
Jonas, E., Kording, K.P., 2017. Could a Neuroscientist Understand a Microprocessor? PLoS Comput. Biol. 13.
Jones, M.S., Macdonald, K.D., Choi, B., Dudek, F.E., Barth, D.S., 2000. Intracellular Correlates of Fast (200 Hz) Electrical Oscillations in Rat Somatosensory Cortex.
Juhász, R., Odor, G., Castellano, C., Muñoz, M.A., 2012. Rare-region effects in the contact process on networks. Phys. Rev. E 85.
Jung, C., 1981. The Archetypes and The Collective Unconscious. Walter-Verlag.
Kandel, E.R., Schwartz, J.H., Jessell, T.M., Siegelbaum, S.A., Hudspeth, A.J., 2012. Principles of Neural Science, 5th ed. McGraw-Hill.
Kantelhardt, J.W., 2008. Fractal and Multifractal Time Series.
Katzner, S., et al., 2009. Local Origin of Field Potentials in Visual Cortex. Neuron 61, 35–41. h
Kauffman, S.A., 1993. The Origins of Order: Self-Organization and Selection in Evolution. Oxford University Press, New York.
Kelso, J.A.S., 2012. Multistability and metastability: understanding dynamic coordination in the brain. Philos. Trans. R. Soc. B Biol. Sci. 367, 906–918.
Khamechian, M.B., Kozyrev, V., Treue, S., Esghaei, M., Daliri, M.R., 2019. Routing information flow by separate neural synchrony frequencies allows for "functionally labeled lines" in higher primate cortex 116, 12506–12515.

Khodagholy, D., Gelinas, J.N., Buzsáki, G., 2017. Learning-enhanced coupling between ripple oscillations in association cortices and hippocampus. Science (80). 369–372.
Kim, K., Kim, J.S., Chung, C.K., 2017. Increased gamma connectivity in the human prefrontal cortex during the bereitschaftspotential. Front. Hum. Neurosci. 11.
Kim, S., Park, S.H., Ryu, C.S., 1997. Noise-enhanced multistability in coupled oscillator systems. Phys. Rev. Lett. 78, 1616–1619.
Kinouchi, O., Brochini, L., Costa, A.A., Campos, J.G.F., Copelli, M., 2019. Stochastic oscillations and dragon king avalanches in self-organized quasi-critical systems. Sci. Rep. 9.
Kinouchi, O., Copelli, M., 2006. Optimal dynamical range of excitable networks at criticality. Nat. Phys. 2, 348–352.
Köhling, R., Staley, K., 2011. Network mechanisms for fast ripple activity in epileptic tissue. Epilepsy Res. 97, 318–323.
Korhonen, O., Palva, S., Palva, J.M., 2014. Sparse weightings for collapsing inverse solutions to cortical parcellations optimize M/EEG source reconstruction accuracy. J. Neurosci. Methods 226, 147–160.
Koulakov, A.A., Raghavachari, S., Kepecs, A., Lisman, J.E., 2002. Model for a robust neural integrator. Nat. Neurosci. 5, 775–782.
Krakauer, J.W., Ghazanfar, A.A., Gomez-Marin, A., MacIver, M.A., Poeppel, D., 2017. Neuroscience Needs Behavior: Correcting a Reductionist Bias. Neuron.
Kreuz, T., 2011. Measures of neuronal signal synchrony. Scholarpedia 6, 11922.
Kuruvilla, A., Flink, R., 2003. Intraoperative electrocorticography in epilepsy surgery: useful or not? Seizure 12, 577–584.
Kuwahara, H., Soyer, O.S., 2012. Bistability in feedback circuits as a byproduct of evolution of evolvability. Mol. Syst. Biol. 8.
Kuzawa, C.W., et al., 2014. Metabolic costs and evolutionary implications of human brain development. Proc. Natl. Acad. Sci. U. S. A. 111, 13010–13015.
La Rocca, D., Zilber, N., Abry, P., van Wassenhove, V., Ciuciu, P., 2018. Self-similarity and multifractality in human brain activity: A wavelet-based analysis of scale-free brain dynamics. J. Neurosci. Methods 309, 175–187.
Lachaux, J.-P., Rodriguez, E., Martinerie, J., Varela, F.J., 1999. Measuring Phase Synchrony in Brain Signals, Hum Brain Mapping.
Lachaux, J.P., Axmacher, N., Mormann, F., Halgren, E., Crone, N.E., 2012. High-frequency neural activity and human cognition: Past, present and possible future of intracranial EEG research. Prog. Neurobiol. 279–301.
Landauer, R., 1996. The physical nature of information, Physics Letters A.
Latham, P.E., Nirenberg, S., 2004. Computing and Stability in Cortical Networks. Neural Comput. 16, 1385–1412.
Laughlin, R.B., 2005. A different universe: reinventing physics from the bottom down. Basic Books, New York.
Lazebnik, Y., 2002. Can a biologist fix a radio?—Or, what I learned while studying apoptosis. Cancerl Cell 2, 179–182.
Lebar, T, et al., 2014. A bistable genetic switch based on designable DNA-binding domains. Nat. Commun. 5.
Lee, J.H., Whittington, M.A., Kopell, N.J., 2013. Top-Down Beta Rhythms Support Selective Attention via Interlaminar Interaction: A Model. PLoS Comput. Biol. 9.
Lee, S., et al., 2019. DC shifts, high frequency oscillations, ripples and fast ripples in relation to the seizure onset zone. Seizure.
Levina, A., Herrmann, J.M., Geisel, T., 2007. Dynamical synapses causing self-organized criticality in neural networks. Nat. Phys. 3, 857–860.
Levitis, D.A., Lidicker, W.Z., Freund, G., 2009. Behavioural biologists do not agree on what constitutes behaviour. Anim. Behav. 78, 103–110.
Lin, F.H., et al., 2006. Assessing and improving the spatial accuracy in MEG source localization by depth-weighted minimum-norm estimates. Neuroimage 31, 160–171.
Linkenkaer-Hansen, K., et al., 2007. Genetic contributions to long-range temporal correlations in ongoing oscillations. J. Neurosci. 27, 13882–13889.
Linkenkaer-Hansen, et al., 2005. Breakdown of long-range temporal correlations in theta oscillations in patients with major depressive disorder. J. Neurosci. 25, 10131–10137.
Linkenkaer-Hansen, K., Nikouline, V. V, Matias Palva, J., Ilmoniemi, R.J., 2001. Long-Range Temporal

Correlations and Scaling Behavior in Human Brain Oscillations. J. Neurosci.
Lisman, J.E., Idiart, M.A.P., 1995. Storage of 7 ± 2 short-term memories in oscillatory subcycles. Science (80). 267, 1512–1515.
Lisman, J.E., Jensen, O., 2013. The Theta-Gamma Neural Code. Neuron.
Liu, A.K., Dale, A.M., Belliveau, J.W., 2002. Monte Carlo simulation studies of EEG and MEG localization accuracy. Hum. Brain Mapp. 16, 47–62.
Lobier, M., Palva, J.M., Palva, S., 2018. High-alpha band synchronization across frontal, parietal and visual cortex mediates behavioral and neuronal effects of visuospatial attention. Neuroimage 165, 222–237.
Logothetis, N.K., et al., 2012. Hippocampal-cortical interaction during periods of subcortical silence. Nature 547–553.
Luders, H.., Engel, J.J., Munari, C., 1993. General principles, in: Surgical Treatment of the Epilepsies. 2nd Ed. Raven Press, New York, pp. 137–153.
Lundstrom, B.N., Boly, M., Duckrow, R., Zaveri, H.P., Blumenfeld, H., 2019. Slowing less than 1 Hz is decreased near the seizure onset zone. Sci. Rep. 9.
Maass, W., Natschläger, T., Markram, H., 2002. Real-Time Computing Without Stable States: A New Framework for Neural Computation Based on Perturbations, Neural Computation.
Majhi, S., Bera, B.K., Ghosh, D., Perc, M., 2018. Chimera states in neuronal networks: A review. Phys. Life Rev.
Mandelbrot, B., 1985. Self-affinity and fractal dimension, in: Physica Scripta. pp. 257–260.
Mandelbrot, B., 1983. The fractal geometry of nature. Macmillan.
Marchiori, M., Possamai, L., 2015. Micro-macro analysis of complex networks. PLoS One 10.
Markram, H., et al. (2015) Reconstruction and Simulation of Neocortical Microcircuitry. Cell 163, 456–492.
Markram, H., Tsodyks, M., 1996. Redistribution of synaptic efficacy between pyramidal neurons. Nature 807–10.
Meila, M., 2007. Comparing clusterings-an information based distance. J. Multivar. Anal. 98, 873–895.
Mejias, J.F., Kappen, H.J., Torres, J.J., 2010. Irregular dynamics in up and down cortical states. PLoS One 5.
Miller, P., Wang, X.J., 2006. Stability of discrete memory states to stochastic fluctuations in neuronal systems. Chaos 16.
Miller, S.M., Liu, G.B., Ngo, T.T., Hooper, G., Riek, S., Carson, R.G., Pettigrew, J.D., 2000. Interhemispheric switching mediates perceptual rivalry.
Millman, D., Mihalas, S., Kirkwood, A., Niebur, E., 2010. Self-organized criticality occurs in non-conservative neuronal networks during “up” states. Nat. Phys. 6, 801–805.
Mitrophanov, A.Y., Groisman, E.A., 2008. Positive feedback in cellular control systems.
Molnár, Z., 2013. Cortical Columns, in: Neural Circuit Development and Function in the Heathy and Diseased Brain. Elsevier Inc., pp. 109–129.
Montez, T., et al., 2009. Altered temporal correlations in parietal alpha and prefrontal theta oscillations in early-stage Alzheimer disease.
Monto, S., Palva, S., Voipio, J., Palva, J.M., 2008. Very Slow EEG Fluctuations Predict the Dynamics of Stimulus Detection and Oscillation Amplitudes in Humans. J. Neurosci. 28, 8268–72.
Monto, S., Vanhatalo, S., Holmes, M.D., Palva, J.M., 2007. Epileptogenic neocortical networks are revealed by abnormal temporal dynamics in seizure-free subdural EEG. Cereb. Cortex 17, 1386–1393.
Mora, T., Bialek, W., 2011. Are Biological Systems Poised at Criticality? J. Stat. Phys.
Moretti, P., Muñoz, M.A., 2013. Griffiths phases and the stretching of criticality in brain networks. Nat. Commun.
Morgan, MM, et al., 2010. Multiunit Activity, in: Encyclopedia of Psychopharmacology. Springer Berlin Heidelberg, Berlin, Heidelberg, pp. 809–809.
Morris, C., Lecar, H., 1981. Voltage oscillations in the barnacle giant muscle fiber. Biophys J 35, 193–213.
Mota, B., et al., 2019. White matter volume and white/gray matter ratio in mammalian species as a consequence of the universal scaling of cortical folding. Proc. Natl. Acad. Sci. U. S. A. 116, 15253–15261.
Mullin, J.P., Smithason, S., Gonzalez-Martinez, J., 2016. Stereo-electro-encephalo-graphy (SEEG) with robotic assistance in the presurgical evaluation of medical refractory epilepsy: A technical note. J. Vis. Exp. 2016.
Munari, C., Bancaud, J., 1985. The Role of stereo-electroencephalography (SEEG) in the evoluation of partial epileptic seizures, in: Porter, R., Morselli, P. (Eds.), The Epilepsies. Butterworth & Co., London.
Muñoz, M.A., 2018. Colloquium: Criticality and dynamical scaling in living systems. Rev. Mod. Phys. 90.
Muñoz, M.A., Juhász, R., Castellano, C., Ódor, G., 2010. Griffiths phases on complex networks. Phys. Rev.

Lett.
Newman, M.E.J., 2003. The Structure and Function of Complex Networks, Society for Industrial and Applied Mathematics.
Nicolelis, M.A.L., Ghazanfar, A.A., Faggin, B.M., Votaw, S., Oliveira, L.M.O., 1997. Reconstructing the Engram: Neurotechnique Simultaneous, Multisite, Many Single Neuron Recordings, Neuron.
Nikulin, V. V., Brismar, T., 2005. Long-range temporal correlations in electroencephalographic oscillations: Relation to topography, frequency band, age and gender. Neuroscience 130, 549–558.
Nikulin, V. V., Brismar, T., 2004. Long-range temporal correlations in alpha and beta oscillations: Effect of arousal level and test-retest reliability. Clin. Neurophysiol. 115, 1896–1908.
Nitzan, N., et al., 2020. Propagation of hippocampal ripples to the neocortex by way of a subiculum-retrosplenial pathway. Nat. Commun. 11, 1947.
Noback, C., Strominger, N., Demarest, R., Ruggiero DA, 2005. The Human Nervous System: Structure and Function, 6th ed. Totowa, NJ: Humana Press.
Noble, D., 2012. A theory of biological relativity: No privileged level of causation. Interface Focus.
Nolte, G., Bai, O., Wheaton, L., Mari, Z., Vorbach, S., Hallett, M., 2004. Identifying true brain interaction from EEG data using the imaginary part of coherency. Clin. Neurophysiol.
Nonoda, Y., et al., 2016. Interictal high-frequency oscillations generated by seizure onset and eloquent areas may be differentially coupled with different slow waves. Clin. Neurophysiol. 127, 2489–2499.
Novikoff, A.B., 1945. The Concept of Integrative Levels and Biology. Science (80). 101, 209–215.
Novitskaya, Y., Sara, S.J., Logothetis, N.K., Eschenko, O., 2016. Ripple-triggered stimulation of the locus coeruleus during post-learning sleep disrupts ripple/spindle coupling and impairs memory consolidation. Learn. Mem. 238–248.
Nunez, P., Srinivasan, R., 2007. Electroencephalogram. Scholarpedia 2, 1348.
Nurse, P., 2008. Life, logic and information. Nature 454, 424–6.
O'Connor, T., 1994. Emergent Properties. Am. Philos. Q. 31, 91–104.
O'Neill, G.C., Barratt, E.L., Hunt, B.A.E., Tewarie, P.K., Brookes, M.J., 2015. Measuring electrophysiological connectivity by power envelope correlation: A technical review on MEG methods. Phys. Med. Biol.
Ódor, G., 2019. Robustness of Griffiths effects in homeostatic connectome models. Phys. Rev. E 99.
Ódor, Géza, Dickman, R., Ódor, Gergely, 2015. Griffiths phases and localization in hierarchical modular networks. Sci. Rep.
Oizumi, M., Albantakis, L., Tononi, G., 2014. From the Phenomenology to the Mechanisms of Consciousness: Integrated Information Theory 3.0. PLoS Comput. Biol. 10.
Oostenveld, R., Fries, P., Maris, E., Schoffelen, J.M., 2011. FieldTrip: Open source software for advanced analysis of MEG, EEG, and invasive electrophysiological data. Comput. Intell. Neurosci. 2011.
Oyarzun, D.A., Chaves, M., 2015. Design of a bistable switch to control cellular uptake. J. R. Soc. Interface 12.
Pakkenberg, B., et al., 2003. Aging and the human neocortex. Exp. Gerontol. 38, 95–99.
Palva, J., Palva, S., 2014. The Correlation of the Neuronal Long-Range Temporal Correlations, Avalanche Dynamics with the Behavioral Scaling Laws and Interindividual Variability, in: Criticality in Neural Systems. Weinheim: Wiley-VCH, pp. 105–126.
Palva, J.M., 2005. Phase Synchrony among Neuronal Oscillations in the Human Cortex. J. Neurosci.
Palva, J.M., Monto, S., Kulashekhar, S., Palva, S., 2010a. Neuronal synchrony reveals working memory networks and predicts individual memory capacity. Proc. Natl. Acad. Sci. U. S. A. 107, 7580–7585.
Palva, J.M., Monto, S., Kulashekhar, S., Palva, S., 2010b. Neuronal synchrony reveals working memory networks and predicts individual memory capacity. Proc. Natl. Acad. Sci. U. S. A. 107, 7580–7585.
Palva, J.M., Palva, S., 2012. Infra-slow fluctuations in electrophysiological recordings, blood-oxygenation-level-dependent signals, and psychophysical time series. Neuroimage.
Palva, J.M., et al., 2018. Ghost interactions in MEG/EEG source space: A note of caution on inter-areal coupling measures. Neuroimage.
Palva, J.M., et al., 2013. Neuronal long-range temporal correlations and avalanche dynamics are correlated with behavioral scaling laws. Proc. Natl. Acad. Sci.
Palva, S., Monto, S., Palva, J.M., 2010. Graph properties of synchronized cortical networks during visual working memory maintenance. Neuroimage 49, 3257–3268.
Palva, S., Palva, J., 2012. Discovering oscillatory interaction networks with M/EEG: Challenges and breakthroughs. Trends Cogn. Sci. 16, 219–30.
Palva, S., Palva, J.M., 2018. Roles of Brain Criticality and Multiscale Oscillations in Temporal Predictions for

Sensorimotor Processing. Trends Neurosci. 41, 729–743.
Paquola, C., et al., 2019. Microstructural and functional gradients are increasingly dissociated in transmodal cortices. PLoS Biol. 17.
Patestas, M.A., Gartner, L.P., 2006. A Textbook of Neuroanatomy. BLACKWELL, Malden.
Pennisi, E., 2003. Modernizing the Tree of Life. Science (80). 300, 1692–1697.
Pérez-Cervera, A., Ashwin, P., Huguet, G., M. Seara, T., Rankin, J., 2019. The uncoupling limit of identical Hopf bifurcations with an application to perceptual bistability. J. Math. Neurosci. 9.
Peyrache, A., et al., 2012. Spatiotemporal dynamics of neocortical excitation and inhibition during human sleep. Proc. Natl. Acad. Sci. U. S. A. 109, 1731–1736.
Pikovsky, A., Rosenblum, M., Kurths, J., 2003. Synchronization A Universal Concept in Nonlinear Sciences. Cambridge University Press, New York.
Pillai, A.S., Jirsa, V.K., 2017. Symmetry Breaking in Space-Time Hierarchies Shapes Brain Dynamics and Behavior. Neuron.
Plenz, D., Thiagarajan, T.C., 2007. The organizing principles of neuronal avalanches: cell assemblies in the cortex? Trends Neurosci.
Polkinghorne, J., 2002. Reductionism, in: Tanzella-Nitti, G., Colagé, I., Strumia, A. (Eds.), Interdisciplinary Encyclopedia of Religion and Science. Colagé and A. Strumia.
Porta, L.D., Copelli, M., 2019. Modeling neuronal avalanches and long-range temporal correlations at the emergence of collective oscillations: Continuously varying exponents mimic M/EEG results. PLoS Comput. Biol. 15.
Priesemann, V., 2014. Spike avalanches in vivo suggest a driven, slightly subcritical brain state. Front. Syst. Neurosci.
Proix, T., Bartolomei, F., Guye, M., Jirsa, V.K., 2017. Individual brain structure and modelling predict seizure propagation. Brain.
Puce, A., Hämäläinen, M.S., 2017. A review of issues related to data acquisition and analysis in EEG/MEG studies. Brain Sci.
Qi, X., Zhongke, S., 2015. Bifurcation analysis and stability design for aircraft longitudinal motion with high angle of attack. Chinese J. Aeronaut. 28, 250–259.
Rakic, P., 2008. Confusing cortical columns. PNAS 105, 12099.
Rankin, J., Meso, A.I., Masson, G.S., Faugeras, O., Kornprobst, P., 2014. Bifurcation study of a neural field competition model with an application to perceptual switching in motion integration. J. Comput. Neurosci. 36, 193–213.
Rattay, F., Bassereh, H., Stiennon, I., 2018. Compartment models for the electrical stimulation of retinal bipolar cells. PLoS One 13.
Ray, S., Crone, N.E., Niebur, E., Franaszczuk, P.J., Hsiao, S.S., 2008. Neural correlates of high-gamma oscillations (60-200 Hz) in macaque local field potentials and their potential implications in electrocorticography. J. Neurosci. 28, 11526–11536.
Roberts, J.A., Boonstra, T.W., Breakspear, M., 2015. The heavy tail of the human brain. Curr. Opin. Neurobiol.
Roberts, J.A., Friston, K.J., Breakspear, M., 2017a. Clinical Applications of Stochastic Dynamic Models of the Brain, Part I: A Primer. Biol. Psychiatry Cogn. Neurosci. Neuroimaging.
Roberts, J.A., Friston, K.J., Breakspear, M., 2017b. Clinical Applications of Stochastic Dynamic Models of the Brain, Part II: A Review. Biol. Psychiatry Cogn. Neurosci. Neuroimaging.
Robinson, P.A., Rennie, C.J., Rowe, D.L., 2002. Dynamics of large-scale brain activity in normal arousal states and epileptic seizures. Phys. Rev. E - Stat. Physics, Plasmas, Fluids, Relat. Interdiscip. Top. 65, 9.
Roehri, N., et al., 2018. High-frequency oscillations are not better biomarkers of epileptogenic tissues than spikes. Ann. Neurol. 83, 84–97.
Roh, E., Kim, M.S., 2016. Brain regulation of energy metabolism. Endocrinol. Metab.
Rubinov, M., Sporns, O., 2010. Complex network measures of brain connectivity: Uses and interpretations. Neuroimage 52, 1059–1069.
Samorodnitsky, G., 2006. Long memory and self-similar processes, Annales de la Faculté des Sciences de Toulouse.
Sanchez-Panchuelo, R.M., Francis, S., Bowtell, R., Schluppeck, D., 2010. Mapping human somatosensory cortex in individual subjects with 7T functional MRI. J. Neurophysiol. 103, 2544–2556.
Santarnecchi, E., Galli, G., Polizzotto, N.R., Rossi, A., Rossi, S., 2014. Efficiency of weak brain connections support general cognitive functioning. Hum. Brain Mapp. 35, 4566–4582.

Schaefer, A., Kong, R., Gordon, E.M., Laumann, T.O., Zuo, X.-N., Holmes, A.J., Eickhoff, S.B., Yeo, B.T.T., 2017. Local-Global Parcellation of the Human Cerebral Cortex from Intrinsic Functional Connectivity MRI. Cereb. Cortex 28, 3095–3114.
Scheffer-Teixeira, R., Belchior, H., Leao, R.N., Ribeiro, S., Tort, A.B.L., 2013. On High-Frequency Field Oscillations (>100 Hz) and the Spectral Leakage of Spiking Activity. J. Neurosci. 33, 1535–9.
Schirner, M., Mcintosh, A.R., Jirsa, V.K., Deco, G., Ritter, P., n.d. Bridging multiple scales in the human brain using computational modelling.
Schoffelen, J.M., Gross, J., 2009. Source connectivity analysis with MEG and EEG. Hum. Brain Mapp.
Schrodinger, E., 1944. What is Life? Cambridge University Press.
Senkowski, D., Schneider, T.R., Foxe, J.J., Engel, A.K., 2008. Crossmodal binding through neural coherence: implications for multisensory processing. Trends Neurosci.
Shriki, O., Yellin, D., 2016. Optimal Information Representation and Criticality in an Adaptive Sensory Recurrent Neuronal Network. PLoS Comput. Biol. 12.
Siebenhühner, Felix, Lobier, M., Wang, S.H., Palva, S., Palva, J.M., 2016. Measuring Large-Scale Synchronization with Human MEG and EEG: Challenges and Solutions, in: Multimodal Oscillation-Based Connectivity Theory. Springer International Publishing, Cham, pp. 1–18.
Siebenhühner, F., Wang, S.H., Arnulfo, G., Nobili, L., Palva, J.M., Palva, S., 2020. Resting-state cross-frequency coupling networks in human electrophysiological recordings. PLOS Biol.
Siebenhühner, F., Wang, S.H., Palva, J.M., Palva, S., 2016. Cross-frequency synchronization connects networks of fast and slow oscillations during visual working memory maintenance. Elife 5.
Siegel, M., Engel, A.K., Donner, T.H., 2011. Cortical network dynamics of perceptual decision-making in the human brain. Front. Hum. Neurosci. 1–12.
Siljak, D.D., 2011. Decentralized control of complex systems. Dover Publications, Mineola, New York.
Silvanto, J., 2015. Why is "blindsight" blind? A new perspective on primary visual cortex, recurrent activity and visual awareness. Conscious. Cogn. 32, 15–32.
Simola, J., Zhigalov, A., Morales-Muñoz, I., Palva, J.M., Palva, S., 2017. Critical dynamics of endogenous fluctuations predict cognitive flexibility in the Go/NoGo task. Sci. Rep. 7.
Simon, H.A., 1962. The Architecture of Complexity, Proceedings of the American Philosophical Society.
Singer, W., 1999. Neuronal synchrony: a versatile code for the definition of relations? Neuron 24, 49–65.
Smialowski, A., Bijak, M., 1987. Excitatory and inhibitory action of dopamine on hippocampal neurons in vitro. Neuroscience 23, 95–101.
Sornette, D., 1998. Multiplicative processes and power laws.
Sornette, D., Ouillon, G., 2012. Dragon-kings Mechanisms, statistical methods and empirical evidence. Eur. Phys. J. Spec. Top. 205, 1–26.
Soto, J.L.P., Lachaux, J.P., Baillet, S., Jerbi, K., 2016. A multivariate method for estimating cross-frequency neuronal interactions and correcting linear mixing in MEG data, using canonical correlations. J. Neurosci. Methods 271, 169–181.
Sperry, R.W., 1980. Mind-brain interaction: Mentalism, yes; dualism, no. Neuroscience 5, 195–206.
Sporns, O., 2018. Graph theory methods: applications in brain networks.
Sporns, O., Betzel, R.F., 2016. Modular brain networks. Annu. Rev. Psychol. 67, 613–640.
Sporns, O., Tononi, G., Kötter, R., 2005. The human connectome: A structural description of the human brain. PLoS Comput. Biol.
Stam, C.J., Nolte, G., Daffertshofer, A., 2007. Phase lag index: Assessment of functional connectivity from multi channel EEG and MEG with diminished bias from common sources. Hum. Brain Mapp. 28, 1178–1193.
Stanley, H., 1971. Introduction to Phase Transitions and Critical Phenomena. Oxford University Press, New York.
Stanley, H.E., 1999. Scaling, universality, and renormalization: Three pillars of modern critical phenomena. Rev. Mod. Phys.
Steriade, M., Nunez, A., Amzica, F., 1993. A novel slow (< 1 Hz) oscillation of neocortical neurons in vivo: Depolarizing and hyperpolarizing components, Journal of Neuroscience.
Steriade, M., Timofeev, I., Grenier, F., 2001. Natural Waking and Sleep States: A View From Inside Neocortical Neurons.
Sterling, P., 2012. Allostasis: A model of predictive regulation. Physiol. Behav.
Strogatz, S., 2004. Sync: How Order Emerges from Chaos in the Universe, Nature, and Daily Life, 1st ed.

Hachette Books, New York.
Strogatz, S.H., 2001. Exploring complex networks. Nature 410, 268–276.
Stumpf, M.P.H., Porter, M.A., 2012. Critical Truths About Power Laws. Science (80-).
Tamas Vicsek, 2002. Complexity: The bigger picture. Nature 418.
Tanaka, T., Kaneko, T., Aoyagi, T., 2009. Recurrent Infomax Generates Cell Assemblies, Neuronal Avalanches, and Simple Cell-Like Selectivity, Neural Computation.
Tass, P., et al., 1998. Detection of n:m Phase Locking from Noisy Data: Application to Magnetoencephalography. Phys. Rev. Lett. 81, 3291.
Taulu, S., Simola, J., 2006. Spatiotemporal signal space separation method for rejecting nearby interference in MEG measurements. Phys. Med. Biol. 51, 1759–1768.
Thom, R., 1972. Structural Stability and Morphogenesis, 1st Ed. ed. CRC Press, Boca Raton.
Tononi, G., Boly, M., Massimini, M., Koch, C., 2016. Integrated information theory: From consciousness to its physical substrate. Nat. Rev.
Tort, A.B.L., Komorowski, R., Eichenbaum, H., Kopell, N., 2010. Measuring Phase-Amplitude Coupling Between Neuronal Oscillations of Different Frequencies. J. Neurophysiol.
Touboul, J., Destexhe, A., 2017. Power-law statistics and universal scaling in the absence of criticality. Phys. Rev. E 95.
Tsodyks, M. V., Markram, H., 1997. The neural code between neocortical pyramidal neurons depends on neurotransmitter release probability. Proc. Natl. Acad. Sci. U. S. A. 94, 719–723.
Turkheimer, F.E., et al., 2019. Conflicting emergences. Weak vs. strong emergence for the modelling of brain function. Neurosci. Biobehav. Rev.
Uhlhaas, P.J., Pipa, G., Lima, B., Melloni, L., Neuenschwander, S., Nikolić, D., Singer, W., 2009. Neural synchrony in cortical networks: History, concept and current status. Front. Integr. Neurosci. 3.
Uhlhaas, P.J., Singer, W., 2006. Neural Synchrony in Brain Disorders: Relevance for Cognitive Dysfunctions and Pathophysiology. Neuron.
van Wijk, B.C.M., Stam, C.J., Daffertshofer, A., 2010. Comparing brain networks of different size and connectivity density using graph theory. PLoS One 5.
Vanhatalo, S., Palva, J.M., Holmes, M.D., Miller, J.W., Voipio, J., Kaila, K., 2004. Infraslow oscillations modulate excitability and interictal epileptic activity in the human cortex during sleep. Proc. Natl. Acad. Sci. 101, 5053–7.
Varela, F., Lachaux, J.P., Rodriguez, E., Martinerie, J., 2001. The brainweb: Phase synchronization and large-scale integration. Nat. Rev. Neurosci. 2, 229–239.
Vaz, A.P., Inati, S.K., Brunel, N., Zaghloul, K.A., 2019. Coupled ripple oscillations between the medial temporal lobe and neocortex retrieve human memory. Science (80). 363, 975–978.
Vidal, J.R., et al., 2012. Long-Distance Amplitude Correlations in the High Gamma Band Reveal Segregation and Integration within the Reading Network. J. Neurosci. 32, 6421–6434.
Villa Martín, P., Bonachela, J.A., Levin, S.A., Muñoz, M.A., 2015. Eluding catastrophic shifts. Proc. Natl. Acad. Sci. 112, E1828–E1836.
Vinck, M., Oostenveld, R., Van Wingerden, M., Battaglia, F., Pennartz, C.M.A., 2011. An improved index of phase-synchronization for electrophysiological data in the presence of volume-conduction, noise and sample-size bias. Neuroimage.
Virkar, Y., Clauset, A., 2014. Power-law distributions in binned empirical data. Ann. Appl. Stat. 8, 89–119.
von Bertalanffy, L., 1968. General System Theory: Foundations, Development, Applications. George Braziller, New York.
Wandell, B.A., 2016. Clarifying Human White Matter. Annu. Rev. Neurosci. 39, 103–128.
Wandell, B.A., Dumoulin, S.O., Brewer, A.A., 2007. Visual field maps in human cortex. Neuron.
Wang, S.H., Lobier, M., Siebenhühner, F., Puoliväli, T., Palva, S., Palva, J.M., 2018 a. Hyperedge bundling: Data, source code, and precautions to modeling-accuracy bias to synchrony estimates. Data Br. 18, 262–275.
Wang, Z., Liu, Z., 2020. A Brief Review of Chimera State in Empirical Brain Networks. Front. Physiol.
Watts, D., Strogatz, S., 1998. Collective dynamics of 'small-world' networks. Nature 393, 440.
Weaver, W., 1948. Science and Complexity. Am. Sci. 36, 536.
Wiener,N., 1948. Cybernetics: Or Control and Communication in the Animal and the Machine, 2nd revise ((Hermann & Cie) & Camb. Mass. (MIT Press).
Wilson, C., 2008. Up and down states. Scholarpedia 3, 1410.

Wilson, H.R., Cowan, J.D., 1972. Excitatory and Inhibitory Interactions in Localized Populations of Model Neurons. Biophys. J. 12, 1–24.
Wilting, J., Priesemann, V., 2019. Between Perfectly Critical and Fully Irregular: A Reverberating Model Captures and Predicts Cortical Spike Propagation. Cereb. Cortex 29, 2759–2770.
Wilting, J, Priesemann, V., 2019. 25 years of criticality in neuroscience — established results, open controversies, novel concepts. Curr. Opin. Neurobiol. 58, 105–111.
Wit, E., van den Heuvel, E., Romeijn, J.W., 2012. 'All models are wrong.': An introduction to model uncertainty. Stat. Neerl.
Womelsdorf, T., Fries, P., 2007. The role of neuronal synchronization in selective attention. Curr. Opin. Neurobiol.
Womelsdorf, T., Valiante, T.A., Sahin, N.T., Miller, K.J., Tiesinga, P., 2014. Dynamic circuit motifs underlying rhythmic gain control, gating and integration. Nat. Neurosci.
Yeo, B.T., et al., 2011. The organization of the human cerebral cortex estimated by intrinsic functional connectivity. J. Neurophysiol. 106, 1125–1165.
Zeeman, E.C., 1976. Catastrophe Theory. Sci. Am.
Zhang, K., Sejnowski, T.J., 2000. A universal scaling law between gray matter and white matter of cerebral cortex. PNAS 97, 5621–5626.
Zimmern, V., 2020. Why Brain Criticality Is Clinically Relevant: A Scoping Review. Front. Neural Circuits 14.